Measurements of the ^{13}C and ^{35}Cl radiative neutron capture reaction cross sections

A thesis submitted to the The University of Manchester for the degree of Doctor of Philosophy in the Faculty of Science and Engineering

2021

Samuel A. Bennett

Department of Physics and Astronomy in the School of Natural Sciences

Contents

The number of words in this document is 33,421

List of Figures

List of Tables

Abstract

ABSTRACT OF THESIS submitted to The University of Manchester by Samuel A. Bennett for the Degree of Doctor of Philosophy, entitled: *Measurements of the ^{13}C and ^{35}Cl radiative neutron capture reaction cross sections.*

Date of submission: 15/11/2021

In the first measurement reported in this thesis, the $^{35}\text{Cl}(n, \gamma)^{36}\text{Cl}$ reaction cross section in the resolved resonance region has been determined by measuring a NaCl sample (99.635% purity, 3.174×10^{-3} ^{35}Cl atoms/barn) at the 185 m beam-line at the n_TOF time-of-flight facility at CERN using the total energy detection method, with a set-up composed of C_6D_6 detectors. The systematic uncertainty associated with the measured reaction yield was 4.4% up to 10 keV and 5.6% for larger energies up to around 100 keV, and resonances were analysed with the R-matrix code SAMMY up to an energy of around 60 keV. The measured resonance kernels are systematically larger than those reported in the ENDF/B-VIII.0 and JEFF-3.3 libraries by around 15%, and are moreover in agreement with one of the previous two measurements suggesting that a new evaluation should adopt this larger normalisation in the resonance region. The resonant component of the 30 keV Maxwellian averaged cross section (MACS) is also around 15% larger than that according to ENDF/BVIII.0, and is in reasonable agreement with a recent dedicated AMS measurement to within the 1-σ level.

For the second measurement reported in this thesis, ampoules of amorphous 99.5% enriched ^{13}C were irradiated at the PF1b neutron beam line at the high-flux Institut Laue–Langevin (ILL) research reactor in order to produce ^{14}C atoms. The precise ratio of ^{14}C/^{13}C was subsequently measured at the Vienna Environmental Research Accelerator (VERA) via accelerator mass spectrometry (AMS), allowing the $^{13}\text{C}(n, \gamma)^{14}\text{C}$ thermal cross section to be accurately determined. This is the first measurement of this cross section at sub-eV energies via this technique and the result of 1.52±0.07 mb for the thermal cross section is in good agreement with other recent measurements which were performed via Prompt Gamma-ray Activation Analysis.

Declaration of Authorship

I, Samuel A. Bennett, confirm that no portion of the work referred to in the thesis has been submitted in support of an application for another degree or qualification of this or any other university or other institute of learning.

Chapter 4 of this thesis consists to a large extent of the article *'Measurement of the* $^{13}C(n,\gamma)$ *thermal cross section via neutron irradiation and AMS'* [1]. The majority of the work including the experimental work and data analysis was performed by S. Bennett. The experimental work associated with the 2016 phase of the experiment was carried out by co-authors.

Copyright statement

(i) The author of this thesis (including any appendices and/or schedules to this thesis) owns certain copyright or related rights in it (the "Copyright") and he has given The University of Manchester certain rights to use such Copyright, including for administrative purposes.

(ii) Copies of this thesis, either in full or in extracts and whether in hard or electronic copy, may be made **only** in accordance with the Copyright, Designs and Patents Act 1988 (as amended) and regulations issued under it or, where appropriate, in accordance with licensing agreements which the University has from time to time. This page must form part of any such copies made.

(iii) The ownership of certain Copyright, patents, designs, trade marks and other intellectual property (the "Intellectual Property") and any reproductions of copyright works in the thesis, for example graphs and tables ("Reproductions"), which may be described in this thesis, may not be owned by the author and may be owned by third parties. Such Intellectual Property and Reproductions cannot and must not be made available for use without the prior written permission of the owner(s) of the relevant Intellectual Property and/or Reproductions.

(iv) Further information on the conditions under which disclosure, publication and commercialisation of this thesis, the Copyright and any Intellectual Property University IP Policy (see http://documents.manchester.ac.uk/display.aspx?DocID=24420), in any relevant Thesis restriction declarations deposited in the University Library, The University Library's regulations (see http://www.library.manchester.ac.uk/about/regulations/) and in The University's policy on Presentation of Theses.

Acknowledgements

Chapter 1

Introduction

1.1 Nuclear data for technologies

Nuclear data pertains to the quantities that describe the physical properties and behaviour of nuclei, including their structure, decay and interaction probabilities with other nuclei. These properties are fundamental to many fields ranging from basic physics research, including fundamental nuclear research and astrophysics, to industrial applications in which they are essential for the efficient, safe and reliable execution of varied nuclear technologies from power generation to medical physics [2,3]. Owing to their importance there are large efforts to coordinate the evaluation and dissemination of such data, which in general may come from experiments or theoretical calculations. Despite decades of data gathering, there are many isotopes (not limited to unstable isotopes) for which data are scarce. Moreover, as detector technologies and methods have improved over time, new measurements with unprecedented accuracy can be performed that can complement older datasets. The results of individual experiments and the associated experimental methods are collated in the EXFOR database (Experimental Nuclear Reaction Data) [4], coordinated by the IAEA (International Atomic Energy Agency) [5]. Before dissemination for use by the end user for whichever technology, the data are evaluated: this procedure takes each experimental measurement (and calculations in some cases where experimental data are not available or are limited) for a specific quantity (the value(s), reported experimental circumstances and associated uncertainties) and aims to produce the best estimate of the quantity. This is especially important for quantities differential in some other parameter, for example a reaction cross section differential in energy where some measurements will only report the cross section in a narrow energy interval. In these cases, measurements and nuclear model calculations must be combined to yield the

most complete and consistent final result, suitable for the intended application. The major data evaluations include ENDF/B-III.0 (USA), JEFF-3.3 (Europe) and JENDL-4.0 (Japan), amongst others; these libraries contain incident neutron data, as well as many other types including incident charged particle and photo-nuclear data for example.

In the context of nuclear power specific to the UK, a recent NIRAB (Nuclear Innovation and Research Advisory Board) report acknowledges the key role that nuclear data has in the future development of nuclear technologies: "whilst adequate for current reactor systems, existing nuclear data is not adequate for the assessment of advanced fuels (in current reactors); advanced reactors (Gen-IV and beyond); and for understanding the wastes arising from these systems" [6]. The response to this acknowledgement are plans to ensure access to such data and focus on obtaining new measurements of more accurate data with more complete understanding of the associated uncertainties. A review of the need for data to support advanced energy systems can be found in Reference [7]. Furthermore, despite their successful operation for many decades, there can be nuclear data issues associated with the decommissioning of the current fleet of nuclear reactors worldwide [8]; the two measurements in this thesis, the neutron capture cross sections of ^{35}Cl and ^{13}C, are concerned with this issue. Moreover, nuclear data is the bedrock of novel medical technologies aiming to provide ever safer and more effective cancer radiotherapies such as boron neutron capture therapy, one of the applications of the ^{35}Cl measurement in this work [9]. Finally, basic physics such as understanding the origin of elements in stellar neutron capture processes rely on accurate neutron induced reaction data, a further application of the ^{35}Cl measurement in this work.

1.2   Neutron induced reaction cross sections

In this section, a brief summary of neutron induced nuclear reactions is given. In general the relative probability of a particular nuclear reaction (α, β) occurring is expressed as a cross section $\sigma_{\alpha, \beta}$, which has units of area and is defined such that the reaction rate $R_{\alpha, \beta}$ is given by

$$R_{\alpha, \beta} = N_t \sigma_{\alpha, \beta} \phi_\alpha \tag{1.1}$$

where N_t is the number of target nuclei and ϕ_α is the rate at which projectiles α, in this work neutrons, pass through the target per unit area. The cross section is more formally given by

$$\sigma \sim \pi \lambda^2 |H_{i,f}|^2, \tag{1.2}$$

where $H_{i,f}$ is the matrix element that transforms the initial state i to the final state f. For a neutron induced reaction, the wavelength λ is given by

$$\lambda = \sqrt{\frac{m_n + m_t}{m_t}} \frac{\hbar}{\sqrt{2m_n E_n}} \tag{1.3}$$

where m_n and m_t are the masses of the neutron and target, and E_n is the neutron kinetic energy in the laboratory.

In general, neutron-nucleus reactions separate into two groups, direct and compound reactions, but where the form for a particular reaction is not necessarily exclusive as the same reaction products can be obtained from a mixture of the direct and compound mechanisms.

For the case of direct reactions there is a single step in which the reaction occurs, typically populating single particle states within the residual nucleus formed in the reaction. Direct reactions occur over short timescales on the order of 10^{-22} s and are non-resonant; the reaction cross section varies smoothly with incoming neutron kinetic energy. For cases where the total reaction cross section for a particular channel (α, β) is very small, the direct component can be significant.

For the case of compound nuclear reactions, there is a two-step reaction mechanism where in the first step, the projectile and target nucleus form an excited compound nucleus (CN). In this intermediate 'compound' state, the nucleus equilibrates and excitation is shared amongst all nucleons. The total excitation energy is given by $E^{\star} = Q + E^{CM}$ where Q is the Q-value of the reaction and E^{CM} refers to the kinetic energy of the projectile in the centre-of-mass system. By the nature of this reaction mechanism, when $E^{\star}$ matches the energy of an eigenstate of the compound system, quasi-stationary resonant states are populated which decay via any energetically allowed channel, and the reaction cross section can vary by many orders of magnitude, shown for example in Figure 1.1. The intermediate states live long enough that the exact nature of the formation of the state is forgotten, and the decay to the final state depends only on the excitation energy $E^{\star}$ and the spin-parity J^{π} of the compound nucleus and is hence independent of the formation channel — the Bohr independence hypothesis.

There are three main characteristic regions of the neutron induced reaction cross section differential in incoming neutron kinetic energy, shown in Figure 1.1:

- In the absence of a Coulomb barrier, neutrons of very low kinetic energies can penetrate and interact with the atomic nucleus. Under the assumptions that the incoming neutron energy is low ($\lesssim 50$ MeV) and that the only channels are
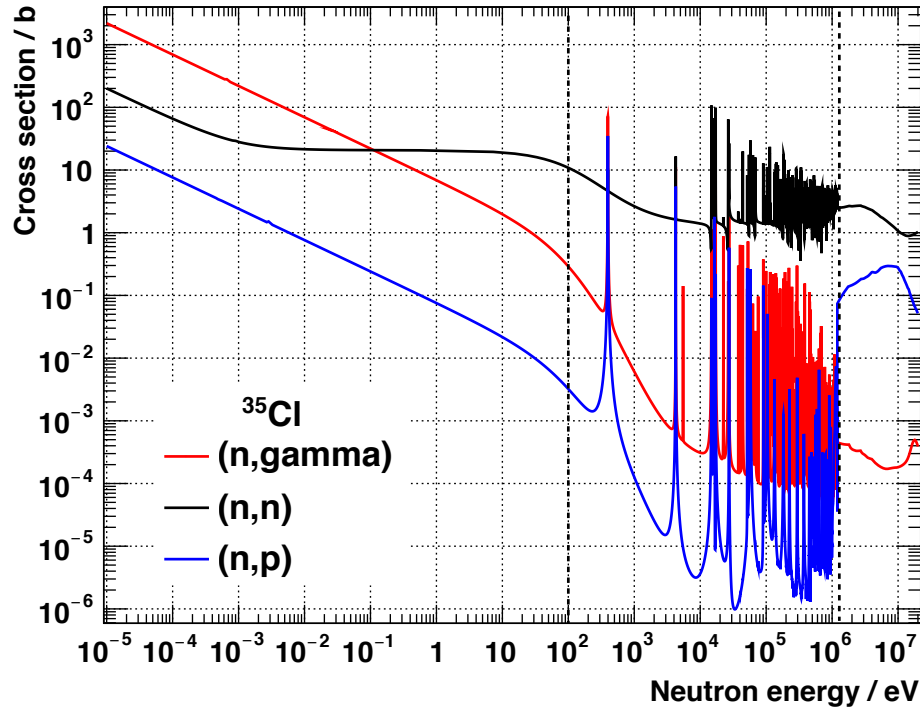
FIGURE 1.1: An example of the neutron induced cross section differential in neutron energy for the three dominant channels in this energy range in the case of $n+^{35}$Cl, a nucleus studied later on in this work. The data are from the ENDF B-VIII.0 library. Moving from low to high neutron energies, the three regions bounded by vertical dashed lines are called the *1/v* region, *Resolved Resonance Region* (RRR) and the *Unresolved Resonance Region* (URR), each described in the text.

either elastic scattering (non-resonant) or compound nucleus formation, it can be shown that the compound nucleus formation cross section for neutrons with orbital angular momentum $\ell = 0$ has the form

$$\sigma_{CN} = \frac{\pi}{k^2} \frac{4kK}{(k+K)^2},$$

(1.4)

where k and K are the wavenumbers of the neutron moving outside and inside the nuclear potential respectively. In the limit of low energies, $k \ll K$. Under these conditions $\sigma_{CN} = 4\pi/kK$; thus $\sigma_{CN} \propto 1/v$ where v is the incoming neutron speed. The cross section in the **1/v** region is the sum of the low energy tails of the many resonances centred at larger energies and is usually measured and reported for $E_n = 25.3$ meV, corresponding to thermalised neutrons with temperature $T = 290$ K. The cross section can then be extrapolated to different neutron energies in the $1/v$ region according to the $\sigma \sim 1/\sqrt{E_n}$ relation.

- The **Resolved Resonance Region (RRR)** is characterised by the resonant structures at intermediate neutron energies. In this region, the spacing between resonances is larger than their width. This region can extend to multiple MeV

for light nuclei, but extends to far lower energies for heavy nuclei where the level spacing is smaller.

- The RRR transitions to the **Unresolved Resonance Region (URR)** when the spacing between resonances become smaller than their widths, giving rise to a smoothly varying cross section — there is nevertheless still structure in the cross section that arises mainly from the interference between the component of the incident beam that passes through the target nucleus and the component that passes around it. This region is best described theoretically with an optical model or with Hauser-Feshbach theory which uses R-Matrix theory to calculate a cross section using the statistical properties of resonances.

As illustrated in Figure 1.1, even for the case of a relatively light nucleus the resonance structure of the RRR can become very complex, even more so for heavier nuclei with higher level densities — the nuclear wavefunctions become intractable and changes in energy of just a few eV can populate completely different eigenstates of the compound nucleus. In this regime therefore, calculations can only deliver average properties of the cross section and statistical properties of resonances. It is for this reason that although the energy dependence of reaction cross sections can be calculated to some degree, the precise energy dependence and position of resonances must be measured experimentally — especially when accurate reaction data are required for technological and/or astrophysical applications.

Resonances

Since for compound nuclear reactions there are two reaction steps, CN formation and subsequent decay, the cross section for a particular reaction with entrance and exit channels α and β can be factorised and written as

$$\sigma_{\alpha,\beta} = \sigma_{CN}(\alpha)P(\beta). \tag{1.5}$$

The quantity $\sigma_{CN}(\alpha)$ is the cross section for the formation of the CN through entrance channel α, and $P(\beta)$ is the probability of decaying from the CN via channel β. $P(\beta)$ is associated with the partial width for that channel, Γ_β such that $P(\beta) = \Gamma_\beta/\Gamma$, where $\Gamma = \sum_\beta \Gamma_\beta$. In the vicinity of an isolated resonance in the RRR, the cross section for the reaction (α, β) has a Breit-Wigner profile and is given by

$$\sigma(E_n) = \pi \lambda^2 g \frac{\Gamma_\alpha \Gamma_\beta}{(E_n - E_R)^2 - \Gamma^2/4}, \tag{1.6}$$

where E_R is the centroid of the resonance. The reaction cross section can therefore be described by the partial and total widths, and the energy of the resonance. The spin coupling factor g is given by

$$g = \frac{2J + 1}{(2I + 1)(2s + 1)} \tag{1.7}$$

where J is the total CN spin, I is the target nucleus spin and s is the incoming projectile spin, in this neutrons with $s = 1/2$.

The general formalism to describe the resonant behaviour in compound nuclear reactions is the R-Matrix theory, the details of which can be found in References [10, 11].

1.3   Radiative neutron capture

Radiative neutron capture (n, γ), the subject of the measurements in this thesis, proceeds through the formation of a compound nucleus prior to de-excitation to the ground state via a cascade composed of one or more gamma-rays (plus possible internally converted electrons) over a timescale of $\sim 10^{-14}$ s. For the case of a target nucleus $^{A}_{Z}X$:

$$^{A}_{Z}X + n \rightarrow^{A+1}_{Z} X^{\star} \rightarrow^{A+1}_{Z} X + \gamma\text{'s } (+e^{-}\text{'s}). \tag{1.8}$$
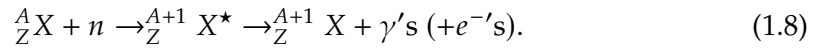
This process is shown schematically in Figure 1.2.

The excitation energy of the intermediate state $^{A+1}_{Z}X^{\star}$ is given by

$$E^{\star} = S_n + \frac{A}{A + 1}E_n, \tag{1.9}$$

where S_n is the neutron separation energy of the nucleus $^{A+1}_{Z}X$ and E_n is the kinetic energy of the incident neutron in the laboratory. Equivalently, for a cascade of γ-ray multiplicity M_{γ} and converted electron multiplicity M_e, with energies E^{γ}_i and E^{e}_i respectively,

$$E^{\star} = \sum_{i}^{M_{\gamma}} E^{\gamma}_i + \sum_{i}^{M_e} E^{e}_i. \tag{1.10}$$

In order to detect neutron capture reactions therefore, one may exploit measurements of the multiplicity or total energy of the cascade, or both in some cases; these two detection approaches are discussed in the next chapter. An alternative approach, also discussed in the next chapter, is not to detect the prompt reaction products, but instead to measure the product nuclei $^{A+1}_{Z}X$, which may be performed after a neutron irradiation.
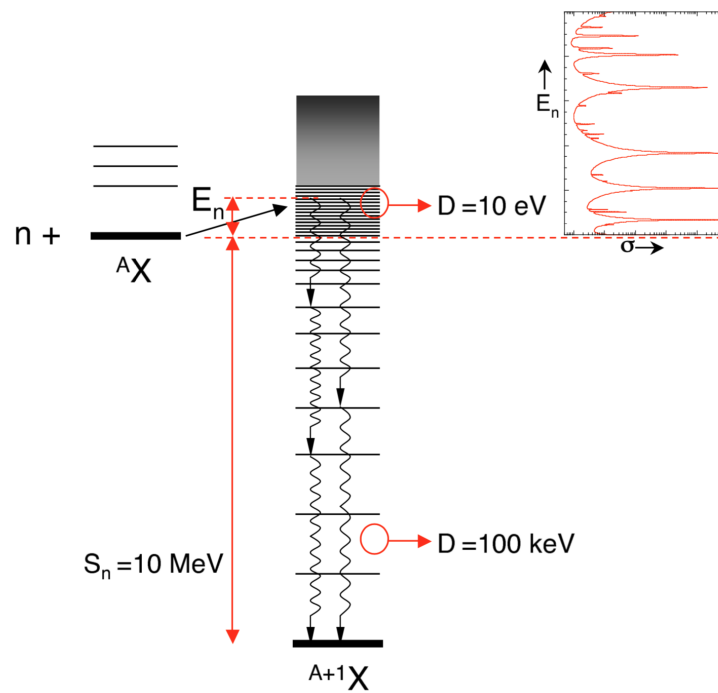
FIGURE 1.2: Schematic of the two-step process in radiative neutron capture. The resonant structures correspond to states of the intermediate compound system. Order of magnitude level spacings and neutron separation energy are shown. Figure taken from [12].

Chapter 2

Radiative neutron capture measurement techniques

This chapter contains an overview of the most common methods for measuring radiative neutron capture cross sections. Specific details relating to the methodologies used for the cross section measurements in this work are given in their respective chapters.

The cross section defined by Equation 1.1 is determined experimentally either by measuring the reaction rate through the detection of prompt reaction products, gamma-rays in the case of radiative capture, or by measuring the number of target nuclei that underwent neutron capture during a neutron irradiation via a suitable post-irradiation analysis of the irradiated sample. *Prompt* detection techniques include: using high resolution detectors to measure the gamma-rays from distinct (known) transitions within the electromagnetic de-excitation cascade following neutron capture; measuring the total energy of the cascade using the 'Total Energy Detection' (TED) technique using low resolution liquid scintillators; or by measuring all of the gamma-rays from the cascade via 'Total Absorption Calorimetry' (TAC). *Post-irradiation* techniques include measuring the radioactive decay of the activated products, or direct atom counting, both to deduce the total number of capture reactions that occurred during a neutron irradiation. Each of these approaches are discussed below.

All cross sections are ideally required over a wide range of neutron energies to suit any potential application, although for some applications the cross section may only be desired at a particular energy. In some cases the approach taken is to measure the cross section at discrete energies, after which the measurement is used to normalise a cross section calculated using some suitable theory, using either the Hauser-Feshbach formalism or optical model calculations. The most accurate measurements of reaction

cross sections over a wide energy range are performed using the time-of-flight technique. Examples of neutron sources used for such measurements are given below.

2.1 Neutron capture cross section measurement principles

In a reaction cross section experiment the quantity that is required to deduce the cross section either at a single neutron energy or over a range of neutron energies is the reaction yield $Y_{n,\gamma}(E_n)$. It is defined as the fraction of neutrons which pass through the sample that lead to the (n, γ) reaction:

$$Y_{n,\gamma}(E_n) = \frac{N_{n,\gamma}(E_n)}{\Phi(E_n)},$$ (2.1)

where $N_{n,\gamma}(E_n)$ is the number of capture reactions and where $\Phi(E_n)$ is the total number of neutrons which passed through the sample (the neutron fluence); it takes the values $0 \leq Y \leq 1$. For the case of a parallel neutron beam impinging perpendicular to the surface of a homogeneous sample of uniform thickness, the capture yield is related to the capture cross section $\sigma_{n,\gamma}$ via

$$Y_{n,\gamma}(E_n) = (1 - T) \frac{\sigma_{n,\gamma}(E_n)}{\sigma_{total}(E_n)} \underset{n\sigma_{total} \ll 1}{\approx} n\sigma_{n,\gamma}(E_n),$$ (2.2)

where n is the areal density, the number of target nuclei per unit area of the sample face perpendicular to the beam, and σ_{total} is the total neutron reaction cross section. In the first equality the factor $(1 - T)$ gives the fraction of neutrons that interact with the target, giving rise to the 'self-shielding effect', where the transmission factor $T = e^{-n\sigma_{total}(E_n)}$, and the factor $\sigma_{n,\gamma}/\sigma_{total}$ gives the fraction of these neutrons that lead to the reaction of interest.

In general there are experimental effects that mean Equation 2.2 only holds in the ideal case and which require experiment specific corrections. These include:

- multiple scattering where neutrons can be captured after scattering one or more times in the sample: $Y_{meas} = Y_1 + Y_2 + \ldots$ where Y_i is the yield where the neutron was captured upon its ith interaction with the sample (Equation 2.2 pertains to Y_1).

- self-attenuation where the reaction products are scattered and attenuated within the sample leading to an underestimation of the reaction yield. This effect is negligible for gamma-rays (from capture reactions), but the effect can be large for the internally converted electrons generated as part of a capture cascade.

The following sections give an overview of the most common experimental methods used to deduce the reaction yield defined above, and hence the reaction cross section. A comprehensive review of neutron capture cross section measurement techniques can be found in Reference [13].

2.2 Post-irradiation measurements

Post-irradiation techniques are based on counting the neutron capture reaction products, the nuclei $^{A+1}_{Z}X$ produced during an irradiation, with respect to the number of target nuclei $^{A}_{Z}X$. This can be done in two ways: if the product is radioactive and short lived, the nuclei $^{A+1}_{Z}X$ can be quantified by decay counting, or if the product is long lived then direct atom counting techniques such as AMS (Accelerator Mass Spectrometry) or more standard techniques such as Inductively Coupled Plasma Mass Spectrometry (ICP-MS) or chemical separation can be used. The high sensitivity of these techniques ($\sim 10^{-15}$ for AMS and $\sim 10^{-6}$ for ICP-MS) allows one to be sensitive to very small numbers of atoms, thereby making the measurement of small cross sections feasible. If the experimental conditions are arranged such that the thin target approximation can be applied $Y = n\sigma$ (Equation 2.2), the cross section is simply given by

$$\sigma_{n,\gamma} = \frac{N_{A+1}}{N_A}\frac{1}{\phi t_{irr}} \tag{2.3}$$

where N_{A+1} is the number of nuclei $^{A+1}_{Z}X$ produced during an irradiation, and N_A is the number of target nuclei; ϕ is the neutron flux (n/cm^2/s) assumed to be constant over the area of the sample in the irradiation and over the irradiation duration, t_{irr}. By definition, with post-irradiation techniques there is no measurement of the energies of the neutrons that led to the reaction of interest; one obtains a spectrum averaged cross section:

$$\langle\sigma_{n,\gamma}\rangle_\phi = \frac{\int \sigma_{n,\gamma}(E_n)\phi(E_n)\mathrm{d}E_n}{\int \phi(E_n)\mathrm{d}E_n}. \tag{2.4}$$

The energy spectrum of the neutron source must therefore be well known, and well suited to the particular application for which the measurement is being made. If the cross section for a specific energy is to be determined and the neutron source is not truly mono-energetic, the energy dependence of the cross section in the relevant energy region must also be well known a priori; this may be acceptable for example where the cross section varies as $1/v$ for low energies, but more complicated variations with neutron energy must firstly be measured using the time-of-flight technique described below, or characterised with activation foils whose neutron capture resonances span the range of interest.

There are a number of advantages to using post-irradiation methods: unlike the cross sections obtained from resonance analyses made using the time-of-flight technique, activation measurements automatically include the direct capture component which for cases where the capture cross section is small can be significant. Sample impurities which would affect resonance analyses do not affect activation measurements, since these impurities in general do not affect isotopic ratio measurements. Systematic backgrounds associated with the prompt detection techniques below do not affect isotopic ratio measurements. Furthermore, irradiation samples can be placed very close to neutron sources, in some cases inside a nuclear reactor for example; this allows one to measure small cross sections and use small sample masses which in turn minimises the magnitude of the corrections described above. Finally, there are no complications that arise due to the multiplicity of the gamma-rays produced in a single capture reaction that otherwise makes counting the number of capture reactions non-trivial, discussed in the following Section.

The irradiation facility of choice for a particular measurement depends on the application. Research reactors produce the highest neutron fluxes of any facility, up to around 10^{14} neutrons/cm^2/s via fission. The associated neutron energy spectra are typically Maxwell-Boltzmann distributions with a mean energy of 25.3 meV (corresponding to a temperature of 290 K), although some reactors provide sources of colder neutrons. These sources are typically used for measurements relating to technological applications. Neutron beams (or fields) can be produced using low energy (< 15 MeV) beams of light charged particles, typically provided by Tandem accelerators; mono-energetic (or quasi mono-energetic) beams of neutrons with energies ranging from around 0.5 MeV to 24 MeV are produced from high Q-value reactions such as T$(p, n)^3$He, D$(d, n)^3$He or T$(d, n)^4$He. Sources of neutrons with 'quasi-stellar' Maxwell-Boltzmann energy distributions with mean energies in the keV range can be produced by the ^{7}Li$(p, n)^7$Be (mean energy 25 keV) and ^{18}O$(p, n)^{18}$F (mean energy 5 keV) reactions for example. These sources are primarily used for astrophysical studies.

2.3 Prompt detection techniques

The following techniques rely on measuring the prompt gamma-rays from the electromagnetic cascades depopulating the excited compound nucleus decaying to its ground state as a means of measuring the rate of reactions $C_{n,\gamma}$. The yield is given by

$$Y_{n,\gamma}(E_n) = \frac{C_{n,\gamma}(E_n)}{\epsilon(E_n)\phi(E_n)},$$

$$(2.5)$$

where ϕ is the neutron flux (defined here as the neutrons passing through the sample area per unit time), and ϵ is the efficiency for the prompt detection of the capture reaction which in general is not equal to the efficiency for the detection of the individual gamma-rays since in general many gamma-rays are produced for a single capture event. As illustrated in Figure 1.2 there are many possible cascades meaning that for each capture event, the multiplicity and energy of the gamma-rays is different although for some specific cases there may be characteristic gamma-rays that are produced in each de-excitation. One of the most important aspects of the detection system of choice is therefore that the detection efficiency should be independent of the cascade on an event-by-event basis; that is the efficiency should be independent of the cascade multiplicity and gamma-ray energy distributions.

There are three distinct prompt gamma-ray techniques discussed below; for a particular measurement the choice of technique depends on many factors such as the desired accuracy, the amount and possible radioactivity of the sample material, and on the neutron energy range of interest. It is most common for *γ-spectroscopic methods* to be used at mono-energetic or thermal neutron sources, whilst *total absorption calorimetry* and *total energy detection* are typically applied at white neutron sources in conjunction with the time-of-flight method, although in principle each of the following methods can be implemented at either mono-energetic or white neutron sources. A comprehensive review of prompt measurement techniques can be found in Reference [14].

γ-ray spectroscopy

Detectors with sufficient resolution, e.g. high purity Ge-detectors, can be can be used to perform level population spectroscopy, where the capture reaction rate can be determined by measuring either the individual primary gamma-rays depopulating the excited state upon neutron capture, or by measuring the gamma-rays feeding the ground state. This is only possible for a limited number of cases where the level scheme is both relatively simple and well known — in general therefore, this restriction limits the technique to light nuclei. This technique is routinely adopted at mono-energetic neutron sources where it is called Prompt Gamma-ray Activation Analysis (PGAA) — see References [15,16] for examples. One of the major advantages of this technique is that when the full resolving power of the gamma-ray spectrometer is utilised, the results are in principle not affected by systematic backgrounds such as scattered neutrons (the *neutron sensitivity*) which for the methods below need to be carefully subtracted from the overall count rate to avoid the overestimation of the capture yield. The analysis of specific gamma-lines also means that this method

is in general independent of any sample impurities which may affect the following methods.

Total absorption calorimetry

Total absorption calorimetry relies on the detection of all gamma-rays emitted in a capture event, meaning that total absorption calorimeters (TACs) are therefore built ideally in a 4π geometry and have 100% detection efficiency. In this way the total energy deposited in the detection system is proportional to the total energy of the capture cascade and is therefore independent of the cascade. Segmented detectors allow the multiplicity of cascades to be measured, and when coupled with high quality energy resolution, these systems provide a powerful means for counting capture reactions and rejecting undesired background events which in general have a lower multiplicity than capture cascades, and have a different deposited energy distribution. Examples include the TAC at the n_TOF facility composed of 40 BaF_2 crystals [17], and DANCE (Detector for Advanced Neutron Capture Experiments) at Los Alamos Neutron Science Centre (LANSCE), composed of 162 BaF_2 crystals [18]. The main advantages of this method are that TACs have good efficiency, powerful background rejection capabilities, ability to measure multiplicity, good energy resolution, and hence can be used also to study the characteristics of the γ-ray cascade. The main drawback of the method is that in general one needs to apply significant corrections to account for the sensitivity of the detectors to scattered neutrons, owing to the large amount of material associated with the detectors and their support structure.

Total energy detection

The total energy detection method (TED) seeks to measure the total energy of the cascade given by Equation 1.10 on an event-by-event basis, rather than measure the properties of the individual cascade gamma-rays. Knowing the excitation energy prior to the cascade, given in Equation 1.9, allows one to calculate the number of cascades and therefore the capture rate $C_{n,\gamma}$. The method was originally proposed by Maier-Leibnitz and first applied by Macklin and Gibbons [19]; it is based around a detection system with a low efficiency such that at most one of the gamma-rays from a cascade is detected in any given capture event and where the efficiency for the detection of a gamma-ray is proportional to its energy. These properties mean that the efficiency for detecting a capture cascade depends only on the initial excitation energy of the decaying nucleus, or equivalently on the total energy of the cascade — in this way, the efficiency is independent of the cascade. Whilst Moxon-Rae detectors

achieve this required proportionality to some degree, they fell into disuse because of non-proportionality below about 0.5 MeV, and due to their poor efficiency. Modern experiments use C_6D_6 detectors and artificially modify the efficiency of the detectors in software using the Pulse Height Weighting Technique (PHWT); further details are given in Section 3.6.1 and in References [20–22]. The main advantage of this technique is the insensitivity of the detection systems to neutrons. Such detection systems are routinely used at each of the neutron time-of-flight facilities discussed below. The TED method was used in this work, and the associated TED detection system used at n_TOF is described in Section 3.2.3.

2.4   The time-of-flight method at white neutron sources

The time-of-flight method coupled to one of the prompt detection techniques above allows the energy dependence of neutron induced reaction properties to be studied, including the complex resonant structures of reaction cross sections. The technique requires a pulsed neutron source providing neutrons across a wide range of energies, a *white neutron source* — examples of facilities housing such sources and neutron producing methods are given below. In a reaction cross section experiment, the neutron time-of-flight t_n corresponding to the time taken to traverse a fixed flight path length L is used to determine the neutron kinetic energy via the dispersion relation

$$E_n = m_n c^2 (\gamma - 1), \tag{2.6}$$

where m_n is the neutron mass, c is the speed of light and γ is given by

$$\gamma = \frac{1}{\sqrt{1 - (L/t_n)^2/c^2}}. \tag{2.7}$$

The time-of-flight is measured as the time difference between the initiation of the neutron pulse and the detection of the prompt reaction product(s) of interest corresponding to a single event, for example a gamma-ray cascade in a radiative capture event, with some suitable detection apparatus with good time resolution (typically < 1 ns). The neutron energy resolution, although dependent on energy and sample dependent to some degree, is typically $\delta E_n/E_n \sim 10^{-3}$ for the existing neutron time-of-flight facilities described below. This resolution is sufficient to allow precision cross section and resonance analyses for a wide range of isotopes across the nuclear chart. Further details of this technique relevant to the measurement made in this work are given in Chapter 3.

Pulsed neutron sources required for the time-of-flight technique are typically produced by pulsed beams of charged particles impinging on heavy nuclei targets resulting in either spallation or photo-disintegration reactions. At spallation sources, multi-GeV proton pulses impinge on a massive target such as Pb producing many reaction products including neutrons; time-of-flight facilities with such sources include n_TOF (CERN) (discussed at length in Chapter 3) and LANSCE (Los Alamos National Laboratory). Neutrons from photo-disintegration reactions are generated by impinging pulses of ~40-200 MeV electrons on targets with high atomic numbers such as U or Ta, thus generating a source of Bremsstrahlung radiation leading to reactions such as (γ, n), $(\gamma, 2n)$, (γ, f). Facilities housing such sources include GELINA at JRC-Geel and ORELA (now decommissioned) at Oak Ridge National Laboratory [23]. For both types of pulsed source, the neutron energy range is extended over multiple orders of magnitude via neutron moderation.

2.5 Surrogate measurements

In the most exotic cases of interest, the target nuclide may be toxic or intensely radioactive (or both). Manufacturing a target for a measurement may not only be impractical from a safety perspective, but may also be futile if the target has a very short half-life. In these cases, the methods described above are not feasible; a *surrogate* for neutron addition such as the single-neutron-adding (d, p) transfer reaction presents an alternative doorway into compound nucleus formation, which by the independence hypothesis decays independently of its formation channel. This allows one to perform experiments in inverse kinematics where a beam of the exotic isotope of interest is incident on a fixed deuterated target for example, in the case of a (d, p) reaction. In this way, if the decay from the compound nucleus via the channel of interest β is studied, the decay probability $P(\beta)$ of Equation 1.5 can be determined. An optical model calculation can yield the quantity $\sigma_{CN}(n)$ (typically to a higher degree of accuracy than possible for calculations of $P(\beta)$) which when combined with the measured $P(\beta)$ yields the cross section of interest as per Equation 1.5, or at least helps to constrain the value of the desired cross section. Historically, surrogates for radiative neutron capture have presented difficulties due to the mismatch between the distributions of spin-parity populated in the surrogate and 'real' neutron capture reactions, but recent theoretical advances have improved the accuracy of the technique, see References [24,25]. The surrogate approach may be associated with either a prompt or post-irradiation measurement technique.

2.6 Normalisation

For post-irradiation and prompt methods alike, the absolute value of the flux ϕ (or absolute normalisation of the shape of the neutron flux $\phi(E_n)$) is typically the largest source of uncertainty associated with the measured yield Y, and the deduced cross section. It is usual to make auxiliary measurements of samples whose cross sections are well known, or considered 'standard' [26]. For post-irradiation techniques, this is typically performed by activating small foils of known composition and mass (e.g. Au, Cu, Zr) in close proximity to the sample of interest during the irradiation, before performing an analysis of the activated gamma-ray lines (with known half-lives and branching ratios). Details of this procedure are given in Section 4.3.2 in relation to the irradiation+AMS measurement made in this work. For prompt measurements, the philosophy is similar; samples whose cross sections are standard across a wide range of neutron energies are used to deduce the shape of the neutron flux $\phi(E_n)$ — this procedure is discussed in Section 3.2.1 for the time-of-flight measurement in this work.

For prompt measurement techniques using the time-of-flight technique, the most common method to perform the final absolute normalisation of the reaction yield is to use the *saturated resonance method* (SRM) [27]. This accounts for the absolute values of the efficiency of the detection system ϵ and the absolute normalisation of the neutron energy spectrum ϕ (both of which depend on precise geometries and sample/detector positions). The SRM involves measuring a sample of the same size as the sample of interest, which has a strong isolated resonance where $\Gamma_n \ll \Gamma_\gamma$. In this case, if the sample is chosen such that the product of the areal density and cross section is large enough, all neutrons with energies near that of the resonance are captured by the sample, meaning that for this 'saturated resonance' the capture yield $Y \approx 1$; an example is the 4.9 eV resonance in ^{197}Au. This allows one to combine the absolute normalisation (which is geometrical and sample independent) into a single factor that can be applied to the measured yield for the sample of interest, by comparing the measured yield at the saturated resonance to the calculated value. Further details of this procedure are given in Section 3.8.2 for the measurement performed in this work.

2.7 Measurable quantities

The simplest measurements are those where a cross section at a particular energy or a spectrum averaged cross section is desired; these measurements were already discussed.

The most complicated are the high-resolution measurements seeking to obtain the point-wise cross section in the resolved resonance region (RRR) using the time-of-flight technique. In addition to the experimental effects described in Section 2.1 (multiple scattering and self-attenuation), Doppler broadening and effects due to the moderation of neutrons in the neutron producing target of white neutron sources also act to change the measured shapes of resonances — the specifics of these resolution effects are discussed in Section 3.2.2. As discussed in Section 1.2, the cross section in the RRR can be parametrised in terms of the partial widths, total widths, energies and spins of resonances. These parameters are independent of any effects associated with a specific experimental set-up, and their measurement is therefore the goal of a cross section measurement of the RRR. In principle, if the neutron energy resolution of the time-of-flight facility is sufficient, a combination of the capture measurement and a transmission measurement[1] can be used to uniquely determine each of the resonance parameters. For most resonances however, the neutron energy resolution of the time-of-flight facility is larger than the natural width of the resonances meaning that the partial widths ($\Gamma_n, \Gamma_\gamma, \ldots$) can not be uniquely determined due to their strong correlation. In a single capture experiment therefore, in general it is only the area of the resonances given by

$$A_{n,\gamma} = 2\pi^2 \lambdabar^2 g \frac{\Gamma_n \Gamma_\gamma}{\Gamma} = 2\pi^2 \lambdabar^2 \kappa \qquad (2.8)$$

that can be measured. Here $\kappa = g\frac{\Gamma_n \Gamma_\gamma}{\Gamma}$ is the capture kernel and the other symbols were defined in Section 1.2. If $\Gamma_n[\Gamma_\gamma] \gg \Gamma_i$ where i represents any of the other partial widths, then $g\Gamma_\gamma[g\Gamma_n]$ can be measured. If the spin factor g is known (the spin of the resonance is known), the partial width $\Gamma_\gamma[\Gamma_n]$ can also be determined.

To obtain these parameters from the experimental yield, codes such as SAMMY [28] or REFIT [29] are typically used which account for the convolution of the various experimental effects mentioned above, and which can also be used to perform a full R-Matrix analysis of the experimental yield; both codes start from an initial set of resonance parameters (usually taken from an existing data evaluation such as ENDF) from which an iterative procedure yields the best fit resonance parameters, and hence resonance kernels.

In addition to resonance parameters for the RRR, point-wise cross sections can be deduced from the reaction yield in the URR, typically via the thin-target approximation as $\sigma = Y/n$ (see Equation 2.2), and where a correction is applied to account for the over/underestimation of the yield because of the effects discussed above. In a similar

---

[1]Transmission measurements yield the transmission factor T defined in Equation 2.2, which in turn allows the total cross section to be measured.

way, the thermal cross section can also be directly measured from the reaction yield, although it is more usual to perform a dedicated thermal measurement using a source of thermal neutrons where in general systematic uncertainties are smaller.

Chapter 3

^{35}Cl radiative capture cross section measurement at n_TOF

3.1 Applications, motivation and objectives

The ^{35}Cl(n, γ) cross section has multiple applications: medical physics in the context of the novel cancer treatment, Boron Neutron Capture Therapy (BNCT); nuclear waste management relating to the current generation of reactors; and in nuclear astrophysics. These applications are summarised below:

BNCT cancer therapy is based around the selective uptake of ^{10}B in malignant cells due to their enhanced metabolism, delivered to the patient by means of the boronated amino-acid, boron-phenylalanine [30]. Irradiating the area with neutrons can lead to the ^{10}B(n, α) reaction from which the ionising reaction products deliver a precisely located dose to the tumour (within around 10 μm of the reaction site), and the non-ionising neutrons mostly pass through the body without interacting thereby reducing the dose to healthy tissue. BNCT is currently being considered more seriously as an option for future cancer therapies, based on the most recent clinical results associated with brain tumours and head and neck cancers [30–32]. Although the total dose rate is dominated by the ^{10}B(n, α) reaction, there is inevitably a dose delivered to the surrounding healthy tissues from other mechanisms; in any radiotherapy treatment it is these undesired dose components that ultimately limit the viability of the treatment. For BNCT these other mechanisms are dominated by the elastic scattering of neutrons on the abundant isotope ^{1}H, but also include the ^{1}H(n, γ), ^{14}N(n, p) and ^{35}Cl(n, γ) reactions. Monte-Carlo simulations have indicated that for brain tumour treatments the dose rate from ^{35}Cl(n, γ) accounts for around 11% of the total dose to the brain for neutron energies in the range 100 eV - 10 keV [33]; in BNCT clinical trials, and indeed

more generally in any future roll-out of the technology, the Monte-Carlo simulation based therapy planning systems rely on accurate cross section data to achieve the most reliable planning and best therapeutic outcomes. The International Commission on Radiation Units and Measurements (ICRU) recommends that the radiation dose delivered should be within 5% of the prescribed dose, therefore requiring cross section uncertainties significantly below 5%.

Graphite moderated reactors are commonplace in the UK and across Europe, Asia and North America, following on from the first nuclear reactor to achieve criticality, Chicago Pile-1, which did so in 1942 with graphite bricks as the moderator. The United Kingdom in particular embraced graphite as a moderator; initially for MAGNOX reactors [34] and later for Advanced Gas-cooled Reactors (AGRs) [35]. ^{35}Cl is present in commercial nuclear reactors, both in the fuel cladding (2-5 ppm by weight) and also as an impurity in the graphite moderator (<2 ppm by weight). Irradiated graphite contains multiple activation products including ^{14}C (see Chapter 4) and ^{36}Cl which are both long-lived and by their chemical nature it may be possible for them to escape from a future geological disposal facility (GDF) and into the wider biosphere, potentially contributing to public doses. Currently in the UK, irradiated graphite makes up 23% of the intermediate level nuclear waste, amounting to a volume of approximately 67,000 m^3 weighing 83,000 metric tonnes with a further 14,000 tonnes classed as low level nuclear waste [36]; it is therefore paramount to be able to predict the amounts of these radionuclides present in nuclear waste to allow for its safe disposal — this relies on accurate knowledge of the reaction cross sections. The final ^{36}Cl content of irradiated nuclear graphite is mostly sensitive to the thermal cross section [37], but the final uncertainty associated with the ^{36}Cl content is also dependent on the reaction cross section uncertainties in the resolved resonance region at larger neutron energies, as was shown by a sensitivity study by Taylor *et al.* [38].

Finally, ^{35}Cl has a role in the astrophysical s-process, a series of successive neutron captures and beta decays, one of the primary mechanisms in the generation of the heavy elements beyond Fe in stellar environments [39, 40]. The s-process is driven by neutrons produced in the ^{13}C$(\alpha, n)^{16}$O and ^{22}Ne$(\alpha, n)^{25}$Mg reactions. Isotopes of high abundance (i.e. lighter nuclei) or those with large neutron absorption cross sections affect the efficiency of the neutron recycling in the s-process by removing neutrons from the stellar environment; they act as 'neutron poisons'. Being relatively abundant, ^{35}Cl (the 17th most abundant in the solar photosphere [41]) is classed as a 'minor neutron poison' and the neutron capture cross section averaged over stellar neutron energy spectra are required to assess its impact on the s-process. The relevant energy range for stellar applications covers entire resolved resonance region, spanning neutron energies up to several 100 keV.

There have been two previous precision time-of-flight measurements of the $^{35}Cl(n, \gamma)$ cross section and associated resonance analyses, those of Macklin *et al.* [42] and Guber *et al.* [43]. Only the Guber measurement reported the cross section below 4 keV, implying the existence of just a single data set for neutron energies < 4 keV. The cross section reported in the evaluated nuclear data libraries ENDF/B-VIII.0 and JEFF-3.3 are both based on an evaluation by Sayer *et al.* including these two datasets as well as previous measurements of the total neutron cross section [44]. For neutron energies > 4 keV the Sayer evaluation (based heavily on the Guber measurement) and the Macklin measurement report capture resonance kernels that consistently differ by around 15%. Both of these measurements were performed at the neutron time-of-flight facility ORELA at Oak Ridge National Laboratory. It is therefore clear that for the applications above, a new precision measurement may not only lead to a reduction of the uncertainty associated with the evaluated reaction cross section, but may also resolve the discrepancies of the individual data-sets therein. Moreover, the stellar averaged cross sections derived from the two previous time-of-flight measurements are inconsistent with a recent measurement made via AMS [45] further prompting a new measurement at a different experimental facility.

Objectives

The objectives of this portion of work were to obtain a neutron capture reaction yield up to an energy of 200 keV with minimal uncertainty, covering the neutron energies relevant to each of the applications above, using the total energy detection system at the neutron time-of-flight (n_TOF) facility at CERN. The resonance parameters for any resolved resonances are desired, to be obtained via an R-Matrix analysis of the reaction yield accounting for the complex response of the time-of-flight spectrometer. Where the resonances are unresolved, the average cross section is desired. An accurate assessment of the systematic uncertainties associated with the measurement is also required, which can be reported with the yield to EXFOR, to be incorporated in a future evaluation of the cross section. In general for light nuclei, the capture cross section is small meaning that any systematic background associated with a measurement may become prohibitive; a comprehensive study of the background components at n_TOF required for the measurement of such nuclei is also the objective of this work, which may serve as a basis for future background optimisation and also for planning future experiments, since at n_TOF there has only been one previous capture measurement campaign concerned with Mg isotopes [46]. Finally, a quantitative comparison of the results to those of previous measurements and evaluations will be made, as well as an

assessment of the impact of the n_TOF measurement on each of the aforementioned applications.

3.2   Experimental set-up at the n_TOF facility, CERN

The neutron time of flight facility at CERN was commissioned in 2001 and grew out of a research programme in the late 1990's seeking to demonstrate the feasibility to destroy, or 'transmute', long-lived fission products in Accelerator Driven Systems (ADS) [47]. The experiences gained during these experimental campaigns led to a proposal by Rubbia for the n_TOF facility with the aim of producing a facility capable of measuring neutron induced reaction cross sections over a wide energy range spanning eleven orders of magnitude from thermal to GeV neutron energies, covering energy ranges relevant to stellar and Big Bang nucleosynthesis, medical physics, nuclear energy technologies, and other basic nuclear physics [48]. There have been three phases of operations, each one leading to improvements in the capabilities of the facility and the range of measurable isotopes; the measurement in this thesis was made during Phase III which commenced in 2014. A complete description of the facility and its history can be found in References [49, 50]; a brief description is given here.

At n_TOF, nominal pulses of $\sim 7 \times 10^{12}$ protons (*dedicated* beam mode) of 20 GeV/c momentum and a temporal width of 7 ns (root mean square) from CERN's Proton-Synchrotron (PS) impinge on a fixed ~ 1 tonne cylindrical Pb target generating around 300 neutrons per proton via spallation reactions, see Figure 3.1. In total, around 5.5×10^5 neutrons per nominal pulse reach the experimental measuring station used in this work. There is also a *parasitic* beam mode with around half the intensity of the dedicated pulses. For each spallation reaction on a lead nucleus, several energetic particles are created which lead to an internuclear cascade producing many highly excited nuclei which decay predominantly by neutron emission, since neutrons do not experience a Coulomb barrier. The lead target is cooled with a 1 cm thick jacket of water encased in an aluminium tank, and a further 4 cm layer of water or borated water (H_2O +1.28%H_3BO_3 by mass) acts to further moderate the spallation neutrons (MeV-GeV energies) in order to produce a white spectrum ranging from thermal energies to multi-GeV. There is a low neutron pulse repetition rate of 0.4 Hz in order to avoid wrap-around events where neutrons from separate pulses overlap, and also to respect the limits on the spallation target heating. Furthermore, the low duty cycle but intense proton pulses results in an enhanced signal-to-background ratio relative to the alternative case of a large duty cycle, but lower intensity beam structure.
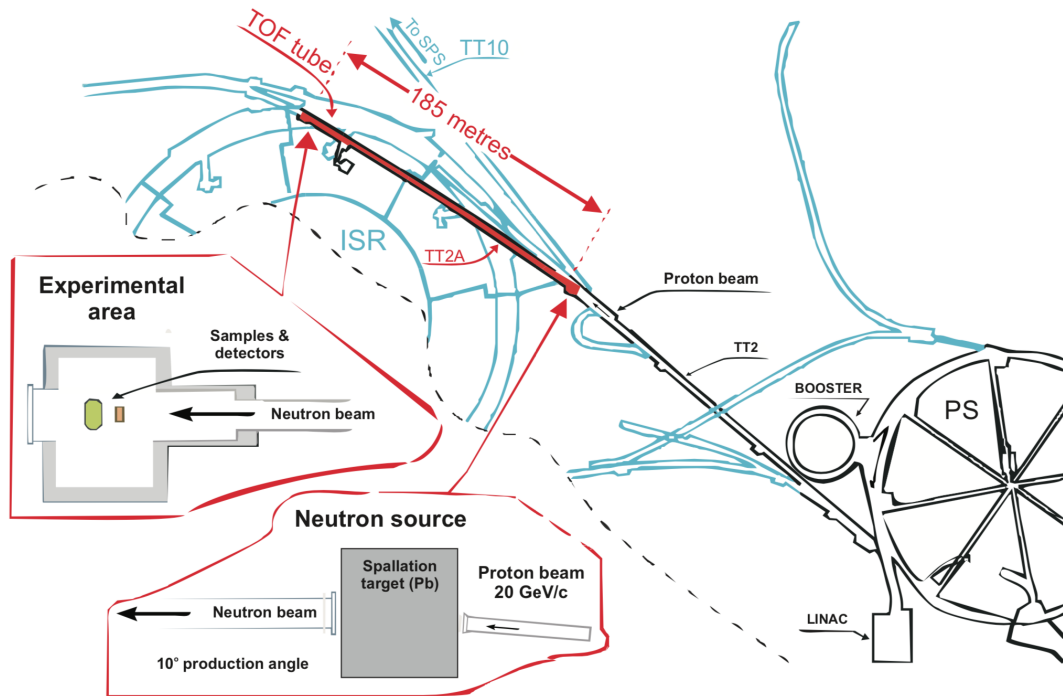
FIGURE 3.1: Schematic of the n_TOF facility as part of the CERN accelerator complex. Protons are accelerated through the LINAC, PS-Booster, PS (proton synchrotron) chain up to 20 GeV/c and are directed onto the n_TOF spallation target, generating neutrons which traverse the 185 m horizontal flight path to Experimental Area 1 (EAR1) (and a second 20 m vertical beamline leading to Experimental Area 2 (EAR2) not shown in the figure).

Since 2014 there are two neutron flight paths: the original 185 m horizontal beam line leading to *Experimental Area I* (EAR1), and a second 20 m vertical beam line leading to *Experimental Area II* (EAR2) [51, 52]. The longer flight path is more suitable for measurements where precision resonance analyses are to be made since there is a larger dispersion in time-of-flight for a given neutron energy interval, but also naturally results in a lower instantaneous neutron flux. The shorter flight path leads to a more degraded neutron energy resolution and ability to resolve closely spaced resonances, but the much increased neutron fluence (around 40× that of EAR1) means that more intensely radioactive samples can be measured where required, as a result of the more favourable signal-to-background ratio. The relative merits of EAR1 versus EAR2 are evaluated on a case by case basis; for this work EAR1 was used since the sample was not radioactive, and a precision resonance analysis was the goal of the experiment.

The spallation products enter the beam-lines evacuated to $< 10^{-2}$ mbar; the EAR1 beam-line is depicted in Figure 3.2 and is described here. After the spallation target, a filter station is positioned before the first collimator, and contains removable slabs of materials that have very strong neutron absorption resonances which effectively

remove all neutrons from the beam at the energy of these resonances; this is useful for evaluating background components and is further discussed in Section 3.7. The undesired charged spallation products are swept out of the beam by a 3.6 Tm dipole magnet positioned around 145 m from the spallation target, and two collimators shape the beam. The second collimator can be changed depending on the measurement requirements, with an 18 mm diameter circular collimator for capture measurements where in general a more well defined beam is required and where thicker targets are used, and an 80 mm collimator for fission measurements where in general targets of large diameter and minimal thickness are used to minimise fission fragment stopping and energy straggling. The resulting approximately Gaussian beam profile for the capture set-up is discussed in Section 3.2.1. Additional sections of concrete shielding covering the cross-section of the beam tunnel act to prevent other particles from travelling to the experimental area outside of the beam tube. Finally, the beam dump is composed of a polyethylene cube of side 50 cm, with additional cadmium foils such that backscattering towards the experimental bunker is minimised.
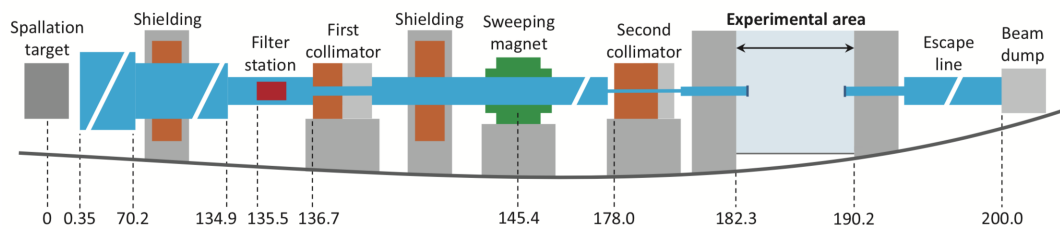
FIGURE 3.2: Schematic of the 200 m n_TOF EAR1 horizontal beam line, not to scale. Distances from the spallation target are given in m.

Background and prompt spallation products

Minimising the sources of undesirable in-beam spallation products is paramount to ensure that the measurement of interest is not dominated by background — this is challenging being within such close proximity to a spallation source. With each proton pulse there is a burst of relativistic particles aside from neutrons, whose passage to the experimental area is minimised through many stages of shielding and collimation. The 10° angle at which the proton beam impinges on the lead target significantly reduces the quantity of forward-focussed spallation products (photons, muons, pions etc.) entering the beamline, in addition to the fraction of the proton beam that does not stop within the lead target. Moreover, the choice of borated water as the moderator significantly reduces the source of 2.2 MeV gamma-rays from the $^{1}H(n, \gamma)$ reaction at thermal neutron energies (the dominant source of in-beam photons) as low energy neutrons are preferentially used up in the $^{10}B(n, \alpha)$ reaction which has a very large

thermal cross section. The reduction of in-beam photons in this way comes at the expense of a significantly reduced thermal and epi-thermal flux, shown in Figure 3.3.

Despite measures for their reduction, there is nevertheless an unavoidable number of in-beam ionising particles: gamma-rays originating from neutron capture on the moderating materials surrounding the spallation target (dominated by 478 keV from $^{10}B(n,\alpha)^{7}Li^{\star}$ reactions, 511 keV from pair annihilation, and 2.2 MeV from $^{1}H(n,\gamma)$), particles from the in-flight decay of short-lived spallation products, and charged particles produced by the interaction of high energy neutrons and photons with the second collimator. Collectively, these prompt particles (arriving at the experimental area in $< 1\ \mu$s) produce a response in any detection system placed in the experimental bunker, the so-called γ-flash. The one redeeming feature of the flash is that it serves as a precise reference for the time of each proton pulse on target which can be used for determining the kinetic energy of neutrons corresponding to subsequent detected events. The response of the detectors used in this work to the flash is discussed in Section 3.2.3. Further sources of background include sources of radiation in the absence of the neutron beam and the scattering of neutrons and in-beam photons in the experimental bunker from the sample and surrounding materials; the relative contributions of each source varies as a function of time-of-flight — a complete description of the individual background sources is given in Section 3.7. For capture measurements, where gamma-rays are detected, these background sources can be prohibitive if the capture cross section of the isotope being studied is relatively low in magnitude and/or small relative to the neutron scattering cross section, as were both the case in this work (see Figure 1.1); this can lead to an enhanced background due to scattered neutrons interacting with the surrounding materials, also discussed in Section 3.7.

3.2.1 Neutron beam characteristics

The production of an experimental yield for any cross section measurement relies on an accurate characterisation of the neutron flux; indeed the flux is often the dominant source of uncertainty. There have been multiple concerted efforts within the n_TOF collaboration to perform this characterisation, the details of which can be found in References [50, 53]; a summary of the essential characteristics of the beam relevant to this work and its measurement at EAR1 are given below.

Neutron flux

For a cross section measurement, it is the shape of the neutron flux that is most important rather than its absolute value as measurements are typically made relative to a well known *standard* cross section [26] (e.g. ^{197}Au for capture measurements or ^{235}U for fission measurements), as was the case in this work. At n_TOF, a series of dedicated measurements of the neutron flux have been made using multiple detector technologies each with different operating principles and systematics, measuring samples where their cross sections are considered 'standard' by the IAEA [26]; the neutron flux is determined using Equations 2.2 and 2.5. The measurements made were the following:

- ^{235}U(n, F) (standard over E_n = 0.15-200 MeV): measured using a position sensitive MicroMegas detector (MGAS) [54], PPAC (Parallel Plate Avalanche Counter) [55], and the PTB 'H19' fast fission chamber (Physikalisch-Technische Bundesanstalt) [56].

- ^{10}B(n, α) (standard over E_n = 25 meV-1 MeV): measured using MGAS.

- ^{6}Li(n, t) (standard over E_n = 25 meV-1 MeV): measured with the SiMon (Silicon Monitor) detectors [57], permanently installed for flux monitoring. The SiMon detectors were also used in this work for flux verification, see Sections 3.2.4 and 3.8.1.

These measurements were compared and combined with accurate Monte-Carlo simulations (FLUKA and MCNP) to produce an *evaluated flux*, which for EAR1 is shown in Figure 3.3 with isolethargic binning[1]; the definition of the neutron flux here is the number of neutrons integrated over the whole beam profile at the entrance to the experimental bunker (around 182 m from the spallation target) per energy bin per nominal proton pulse of 7×10^{12} protons.

The essential features of the flux include the dominant peak around 1 MeV, typical of neutron evaporation from the hot spallation products, and the peak around thermal neutron energies, 25.3 meV, corresponding to thermalisation in the moderator. Below around 1 MeV, the flux varies isolethargically, close to $1/E_n$ typical of a moderated neutron spallation source[2]. The dips in this intermediate region arise from resonant

---

[1]For the flux here, and later for time-of-flight histograms that span multiple orders of magnitude, *isolethargic binning* is used such that for any histogrammed quantity, structures at all energies or times-of-flight can be resolved. Histogram bin widths have equal logarithmic width w such that $\log E_{low} + w = \log E_{up}$ where E_{low} and E_{up} are the lower and upper bin boundaries.

[2]The *neutron lethargy*, the average logarithmic energy-loss per collision, is constant in a perfect moderator — a plot of the moderated neutron flux over the logarithm of energy is therefore flat in the ideal case — this behaviour is evident in the n_TOF flux.
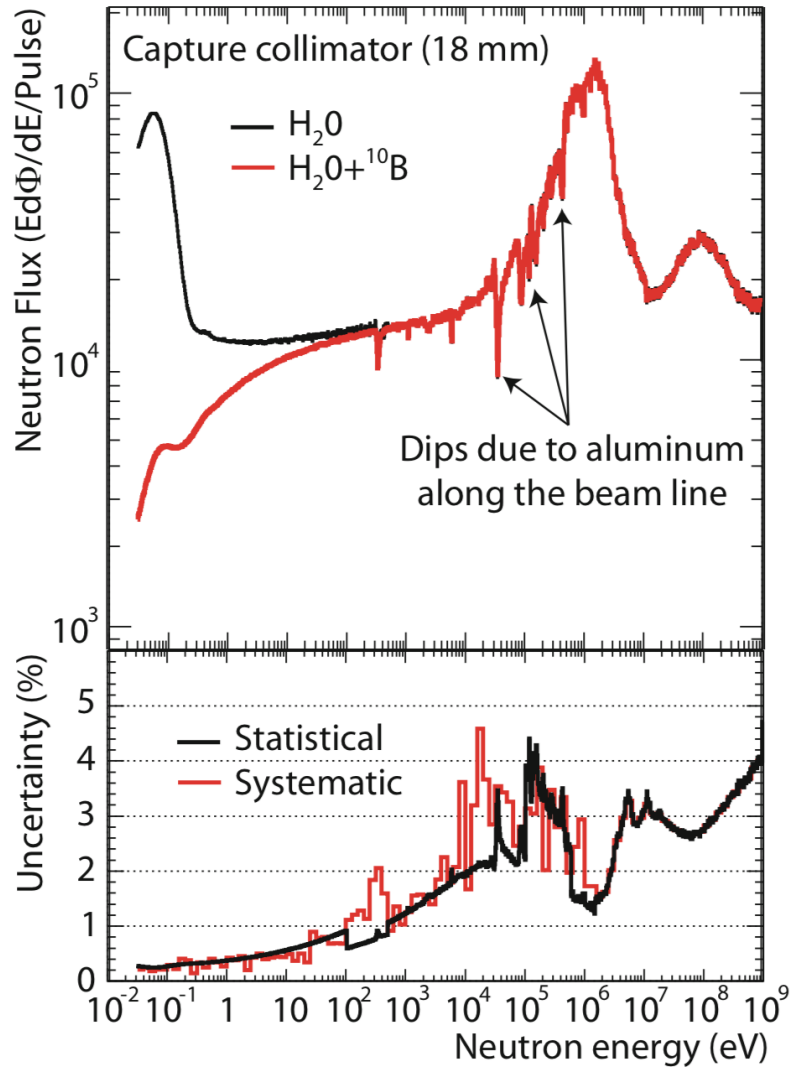
FIGURE 3.3: Evaluated neutron fluxes at EAR1 for the case of non-borated and borated water moderators with the 18 mm capture collimator, shown with 100 bins per energy decade, with associated uncertainties. Figure from Reference [50].

absorption by ^{27}Al used for the windows of the evacuated beam-line and of the spallation target and water moderator circuit assembly. One must take care when a cross section measurement or resonance analysis are to be performed close to the regions around these dips.

The statistical uncertainty shown in Figure 3.3 is calculated in the usual fashion from the combination of each of the individual flux measurements. The different measurements are normalised at the thermal point ($E_n = 0.0253$ eV) and the systematic error is then estimated by calculating the r.m.s. of the different measurements for each energy bin, and is therefore more indicative of the uncertainty associated with the overall shape of the flux; this is the lower limit of the cross section uncertainty achievable in this work since the cross section was made relative to the standard cross section of ^{197}Au meaning that the absolute value of the flux is not as relevant.

The uncertainty increases in general with increasing neutron energy since for each of the individual flux measurements, the counting statistics diminish with neutron energy due to the overall $1/v$ dependence of the reference cross sections listed above coupled with a rough $1/E_n$ dependence of the neutron flux, at least over the region 1 eV $\leq E_n \leq 10^4$ eV (note the flux shown here is in units of lethargy). Where statistics are enhanced, e.g. at the ~1 MeV peak, the uncertainty is smaller and conversely for the regions around the aluminium absorption resonances, the uncertainty is larger. Year-by-year, the precise boron content of the moderator circuit changes meaning that the low energy flux must be monitored in each experiment, details of this procedure are given in Section 3.8.1. For this reason the uncertainty associated with the lower energy flux is estimated to be larger than is shown in Figure 3.3. The overall uncertainties on the flux adopted in this work are shown in Table 3.1.

TABLE 3.1: Overall systematic uncertainty estimates associated with shape the neutron flux adopted in this work, with the borated water moderator.

Neutron energy range	Uncertainty (%)
25 meV to 100 eV	2
100 eV to 10 keV	2
10 keV to 1 MeV	4
1 MeV upwards	3

Beam profile and interception factor

The EAR1 beam profile is shown in Figure 3.4, and was also determined using a combination of measurements using a 2D pixelated MicroMegas detector [54], and Monte-Carlo simulations. For the 18 mm capture collimator, the beam is approximately Gaussian, with width $\sigma \approx 0.7$ cm. The beam profile is crucial for calculating the flux integrated over the sample area $\phi(E_n)$ used to calculate the reaction yield in Equation 2.5. $\phi(E_n)$ is given by the product of the flux in Figure 3.3 with the *beam interception factor* (BIF) defined as fraction of the beam that intercepts the target, shown in Figure 3.4 for different diameter targets. The decline at the lowest neutron energies (< 0.1 eV) is due to the effect of gravity on the slowest neutrons as they traverse the horizontal beam line meaning that they 'miss' the target; for reference, thermal neutrons arrive at the experimental bunker around 85 ms after GeV neutrons. The increase at energies > 1 MeV is a result of the more forwards-peaked neutron production leading to a narrower beam and therefore an increased BIF. In between, from around 0.1 eV to 100 keV, the BIF is constant to within around 1%. For capture experiments this generally covers the entire range of interest meaning that the systematic change in the BIF is not significant; this was the case for this measurement. The systematic change is
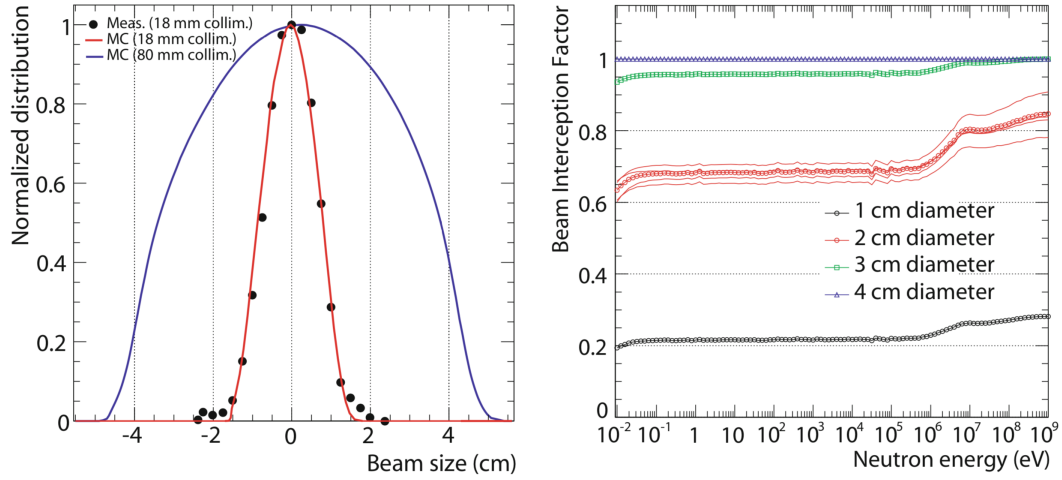
FIGURE 3.4: (Left) Measured beam profile projection in the vertical plane for neutron energies 0.1-1 eV, with associated Monte-Carlo (MC) simulations for both collimator sizes. (Right) Beam interception factor as a function of neutron energy for different sized circular samples at the nominal measuring position. The lines either side of the data points for the 2 cm diameter sample (the size of the sample in this work) correspond to the effect of moving the sample left/right or up/down by 1 mm with respect to the nominal position. Figure adapted from Reference [50].

dominated by the effect of a misalignment, shown in Figure 3.4 for 2 cm diameter samples (as were used in this work), where it is shown that a 1 mm misalignment of the sample can result in a change of up to 3%. For the case where a measurement is made relative to a standard cross section (^{197}Au in this work) using the saturated resonance method (SRM), both samples must intercept the same fraction of the beam making this alignment crucial. The SRM was applied in this work, and is discussed in Section 3.8.2; due to uncertainties relating to the sub-mm alignment of samples, the BIF therefore represents one of the largest sources of systematic uncertainty. The alignment of the samples is discussed in Section 3.3.

3.2.2 Neutron kinetic energy determination and resolution

The neutron kinetic energy associated with each detected event is calculated using Equation 2.6 in the case where the flight path L is fixed. For a given event, the time of the γ-flash t_γ from the corresponding neutron pulse generation is measured (the time at which light arrives at the detector from the neutron producing target following a proton pulse, see Figure 3.8) in addition to the time of the event t; the neutron time-of-flight is given by

$$t_n = t - t_\gamma + L/c \tag{3.1}$$

where for the case of EAR1 at n_TOF, $L/c \approx 620$ ns depending on the exact position of the detectors. The associated energy resolution is limited by several factors:

- The temporal width of the proton beam, 7 ns r.m.s. at n_TOF

- The time resolution of the detectors used to measure t and t_γ, this is negligible for the detectors used in this work, being on the order of 1 ns.

- The relative thermal motion of the incoming neutron and target nuclei results in a Doppler broadened time-of-flight or neutron energy spectrum, especially important for resonance analyses. The broadening can be described by the Free Gas Model where the Gaussian broadening has width

$$\sigma = \sqrt{2k_B T_{eff} E_n A / (A + 1)} \tag{3.2}$$

where A is the mass of the target nuclei, E_n is the neutron energy and $T_{eff} \approx \frac{3}{8}\Theta \coth(\frac{3\Theta}{8T})$ where Θ is the Debye temperature and T is the temperature. The broadening only affects the shapes of resonances, not their positions, and the effect is minimised by keeping the temperature constant inside the experimental bunker (295 K in this work). The effect is taken into account in the resonance analysis.

- The uncertainty relating to the fixed flight path length L affects the position of resonances, but not their shape. The ≈ 185 m geometrical flight path length is calibrated to within around 1 cm using a sample where the resonance energies are well known; see Section 3.5.3.

- The least trivial effect relates to the moderation of neutrons in the neutron producing target assembly. For a given neutron energy, there is a distribution of moderation times that neutrons spend inside the neutron producing target assembly (or equivalently moderation distance), referred to as the *resolution function* (RF). The relationship between the measured time-of-flight and the true neutron energy described by Equation 2.6 is modified in a non-trivial way; the result is that the shapes and positions of resonances are also modified, as shown in Figure 3.5. This effect depends heavily on the experimental facility and the neutron production mechanism. The RF cannot be directly measured, so Monte-Carlo simulations are performed, which also include the effect of the 7 ns proton pulse width. The simulations were subsequently verified by comparing calculated experimental yields with experiment for well known resonances. It was shown in Reference [58] that the time-to-energy dispersion relation of Equation 2.6 can be corrected by the addition of a constant time offset to the measured time-of-flight; this accounts for the shift of the resonances as a result of the resolution function, but resonances still appear broadened. This residual effect is dealt with in the resonance analysis by using the simulated shape of
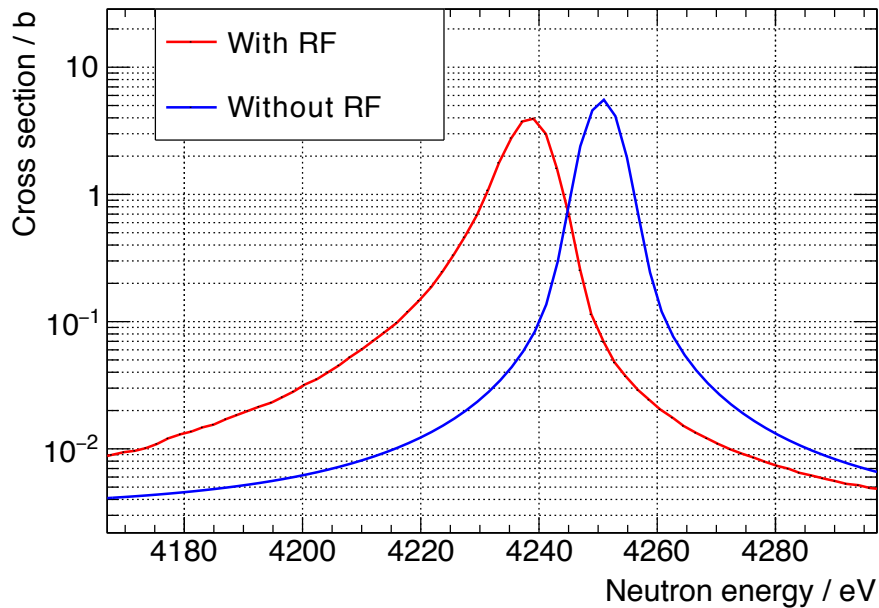
FIGURE 3.5: Example of the effect of the n_TOF resolution function (RF) on the 4.25 keV resonance of ^{35}Cl. The calculation was performed with SAMMY [28]. The tail to lower energies for the case where the RF is included is due to the scattering of neutrons in the neutron producing target, increasing their measured time-of-flight.

the RF. The time offset t_{off} and the geometrical flight path L are calibrated simultaneously, see Section 3.5.3.

The relative contributions to the neutron resolution from each of the components above are shown in Figure 3.6 with respect to the neutron energy. In principle, resonances of ^{35}Cl up to around 1 MeV should be resolvable, but as will be shown, for this measurement it was not the resolution that limited the measurement of resonances, but the background which was prohibitively large meaning that only the strongest resonances were measurable.

3.2.3 Legnaro-C_6D_6 Total Energy Detection set-up

As briefly discussed in Section 2.3, a challenging aspect of radiative capture measurements is how to count the number of capture reactions from the measured single gamma-rays: since there are many possible gamma-ray cascades following the capture of a neutron, composed of different numbers of gamma-rays with different energies, it is not enough to simply count individual gamma-rays. The solution is to (artificially) make the detection efficiency independent of the cascade, and sensitive only to the total energy of the cascade (or equivalently, the excitation energy of the compound nucleus following neutron capture). This measurement was made using the total energy detection (TED) method, which achieves this cascade independence.
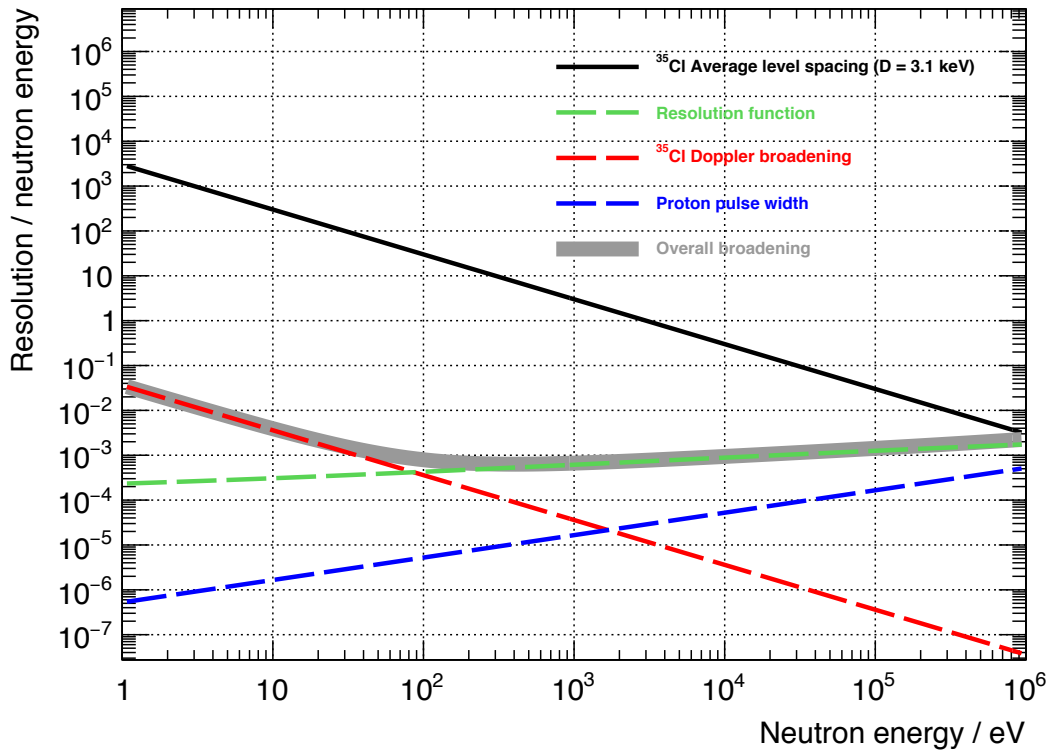
FIGURE 3.6: Relative neutron energy resolution from each contributing factor. The average level spacing of ^{35}Cl is shown, and is larger than the overall broadening over the whole energy range of interest.

A mathematical description is given below, but in summary the method works on the principle that if the efficiency for the detection of a particular gamma-ray is proportional to its energy, and is such that at most one gamma-ray is detected per cascade, then over a large number of capture events for which gamma-rays are detected, the amplitude of the gamma-ray counting spectrum as a function of neutron energy is proportional to the number of capture events. The proportionality of the efficiency to the gamma-ray energy is achieved through a weighting procedure, applied in software, such that more energetic gamma-ray counts are 'weighted' more than less energetic gamma-rays, since the true gamma-ray detection decreases with increasing gamma-ray energy — this is called the Pulse Height Weighting Technique (PHWT).

The mathematical principle of the method is as follows:

If the efficiency to detect a given gamma-ray in a given capture cascade is ϵ_i, the probability that the capture event is detected through the detection of one or more gamma-rays is given by

$$\epsilon_c = 1 - \prod_{i=1}^{i=M}(1 - \epsilon_i), \tag{3.3}$$

where M is the multiplicity of the cascade; ϵ_c varies depending on the particular cascade pattern (which may also vary as a function of incoming neutron energy) resulting in a poorly defined neutron capture detection efficiency, $\epsilon(E_n)$ in Equation 2.5. If some suitable gamma-ray detection system satisfies the two conditions that its efficiency $\ll 1$ and is also proportional to the energy of the gamma-ray, $\epsilon_i = kE_\gamma$, then keeping terms only up to first order in ϵ_i

$$\epsilon_c \approx \sum_{i=1}^{i=M} \epsilon_i = \sum_{i=1}^{i=M} kE_i. \qquad (3.4)$$

Neglecting internal conversion for the moment (which would otherwise lead to 'missing' excitation energy, see further discussion in Section 3.6.2), if the constant k is chosen to be 1 MeV^{-1} then the efficiency becomes equal to the excitation energy, or *total energy* of the cascade:

$$\epsilon_c = E^\star = S_n + E_n^{CM}, \qquad (3.5)$$

as per Equation 1.10, independent of the specific cascade path. The end result is a well defined efficiency that can be used to calculate the reaction yield given by Equation 2.5.

The application of the technique leads to a number of requirements of the detectors that are used, the most demanding of which is that the efficiency be proportional to the gamma-ray energy — this is in general not the case for materials used for gamma-ray detectors; the solution is to use the *Pulse Height Weighting Technique* (PHWT) where the efficiency is artificially modified in software, discussed and applied to the data in Section 3.6. Further general detector requirements for capture measurements are: the sensitivity to neutrons scattered from the sample should be low relative to the sensitivity to gamma-rays produced from capture reactions in the sample; the signals should be fast to minimise dead-time and provide good time resolution; and finally comprise as little material as possible to reduce neutron scattering.

For this work, the detection system used was a quartet of organic liquid scintillation C_6D_6 (deuterated benzene) detectors developed at Legnaro National Laboratory (LNL) [59], shown in Figure 3.7. These are the latest iteration of C_6D_6 detectors developed for use at n_TOF. Previous versions include the commercially available BICRON detectors [60], and the FZK detectors developed at Forschungszentrum Karlsruhe [60]. The detectors consist of a 1 litre active scintillator volume, and 2 inch photomultiplier tubes (PMTs) separated by a lightweight quartz window to minimise neutron sensitivity. The signals from the PMTs are digitised directly, without need for amplification — this aids the time resolution. Deuterated benzene is used instead of hydrogenated benzene since the neutron capture cross section of ^{1}H is large leading

to a source of 2.2 MeV γ-rays from the $^1H(n, \gamma)$ reaction which would violate the requirement of low neutron sensitivity. The detectors are placed in the backwards hemisphere at 125° with respect to the neutron beam direction, both to minimise background events from in-beam photons preferentially Compton scattered into the forwards hemisphere, and also to minimise sensitivity to the angular momentum transfer ℓ in the neutron capture reaction. The resonances measured in this work are limited to s- and p-waves; the angular effect is minimised by placing the detectors at an angle of 125° (or 55°) with respect to the neutron beam[3].
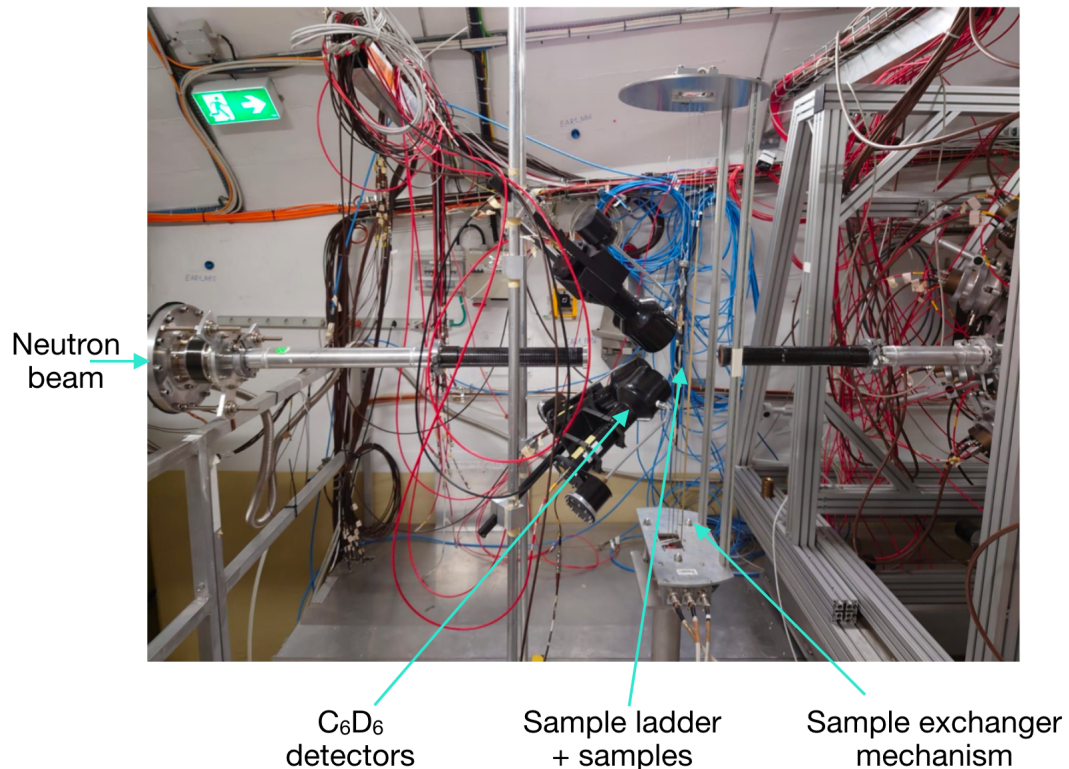
FIGURE 3.7: The low neutron scattering Legnaro-C_6D_6 total energy detection setup in Experimental Area I at n_TOF with ancillary equipment. The TAC is downstream.

The materials in the set-up are optimised for low neutron sensitivity; the detector housings and support structures closest to the neutron beam are carbon fibre, with some structural components manufactured from aluminium. The relative neutron and gamma-ray *sensitivity* $\epsilon_n/\epsilon_\gamma \approx 10^{-5}$; the sensitivity takes not only the detection efficiency into account, but also the effect of the surrounding materials — see [60, 61] for details of the simulations used to determine this number. A further requirement of the detection system is that it recovers promptly from the γ-flash discussed earlier. An example of the response of a single C_6D_6 detector to the flash is shown in Figure 3.8, where the baseline recovers after ≈ 2 μs meaning that in principle at EAR1,

---

[3]For dipolar transitions, the angular distribution of gamma-rays relative to the beam direction is $P_2(\cos \theta)$ (second order Legendre polynomial) which is zero at $\theta = 125°$.

measurements can be made up to neutron energies of around 20 MeV with the nominal pulse intensity. This limit can be extended if and when required by reducing the beam intensity. In practice though, the competing inelastic scattering channel dominates the count rate at neutron energies around 200-300 keV limiting the range of the cross section measurement to neutron energies below this threshold.
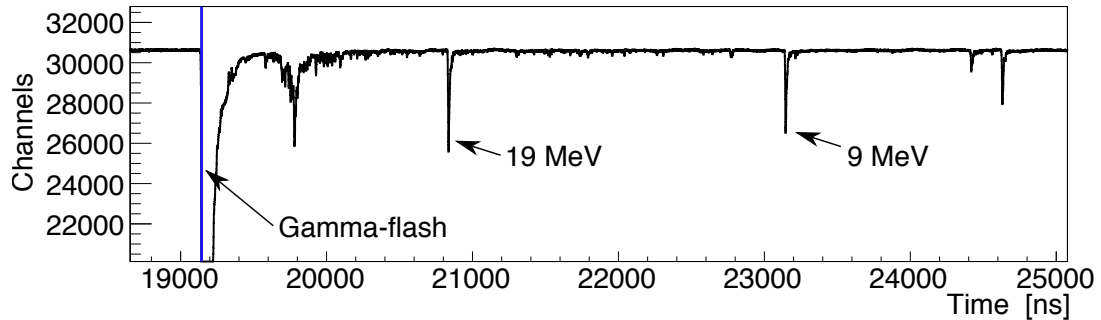
FIGURE 3.8: A typical Legnaro-C_6D_6 response to the γ-flash at EAR1 for a dedicated pulse. The time is measured with respect to the PS trigger. The flash extends from the vertical blue line, indicative of the time deduced by the pulse shape analysis routine, to around 20.5 μs. Typical signals and their corresponding neutron energies are shown.

The alternative detection apparatus at n_TOF suitable for capture measurements is the TAC (Total Absorption Calorimeter) situated in EAR1; the principle of total absorption calorimetry was discussed in Section 2.3. There are practical limitations which for this measurement mean that the C_6D_6 set-up was more appropriate: for light nuclei such as ^{35}Cl, the scattering to capture cross section ratio is typically higher, and the very low neutron sensitivity of the C_6D_6 set-up is superior to that of the TAC, composed of 40 BaF_2 crystals and dense structural materials. Furthermore the TAC has an upper neutron energy limit of around 40 keV due to its slow recovery from the gamma-flash. In this work, the resolved resonances extended beyond this limit. Further information on the TAC can be found in Reference [17].

3.2.4 Ancillary detectors

A number of ancillary detectors are used to monitor the proton and neutron beams on a bunch-by-bunch basis:

- The beam current transformer (or *BCT*) is located 6 m upstream of the spallation target and gives the absolute number of protons delivered by the PS. This value can therefore be used to monitor the relative neutron pulse intensity.

- Directly before the lead spallation target, a wall current monitor measures the instantaneous current induced by the proton bunch in a section of the

beam-line wall, and is referred to as the pick-up (or *PKUP*). It provides a precise measurement of the proton current to within 1%, so can also be used to monitor the neutron pulse intensity. This signal is also used to trigger the n_TOF data acquisition.

- The *SiMon* (silicon monitor) system, also used as part of the flux characterisation, consists of four silicon detectors placed in the periphery of the neutron beam into which is placed a thin Mylar foil loaded with a thin deposit of ^{6}Li (200 $\mu g/cm^2$) [57]. The triton and alpha particles generated from ^{6}Li$(n, t)\alpha$ reactions are detected by the silicon detectors.

The proportionality between the different detectors is monitored on a run-by-run basis, important to be sure of the final neutron fluence integrated over the whole experiment for the measurements associated with each of the samples. Moreover, the counting rates of the C_6D_6 detectors are monitored on a run-by-run basis relative to the neutron monitors as a means of detecting systematic changes in performance.

3.2.5 Data acquisition and pulse shape analysis

Data acquisition

Owing to the variety of detectors used at n_TOF, the philosophy taken with data acquisition is to digitise and store all signals for off-line processing, bypassing the need for detector specific electronic hardware. This approach also affords one the convenience of being able to implement and tweak sophisticated pulse shape analysis routines as many times as is desired after the experiment. The digital acquisition system (DAQ) is based around 12- or 14-bit flash-ADCs which digitise at a rate of 1 GHz for periods of up to 100 ms — for EAR1, when the DAQ is triggered by the *PKUP* signal mentioned in the previous section, this time limit corresponds to a lower neutron energy limit of 18 meV. This sampling rate is necessary to deal with the fast signals associated with most detectors at n_TOF, required for good neutron energy resolution; for example the total width of the C_6D_6 signals used in this work is ≈ 15 ns. Digitising at such a rate demands a very fast data storage system. The data throughput is reduced by applying a fast 'zero-suppression' algorithm within the DAQ which sends data for storage when the signal crosses a specified threshold, and for a set period before and after the threshold crossing. The data are stored in a local disc pool along with the run number, timestamp and data corresponding to the neutron monitoring detectors, before being transferred to CASTOR (the CERN

Advanced Storage manager) [62]. The data is eventually migrated to tape for long term storage.

Pulse shape analysis (PSA)

The non zero-suppressed raw digitised signals are analysed with a suite of pulse shape analysis routines developed within the n_TOF collaboration, specific to each detector type [63]. A basic example of the procedure is shown in Figure 3.9. True signals are firstly recognised from noise according to the behaviour of the numerical derivative, which for a negative polarity uni-polar signal such as the one shown in the top pane of Figure 3.9 will cross a negative threshold twice, before crossing a positive threshold twice, as shown in the middle pane of Figure 3.9 — setting the derivative thresholds at around 4-5× the r.m.s. of the signal derivative serves to effectively recognise signals which are to be further processed from noise. An adaptive baseline routine is used to locally subtract a shifting baseline: around the gamma-flash, the local baseline is taken as a 'moving maximum', but for later times-of-flight the baseline is flat and for a given proton pulse is simply averaged over portions of baseline surrounding the non zero-suppressed signals. The baseline subtracted signal is fitted with an average pulse shape in order to derive an accurate signal amplitude, area and time via a constant fraction discrimination (CFD) with a fraction of 30%. With this method, the time is obtained to an accuracy of less than 1 ns, and the measurement of the amplitude and area of signals is made more accurate, especially for smaller signals. The approach of fitting the baseline subtracted signal also handles cases with pile-up in which the tail of any fitted signal serves as the baseline for possible secondary signals. A second threshold on the signal amplitude is chosen to remove any spurious false signals. A similar procedure is applied to the *PKUP* and *SiMon* signals; for these detectors however, average signal shapes are not fitted — the area is given by the numerical integral after baseline subtraction, and the amplitudes are derived from a parabolic fit to the maximum/minimum of the signal before a CFD is once again used to obtain the signal time. For each proton pulse, the gamma-flash is distinguished as the first signal to saturate the digitisers, and the time of the gamma-flash taken as the time at which the signal crosses a specified threshold. Individual signals are packaged together and labelled by proton bunch number and experimental run number such that where necessary signals from different detectors can be correlated in the analysis.
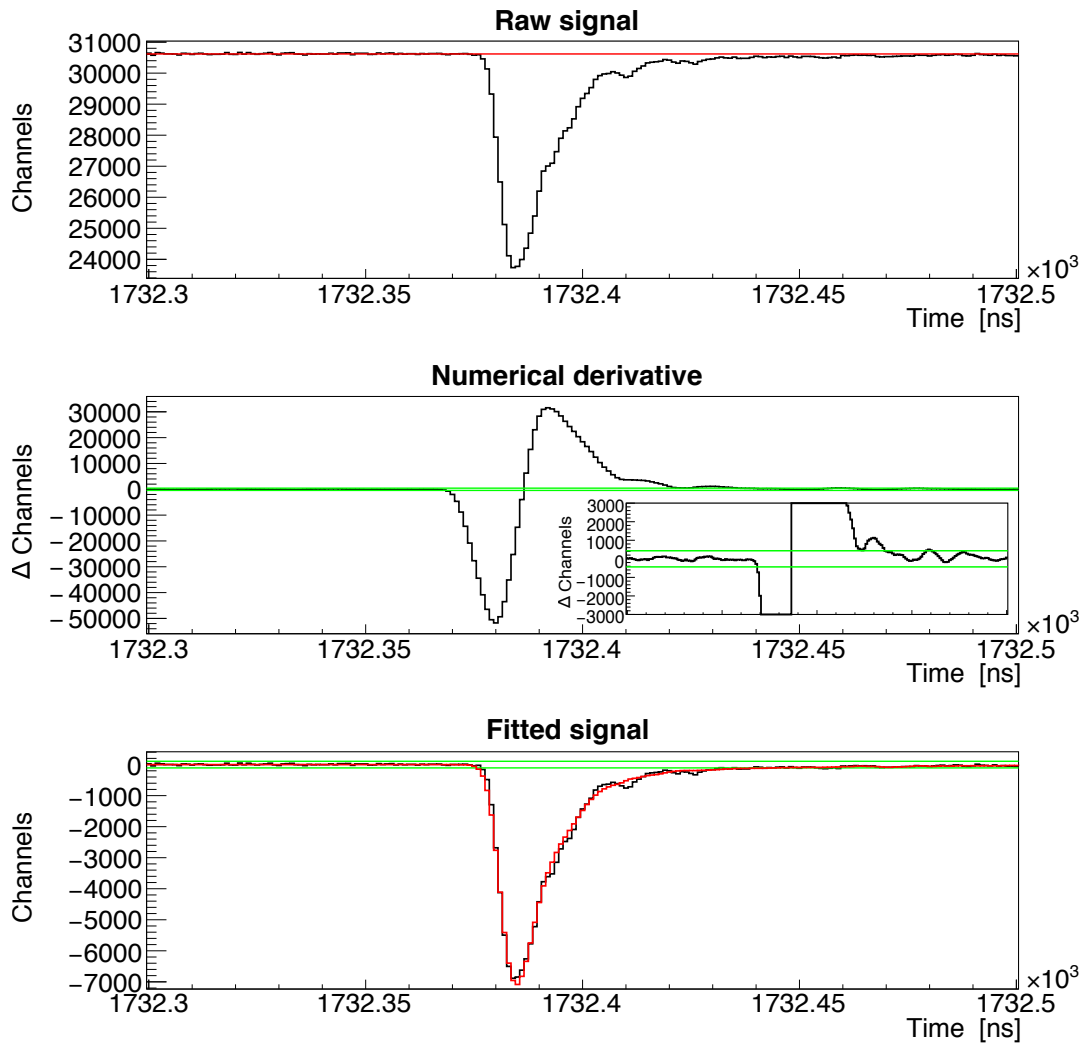
FIGURE 3.9: Example of the pulse shape analysis for a single raw C_6D_6 signal (top) consisting of signal identification via the numerical derivative of the raw signal (middle), and a fit to the baseline subtracted signal with the average signal shape for that particular detector, shown in red (bottom). The horizontal green lines indicate thresholds, discussed in the text.

3.3   Measurement and sample details

For this measurement, performed in June 2018, the total allotted number of protons delivered to the n_TOF spallation target from the CERN PS was 1.8×10^{18} [33], where the total number of protons delivered to n_TOF per year is around 1.5×10^{19}. The proton budget for this measurement was spread over several samples, shown in Table 3.2. The largest fraction was used for measuring the sample of interest. This was a circular sample pressed from enriched NaCl salt, containing 99.635% $^{23}Na^{35}Cl$ by mass (the isotopic abundance of natural Cl is 75.77% ^{35}Cl and 24.23% ^{37}Cl). During the production of the pressed pellet however, there was an issue with contamination from the press which introduced foreign matter into the salt powder. For this reason an ICPMS analysis (inductively coupled plasma-mass-spectrometry) was performed on the sample after the experiment and it was confirmed that the impurities were in fact negligible[4]. For the experiment, the pressed pellet was sandwiched and glued between two 6 μm mylar backings and mounted onto an aluminium ring used to hold the assembly to the sample ladder and exchanger described below — the sample is shown in Figure 3.10.

TABLE 3.2: Details of the measured samples, and proton allocation.

Measurement/ sample	Sample Composition	Mass (mg)	Thickness (atoms/barn)	Protons	Bunches
NaCl [a]	99.635% $^{23}Na^{35}Cl$	959.7	3.174×10^{-3} [b]	9.92×10^{17}	188710
Au	100% ^{197}Au	747.5	7.275×10^{-4}	1.71×10^{17}	30569
C	Natural C	2646.1	4.243×10^{-2}	1.15×10^{17}	21494
Empty [c]	—	—	—	1.42×10^{17}	29518
NaCl/empty + filters	—	—	—	2.54×10^{17}	93185
Beam-off	—	—	—	—	161463

[a] Sample in the form of a pressed salt powder.
[b] Areal density of ^{35}Cl.
[c] Identical sample holder and backing material as for the NaCl sample.

The remaining protons were used for measuring a gold sample for normalisation, and a carbon sample and empty sample holder for the purpose of studying the various

---

[4]The known impurity introduced to the sample during its preparation was aluminium. This was found to be present at the level of ∼ 1 part in 1000 — this level of contamination is negligible, as this does not affect the resonances specific to ^{35}Cl and has a negligible effect on the calculation of the thickness (atoms / unit area) important for the final normalisation of the data. No other contaminants of significance were found.

background components and systematics, as well as measurements with in-beam filters, also for background quantification. The empty sample holder was identical to the NaCl target assembly minus the NaCl pellet. In addition to runs taken with protons on target, several 'beam-off' measurements were performed, also for background quantification, and calibration runs were taken using standard mono-energetic sources for calibrating the detectors; calibrations were performed at the beginning, middle and end of the experiment to monitor the stability of the gain with time.
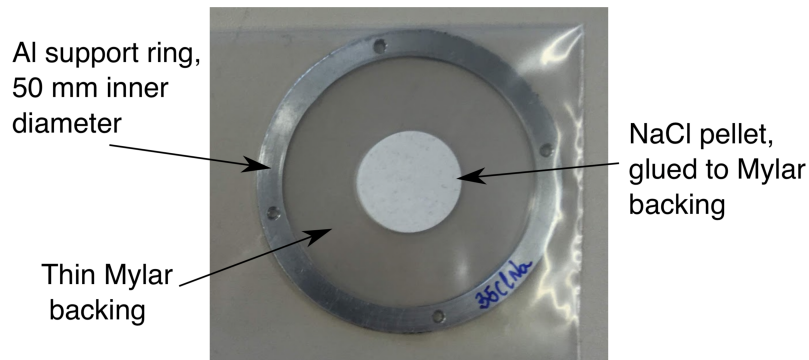
FIGURE 3.10: Enriched $^{23}Na^{35}Cl$ sample, backing and support.

As was already discussed, if using a reference sample to normalise the data taken with a sample of interest, aligning the two samples is crucial since the beam interception factor can vary significantly from just a modest misalignment. The solution at n_TOF is to use a fixed carbon fibre sample ladder, shown in Figures 3.7 and 3.12, which is computer controlled and contains up to five samples — it is only movable in the vertical direction in discrete intervals. A laser cross-hair is projected onto the sample in the measuring position to ensure alignment with the nominal measuring position at the centre of the neutron beam to within around 0.5 mm.

3.4   Outline of the data reduction and analysis steps

The remainder of this chapter deals with the data reduction, analysis, implications and comparison of the n_TOF results with previous measurements. The individual analysis steps are:

- Data quality checks: checking the detector behaviours, and monitoring any systematic changes over the course of the experiment. Checking the proportionality between primary proton beam and neutron beam intensities, and the proportionality between neutron beam intensity and C_6D_6 counting rates for each sample.

- Energy calibration of the C_6D_6 detectors via comparison to Monte-Carlo simulations.

- Evaluating the effect of dead-time, coincidences between detectors where multiple gamma-rays from a single capture cascade are detected in different detectors, and multiple hits where multiple gamma-rays from a single capture cascade are detected in the same detector.

- Time-to-energy calibration of the time-of-flight spectrometer.

- Background evaluation and subtraction using a combination of ancillary measurements and Monte-Carlo simulations.

- Application of the total energy detection method already discussed in Section 3.2.3 through the pulse-height weighting technique, and the calculation of several corrections that must be made when applying the PHWT that relate to the imposition of an electronic threshold for each detector, internal conversion and multiple hits, all of which lead to effects that change the measured total energy with respect to the 'real' total energy.

- Normalisation of the data using the saturated resonance method, which takes the absolute normalisation of the neutron flux at n_TOF into account as well as the absolute efficiency of the detection system.

- Cross section analysis to obtain the resonance parameters and thermal cross section and a comparison to previous measurements and evaluations, followed by an assessment of the impact of the measurement on the applications of interest. As will be shown, the cross section in the URR was not measurable in this experiment.

Where possible and appropriate, the four C_6D_6 detectors were treated separately, as were the parasitic and dedicated beam modes. This allowed the consistency of the various corrections and background subtractions to be validated, before the corrected count rates were combined for the final cross section analysis.

3.5 Detector performance, calibration and data quality checks

3.5.1 Signals and stability

During this experiment, and other experiments performed in 2018 with the same set-up, it was observed that very often C_6D_6 detector signals were followed by smaller false 'after-pulses' occurring at discrete times after the main signal. Investigations in 2018 pointed to an impedance mismatch between the coaxial cable and the digitisers of the data acquisition system causing multiple reflections. In a region of constant count rate the waiting time between two successive signals is expected to follow an exponential distribution — as shown in Figure 3.11, for the case where the second signal is small, this expected behaviour is not observed since there are a number of discrete structures. If such false signals are not dealt with, the discrete time structure leads to shoulders on the measured resonance shapes. This problem is solved by the imposition of a reasonable threshold on the deposited energy for all signals in the analysis, chosen to be 250 keV for all detectors — the threshold is indicated in Figure 3.11. A threshold of around 100-200 keV is in fact normal for this detection system as discussed in Section 3.7, and so the 250 keV threshold in this measurement only has a modest effect on the analysis, reducing the statistics by a small amount. With this threshold, the expected exponential waiting time distribution between successive signals is restored, as shown in Figure 3.18 as part of the dead-time analysis.
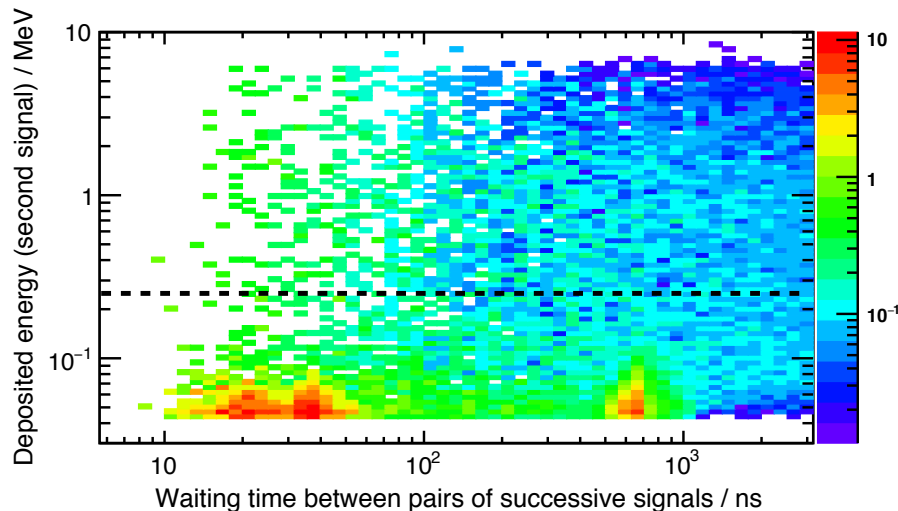
FIGURE 3.11: Distribution of the waiting time between pairs of consecutive signals for a single detector in a region of constant count rate, and deposited energy of the second signal (the same behaviour was seen for all four detectors). The after-pulses discussed in the text are visible at around 20, 40 and 700 ns, and the horizontal dashed line indicates the threshold of 250 keV chosen to eliminate them from the analysis. The decline of counts around 20 ns is due to the dead-time of the system (discussed in Section 3.5.4).

It is important to monitor the stability of each of the the detection systems used, not only the gamma-ray detectors, but also those used for measuring the neutron beam intensity crucial for normalisation of the data. Data quality checks to monitor the stability of the four detection systems (BCT, PKUP, SiMon and C_6D_6) consisted of tracking the proportionality between: the proton pulse intensity from the PS BCT, proton pulse intensity as determined using the PKUP, neutron beam intensity as determined using the SiMon detectors, and the integrated counts of the C_6D_6 detectors. These checks were performed on a run-by-run basis (each run lasting around 4 hours), using NaCl sample measurement runs; in this case the same proportionality should be measured over the whole experiment, lasting for 17 days. The proton pulse intensity determined from the PKUP on a bunch-by-bunch basis is taken to be the area of the signal, and the neutron beam intensity at the experimental area with the SiMon silicon detectors is taken to be the number of triton signals from the $^6Li(n,t)$ reaction which are well separated from noise (see Section 3.8.1 for more details on SiMon data analysis). The number of C_6D_6 signals was taken to be all those signals with deposited energy >250 keV. There were no outlying runs, indicating that all detectors performed satisfactorily during the whole experiment, and the variation in the proportionality between the four detection systems, quantified as the ratio of the width and mean of the distributions of the relative quantities discussed above (σ/μ), is shown in Table 3.3. The final normalisation of the total neutron fluence was performed using the BCT value.

TABLE 3.3: Variation in the proportionality between proton and neutron pulse intensities using the BCT, PKUP and SiMon detectors, and C_6D_6 detector counting rates. The variation coefficient (σ/μ) is discussed in the text.

Ratio	Variation (= σ/μ of distribution over all runs) / %
Pulse Intensity (BCT) / PKUP	0.06
SiMon / PKUP	SiMon detectors 1-4: 1.4, 1.6, 1.6, 1.6
C6D6 / PKUP	C_6D_6 detectors 1-4: 1.7, 1.8, 1.9, 1.7
C6D6 / total SiMon	C_6D_6 detectors 1-4: 1.9, 2.0, 2.2, 1.9

The stability of the gain of the C_6D_6 detectors was monitored by taking calibration runs at the start, middle and and of the experiment from which it was found that the gains for three detectors varied by < 1% over the whole energy range, but by $\approx$ 4% for the remaining one for large deposited energy (with the CmC source). It was found however that this shift was not important when propagated through to the final reaction yield for that particular detector which was consistent with the other three detectors.

3.5.2 C_6D_6 energy calibration

An accurate energy calibration of the detectors is crucial for the total energy detection analysis, implemented through the pulse height weighting technique used for the production of the reaction yield, where a weight is applied to each event based on the deposited energy — this is discussed at length in Section 3.6.1. For the liquid C_6D_6 detectors used in this work, the photo-peak efficiency is poor due to the low atomic number and low density of the scintillation material; the gamma-ray response is therefore dominated by the Compton scattering continuum, and multiple Compton scattering events as shown in Figure 3.13. To accurately calibrate the detectors therefore, Monte-Carlo simulations have been performed to obtain the responses to several mono-energetic gamma-ray sources, which were subsequently matched to their experimental counterparts via a least squares fitting procedure. In this work, the signal areas were used rather than signal amplitudes as this was the most accurate measure of the deposited energy from the signal pulse shape analysis in Section 3.2.5, taking the integral of the scintillation light output rather than the peak value. The gamma-ray sources used for calibration were ^{137}Cs (662 keV), ^{88}Y (coincident 898 keV and 1.836 MeV), $^{241}Am^9Be$ (4.44 MeV from $^9Be(\alpha, n)^{12}C$), and $^{244}Cm^{13}C$ (6.13 MeV from $^{13}C(\alpha, n)^{16}O$). An accurate calibration is required up to the neutron separation energy (as excitation energies for neutron capture $\sim S_n$), 8.58 MeV for ^{35}Cl; the extrapolation from the last calibration data point at 6.13 MeV was however sufficient, as will be shown in subsequent sections.

An accurate representation of the detection apparatus and surrounding materials based on those of Reference [64] was implemented in a Geant4 [65] simulation and is shown in Figure 3.12, with special attention paid to the detectors consisting of the active detection volume, quartz window, photomultipler tube components and carbon fibre container. Only the photon and electron transport in the sample and detectors were considered in the radiation transport, and the scintillation light production and propagation were not explicitly taken into account. The final detector responses were obtained by convolving the simulated responses with the instrumental broadening, governed by scintillation light collection and photoelectron production and transport in the photomultiplier tube; since there is no photopeak, this Gaussian broadening was determined from the experimental data before convolving with the simulated Geant4 deposited energy responses for direct comparison with the measured spectra. It should also be noted that aside from an accurate calibration, accurate broadened responses are required over the full range of emitted gamma-ray energies (not just those given by the calibration sources) as part of the pulse height weighting technique,
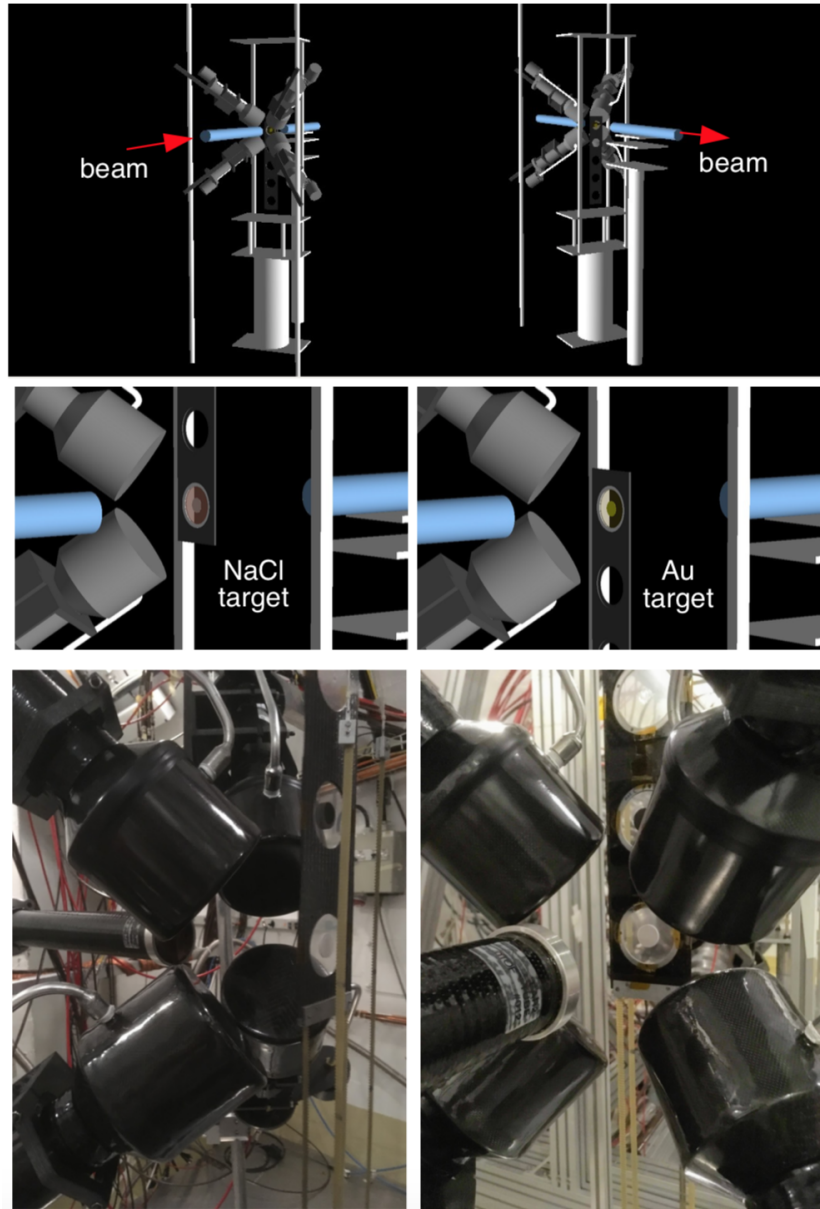
FIGURE 3.12: The Geant4 geometry showing the C_6D_6 setup in EAR1, with corresponding photographs. The four detectors are shown with their faces at 125° with respect to the neutron beam and 10 cm from the target position, alongside the carbon fibre sample ladder, samples plus backings (NaCl sample shown in measuring position in the photographs), carbon fibre beam lines plus kapton vacuum windows, and aluminium/carbon fibre support structures.

so applying the most accurate representation of the experimental broadening to the simulations is vital — this is made clear in Section 3.6.2.

The broadening can be obtained by imposing a functional form for the resolution and varying the parameters until the broadened simulations match the calibration spectra, the usual approach taken. In this work however, the instrumental broadening as a function of deposited energy $\sigma(E)$ was determined experimentally using a

method based on that of Reference [66], using the experimental calibration spectra. It is based around the idea that the non-broadened deposited energy spectrum $r(E)$ contains a discontinuity at the energy of the Compton edge. Therefore $\mathrm{d}r/\mathrm{d}E$ contains a δ-function-like shape, which when one convolves with the experimental broadening gives a result approximating a Gaussian centred at the Compton edge energy: $G(E - E_C)$. The width of this Gaussian $\sigma(E_C)$ gives the resolution at the Compton edge energy. The measured spectrum $r \star G$ (convolution of r and G) can be numerically differentiated to give $G(E - E_C)$, since

$$\frac{\mathrm{d}}{\mathrm{d}E}(r \star G) \approx \delta(E - E_C) \star G(E) = G(E - E_C), \tag{3.6}$$

from which the resolution $\sigma(E_C)$ can be found[5]. An example of this procedure is shown in Figure 3.13. The experimental resolution was measured with each of the calibration sources and is shown as a function of deposited energy E_d in Figure 3.14, with a fit of the form $\sigma(E_d) = a + bE_d + cE_d^2$. The final calibration was made by scaling the simulated spectra until a range of points on the Compton edge matched the experimental ones as shown in Figure 3.15 thus providing an accurate signal area A to deposited energy E_d calibration, which when repeated for each of the calibration sources was parametrised as $E_d = a\sqrt{A} + bA$.

---

[5]This relation follows since for the convolution of two functions $r(E) \star G(E)$,

$$\frac{\mathrm{d}}{\mathrm{d}E}(r \star G) = \frac{\mathrm{d}r}{\mathrm{d}E} \star G. \tag{3.7}$$
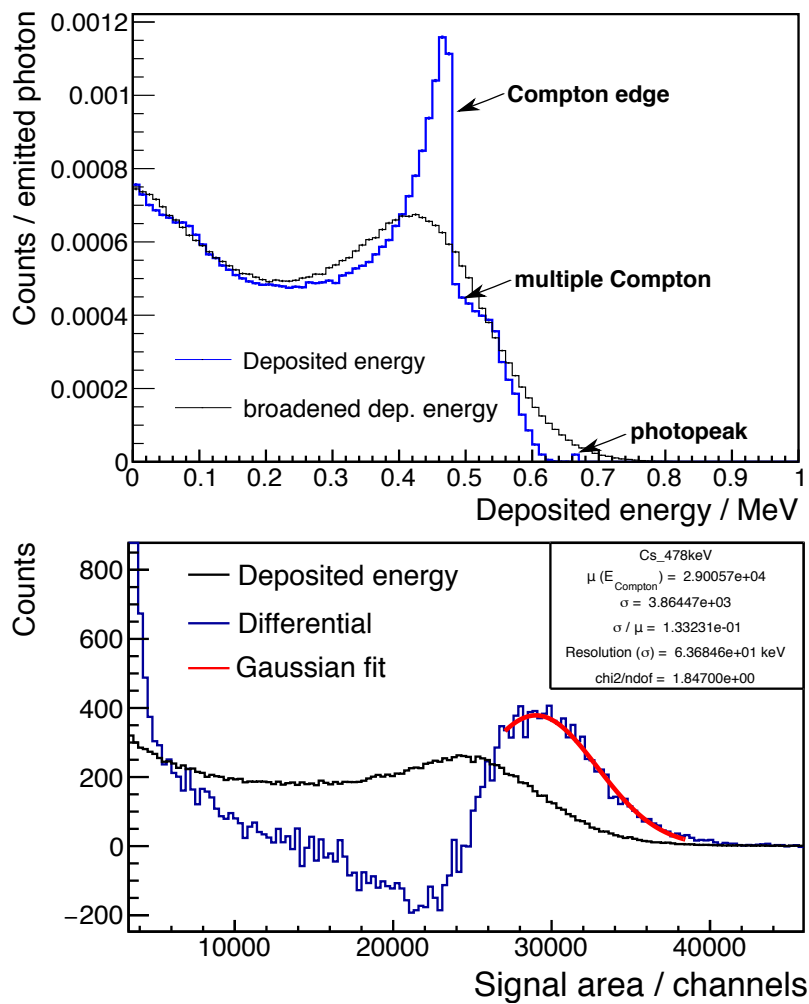
FIGURE 3.13: (Top) Example C_6D_6 detector response (blue) obtained from a Geant4 simulation for the case of 662 keV gamma-rays from the ^{137}Cs source. The broadened version of the simulation (black) is also shown. (Bottom) ^{137}Cs experimental spectrum and its numerical derivative with a Gaussian fit to the Compton edge in order to measure the deposited energy resolution, see text. The quantities μ and σ in the inset refer to the mean and width of the Gaussian fit, respectively.
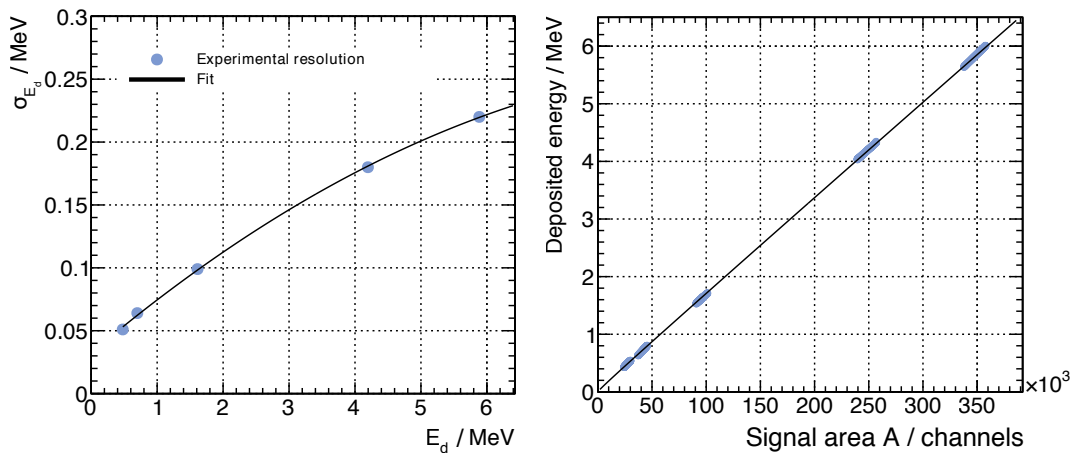
FIGURE 3.14: (Left) Resolution for a single C_6D_6 detector, measured using the method described in the text. (Right) Signal area to deposited energy calibration obtained by matching the experimental responses to the simulated ones, see text. The functional forms for both fits are given in the text.
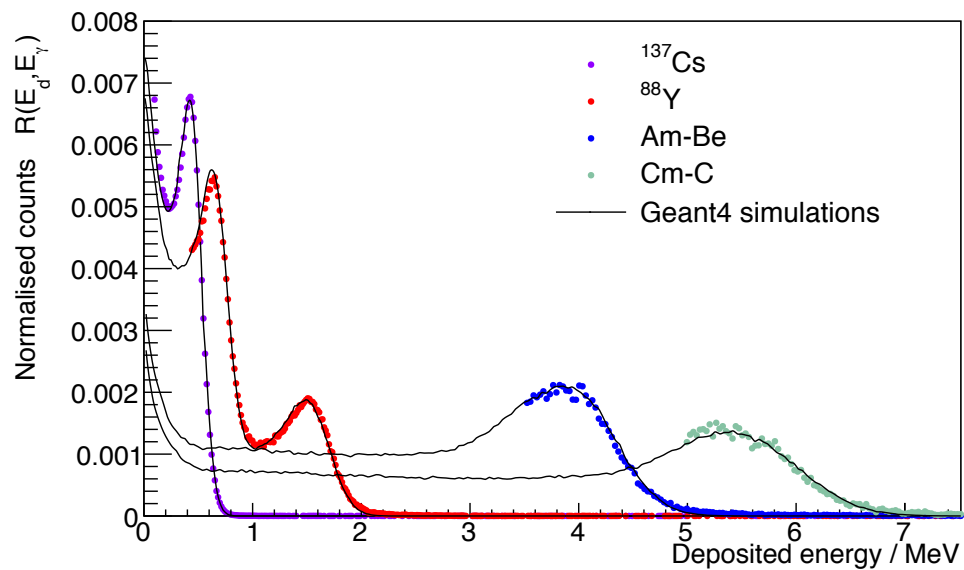
FIGURE 3.15: Comparison of the experimental responses for each of the calibration sources with the simulated ones (for AmBe and CmC, the spectra have been scaled ×4, and the experimental spectrum is only shown for the Compton edge due to additional gamma-ray lines in the source spectrum not included in the simulation).

3.5.3   Neutron time-of-flight to energy calibration

Since different detectors and experimental set-ups have different electronics and are placed in slightly different positions, a separate time-to-energy calibration must be performed for each experiment at n_TOF. As discussed in Section 3.2.2, the resolution function acts to modify the time-to-energy relation in Equation 2.6, the solution to which is the addition of a constant time offset t_{off} to the measured time-of-flight. Following from Equations 2.6 and 3.1, the modified time-to-energy relation is therefore given by

$$E_n = m_n c^2 \left(\frac{1}{\sqrt{1 - \left(\frac{L}{(t - t_\gamma + L/c + t_{off})c} \right)^2}} - 1 \right). \tag{3.8}$$

The geometrical flight path length L and the time offset t_{off}, which accounts for the moderation time within the neutron producing target assembly, are calibrated by measuring a ^{197}Au sample at the same position as the NaCl target (the same measurements used for the normalising the ^{35}Cl cross section with the saturated resonance method); ^{197}Au is considered a cross section *standard*, the resonance energies are therefore well known [26]. An iterative method is used to obtain consistent values for L and t_{off}: the arbitrarily normalised ^{197}Au time-of-flight spectrum is firstly converted to neutron energy with an initial guess for the value of L, with $t_{off} = 0$. The resonance fitting software SAMMY (described in Section 3.9.1) is then used to fit several resonances, leaving the resonance energies E_R as free parameters, but keeping the widths Γ_n and Γ_γ fixed, taking their values from the ENDF-BVIII.0 data library. SAMMY takes into account the various factors that act to change the shape and measured position of resonances discussed in Section 3.2.2, including the resolution function. The resonance energies E_R are then converted back to time-of-flight using the initial guess for L with $t_{off} = 0$, which are shown in Figure 3.16 plotted against the known resonance energies from ENDF-BVIII.0. These data are then fit using the relation of Equation 3.8, giving a geometrical flight path of $L = 183.838(6)$ m and time offset of $t_{off} = 98.4(80)$ ns[6]. Using these parameters and following the analysis procedures detailed in this chapter for the production of the reaction yield for the NaCl sample, a comparison of the measured and theoretical ^{197}Au yields is shown in Figure 3.17 where it can be seen that the time-to-energy calibration is satisfactory, consistently reproducing the positions of resonances to well within 1 eV (for the energy range shown).

---

[6]The quoted uncertainties are not accurate representations of the uncertainties on the 'real' physical quantities t_{off} and L, which in this context are merely parameters in the time-to-energy relation.
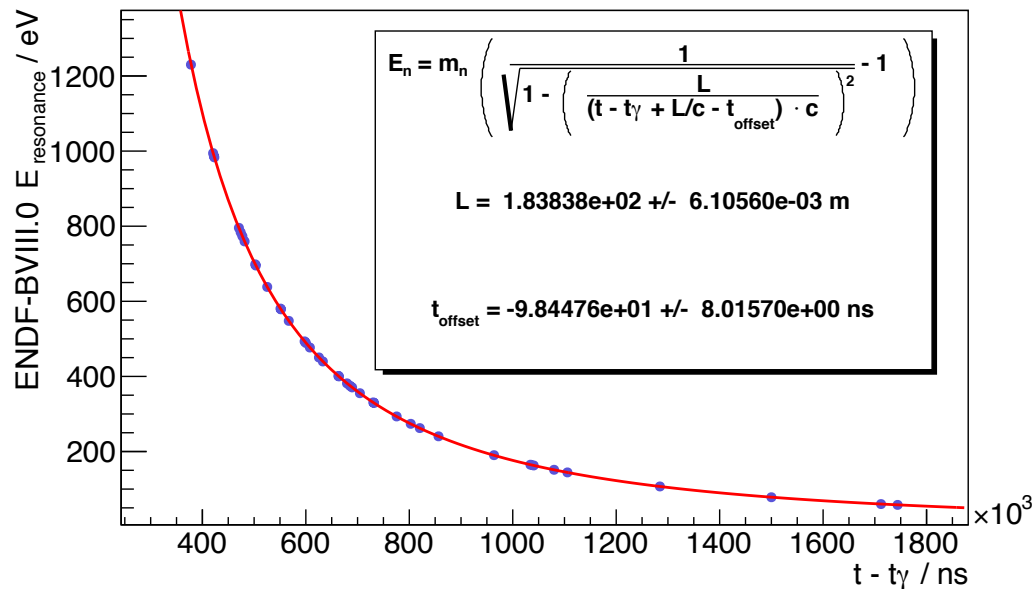
FIGURE 3.16: Determination of the time-to-energy parameters discussed in the text via a fit of the experimental times-of-flight for several ^{197}Au resonances to the known resonance energies from the ENDF-BVIII.0 library with the time-to-energy dispersion relation in Equation 3.8.
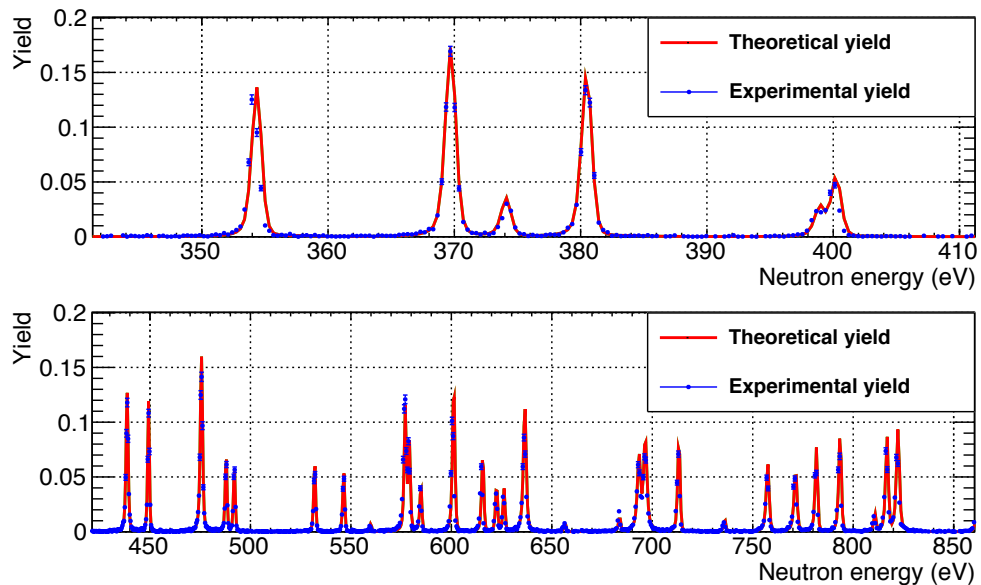
FIGURE 3.17: Examples of the theoretical and experimentally measured ^{197}Au(n, γ) reaction yield using the determined time to energy calibration parameters. The theoretical yield was calculated using SAMMY with resonance parameters from the ENDF-BVIII.0 library.

3.5.4 Dead-time, coincidence and multiple hit corrections

Despite the low efficiency of the C_6D_6 detectors used in this work, it is important to apply a correction for the dead-time inherent to the system to avoid the underestimation of the final reaction yield, especially pronounced for strong resonances. The dead-time is associated with the detector, electronics, digitisers, data acquisition system and the subsequent pulse shape analysis routines discussed previously. The correction is made by choosing a well defined fixed dead-time (as close as possible to the real dead-time) and applying this to the data by imposing a veto on the time between consecutive signals for each individual detector. As shown in Reference [67], for the case of both paralysable and non-paralysable systems, when the dead-time is small the corrected counting rate $C_{corr}(E_n)$ is given by

$$C_{corr}(E_n) = \frac{C(E_n)}{1 - C(E_n)\tau} = f_{dt}(E_n)C(E_n), \tag{3.9}$$

where $C(E_n)$ is the measured count rate and τ is the fixed dead-time — f_{dt} is the correction factor. The dead-time is evaluated by examining the distribution of the waiting time between consecutive signals for each detector, where around the dead-time of the system there is a sharp decline as shown in Figure 3.18; for this work a dead-time of $\tau = 20$ ns was chosen for all four detectors. The two distinct beam intensities (parasitic and dedicated beam modes) mean that in the analysis, data corresponding to the two modes were corrected separately since the count rates for the two modes are also different — this also allowed the consistency of the correction to be verified. The correction factors for the NaCl and Au samples for the largest intensity beam mode (dedicated) are shown in Figure 3.19, where the corrections f_{dt} are never greater than 1% for the neutron energy range of interest. The uncertainty associated with this correction is therefore assumed to be negligible.

To avoid double counting, which would otherwise cause an artificial increase of the capture yield, it is important that only one of any coincident signals in different detectors from gamma-rays originating from the same cascade is used in the analysis. The effect is shown in Figure 3.18 where the waiting time distribution between consecutive signals for different detectors increases below around 20 ns indicating the detection of gamma-rays from the same cascade; a 20 ns veto on the time between successive signals from any detector is sufficient to exclude these events. Similarly, this distribution can be used to estimate the multiple hit contribution (> 1 gamma-ray depositing energy in a single detector), since it is just as likely for two or more gamma-rays to interact with the same detector as it is for them to interact with

separate detectors. This correction is complicated by the application of the pulse-height weighting technique which artificially modifies the detector efficiency — the correction is discussed further in Section 3.6.2 where is it shown that it is on the order of 0.1%, and is thus negligible when compared to statistical errors and the systematic uncertainties associated with the neutron flux for example.
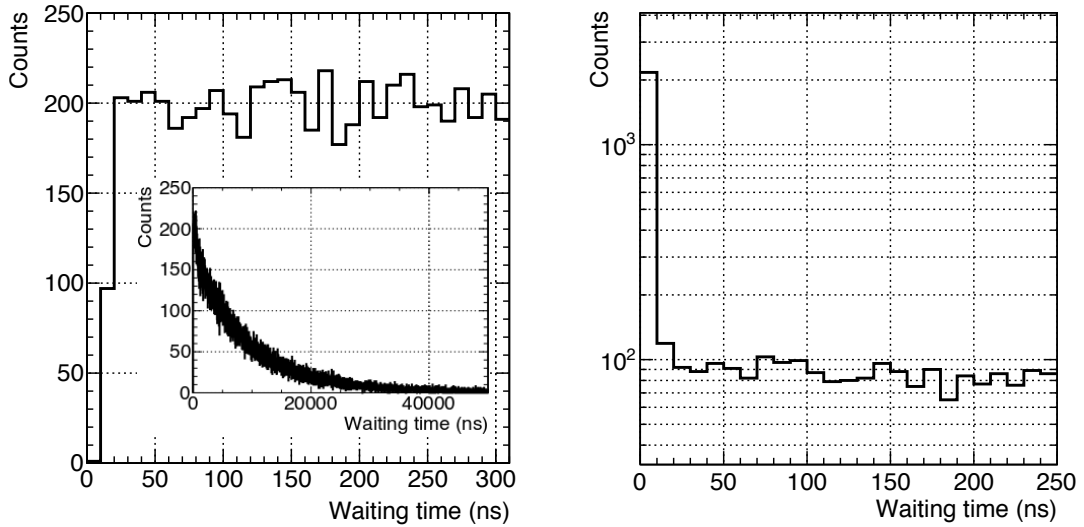
FIGURE 3.18: Waiting time distributions between pairs of consecutive signals for the same detector (left) and between different detectors (right), both shown for the plateau of the Au 4.9 eV saturated resonance where the count rate is constant, and only for signals with deposited energy > 250 keV (to avoid the 'afterpulses' discussed in Section 3.5).
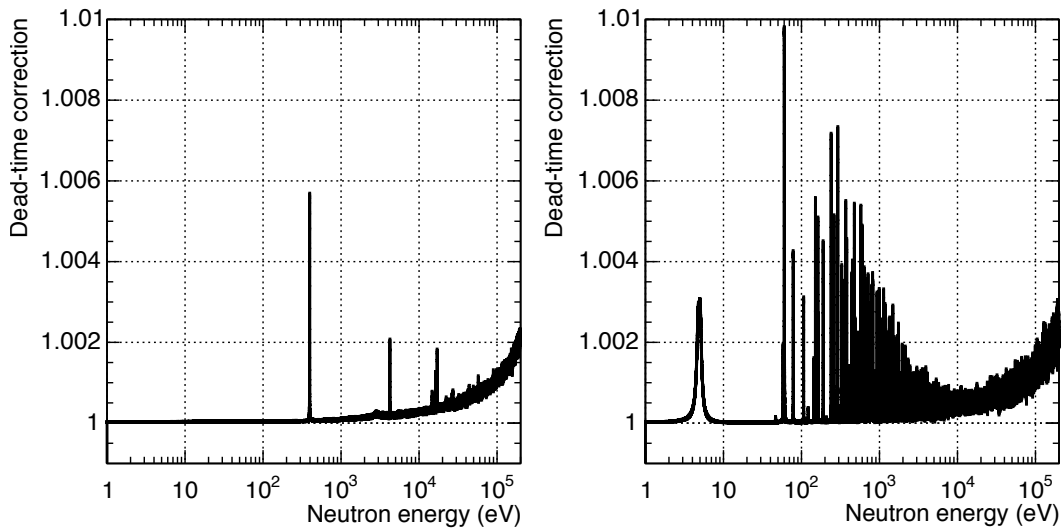
FIGURE 3.19: Dead-time correction factors, f_{dt} in Equation 3.9, for the NaCl (left) and Au (right) samples, both for the dedicated beam mode. Even for the strongest resonances, the correction is always < 1%.

3.6 Total Energy Detection analysis

This section deals with the Total Energy Detection (TED) analysis through the application of the Pulse Height Weighting Technique (PHWT), and the subsequent application of these methods to the experimental data.

3.6.1 Total Energy Detection and the Pulse Height Weighting Technique

The principles of the TED method were discussed in Section 3.2.3, where it was shown that in order to apply the method, the detectors of choice must have a low efficiency such that only one gamma-ray from a given cascade is measured, and have a gamma-ray detection efficiency that is proportional to the gamma-ray energy. As shown in Figure 3.20, although the gamma-ray detection efficiency of the C_6D_6 detectors used is small, it is not proportional to the gamma-ray energy. The PHWT is used to achieve this proportionality; the efficiency is mathematically manipulated in the analysis whereby counts are weighted according to the energy deposited in the detector on an event-by-event basis. If the probability that a gamma-ray of energy E_γ results in an event with an observed deposited energy E_d is $R_d(E_d, E_\gamma)$, the gamma-ray detection efficiency $\epsilon(E_\gamma)$ shown in Figure 3.20 is given by

$$\epsilon(E_\gamma) = \int_0^\infty R_d(E_d, E_\gamma) dE_d. \tag{3.10}$$
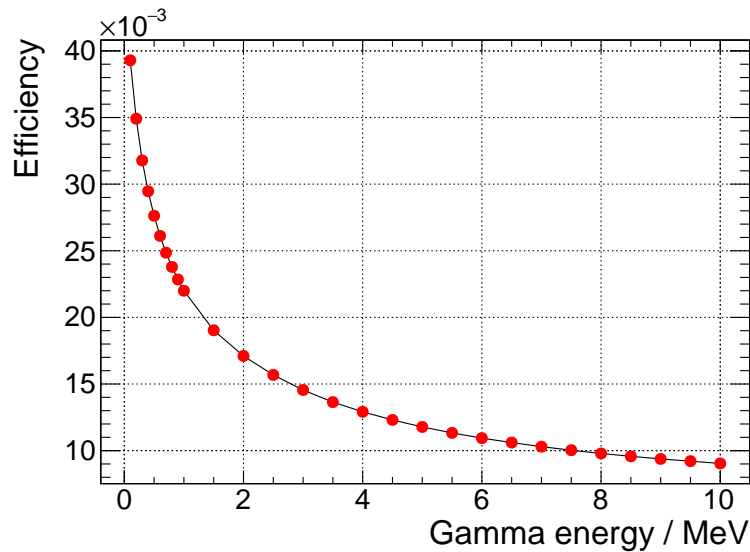
FIGURE 3.20: The simulated γ-ray detection efficiency given in Equation 3.10 for one of the Legnaro-C_6D_6 detectors in the array described in Section 3.2.3.

A *weighting function* $W(E_d)$ is defined such that

$$\int_0^\infty R_d(E_d, E_\gamma)W(E_d)\mathrm{d}E_d = E_\gamma, \tag{3.11}$$

and if such a function can be computed Equation 3.5 can be satisfied. Using this weighting function, the weighted time-of-flight spectrum $C_w(t_n)$ is calculated by transforming the experimental distribution of counts as a function of time-of-flight and deposited energy $C(t_n, E_d)$ in the following way:

$$C_w(t_n) = \int C(t_n, E_d)W(E_d)\mathrm{d}E_d. \tag{3.12}$$

By converting time-of-flight t_n to neutron energy E_n, one obtains an equivalent weighted neutron energy spectrum $C_w(E_n)$. The same operation is applied to the background, and since now by Equation 3.5 the capture cascade detection efficiency is given by the total cascade energy (equal to the excitation energy), the yield is given by

$$Y(E_n) \underset{\text{Eq. 2.5}}{=} \frac{C(E_n) - B(E_n)}{\epsilon\phi(E_n)} = \frac{C_w(E_n) - B_w(E_n)}{\left(S_n + \frac{A}{A+1}E_n\right)\phi(E_n)}, \tag{3.13}$$

where C is the total count rate and B is the background. Historically, the responses R_d in Equation 3.11 used for calculating the weighting function were determined by experimentally measuring the response to mono-energetic gamma sources and then interpolating and extrapolating to energies not measured. In modern, more accurate experiments, the calculation of the weighting function relies on accurate Monte-Carlo radiation transport simulations (using MCNP [68] or Geant4 [65]) of the response R_d involving the precise geometry of the detection setup and of the target from which gamma-rays originate. The simulations were detailed in Section 3.5.2, and the corresponding weighting function calculation is detailed in the next section.

There are several corrections that must be made when applying the PHWT that relate to the imposition of an electronic threshold for each detector, internal conversion and multiple hits, which all lead to effects that change the total energy that is measured with respect to the 'real' total energy. These corrections are discussed in detail in the next section and are labelled f_{PHWT}. In addition, a correction factor f_{Norm} must be applied in order to accurately normalise the yield that takes the absolute normalisation of the neutron flux at n_TOF into account as well as the absolute efficiency of the detection system. Taking these corrections into account, Equation 3.13 becomes

$$Y(E_n) = f_{Norm}f_{PHWT}\frac{C_w(E_n) - B_w(E_n)}{\left(S_n + \frac{A}{A+1}E_n\right)\phi(E_n)}. \tag{3.14}$$

3.6.2 Application of the Pulse Height Weighting Technique

Weighting function calculation

Separate weighting functions (WF), defined in Equation 3.11, were found for each detector and for both measured samples (NaCl and Au) because of the finite differences that different samples make to the responses R_d used to calculate the WF. The same Geant4 simulations described in Section 3.5.2 were used to generate the responses R_d in which gamma-rays were emitted isotropically into 4π from the samples; for the NaCl sample the origin of the gamma-rays was distributed uniformly throughout the sample volume since the product of areal density and total neutron cross section $n\sigma \ll 1$ and hence the self-shielding effect is negligible, but for the Au sample since it is the saturated resonance that is of interest for normalisation where the self-shielding effect is large, the origin of gamma-rays was exponentially distributed decreasing with increasing depth into the sample. By the same reasoning, in principle the WF depends on the strength of the resonance being measured and is hence also a function of neutron energy — this effect is small however when there are no saturated resonances, much smaller than the systematic uncertainties associated with the WF calculation and application. After discretising Equation 3.11, the WFs were found by minimising the expression

$$\chi^2 = \sum_j \left(E_{\gamma j} - \sum_{E_d > 0} R_d(E_d, E_{\gamma j}) W(E_d) \right)^2, \tag{3.15}$$

with the Minuit minimiser in the ROOT analysis package [69, 70]. The weighting function is expressed as a polynomial

$$W(E_d) = \sum_{i=0}^{i=4} a_i E_d^i, \tag{3.16}$$

and the sum j is over all of the simulated mono-energetic responses for gamma-ray energies $E_{\gamma j}$ for a given detector and sample material[7]. An example set of simulated responses is shown in Figure 3.21. The weighting function associated with these responses is shown in Figure 3.22, where the residuals given by $(\sum_i W(E_i)R(E_i, E_j))/E_j$ indicate that for this particular set of responses and WF, the relation of Equation 3.11 is satisfied for all deposited energies between 0.1 and 12 MeV to within 1.5%. This was also the case for the other detectors and for the case of the WF for the Au sample. The systematic uncertainty associated with the application of the WF according to Equation 3.12 is discussed further in the following section.

---

[7]For the cases where a polynomial WF is not appropriate, for example when very thick samples are used, it can be calculated numerically — see Reference [71]. Typically though, a polynomial of order 3, 4 or 5 is sufficient.
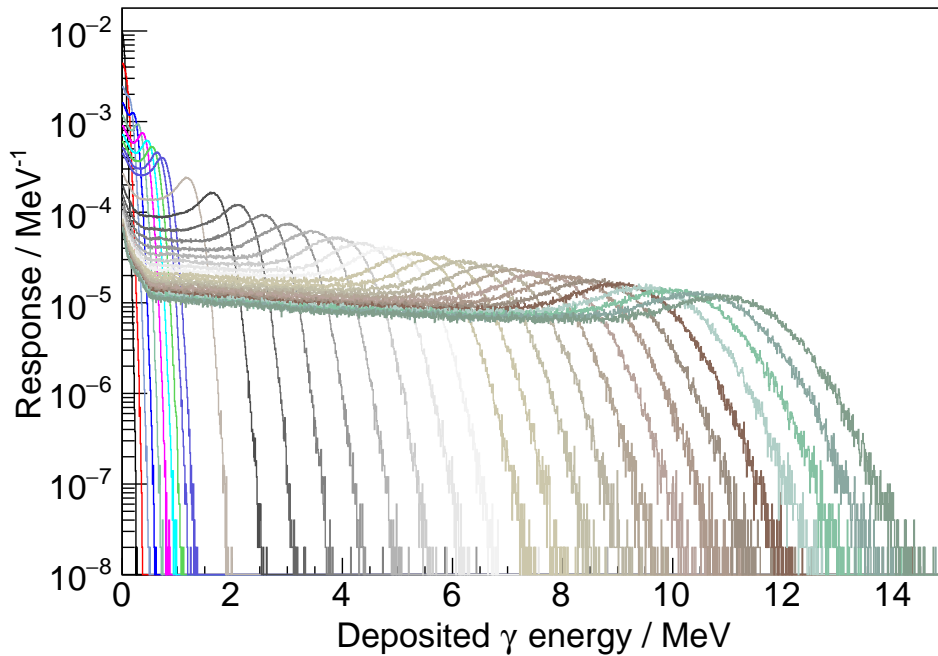
FIGURE 3.21: Set of simulated responses $R_d(E_d, E_\gamma)$ for a single detector and for the case of the NaCl sample obtained with Geant4 simulations consisting of 5×10^7 events, for $E_\gamma = 0.1, ..., 0.9, 1.0, 1.5, ..., 11.5, 12.0$ MeV.

3.6.3 PHWT correction factors

There are several effects that must be accounted for during the application of the PHWT:

- The finite **electronic threshold** E_{thr} placed on the data in software, 250 keV in this work for all detectors, means that one must account for the 'missing' cascade energy due to the non-detection of low energy gamma-rays which give rise to events with a deposited energy below the threshold, which would otherwise lead to an underestimation of the total energy and therefore of the reaction yield. This effect is usually on the order of a few percent and is thus non-negligible; indeed this is the largest of any of the systematic corrections applied to the data and is therefore likely one of the the largest sources of systematic uncertainty contributing to the final experimental yield, aside from the neutron flux.

- **Internal conversion** also leads to missing cascade energy, usually on the order of 0.1%. Electrons are quickly stopped within the target producing x-rays that are also mostly absorbed before reaching the detector.

- In principle there is also a small correction due to the fact that there is a finite probability for **multiple hits**, where two or more of the gamma rays from
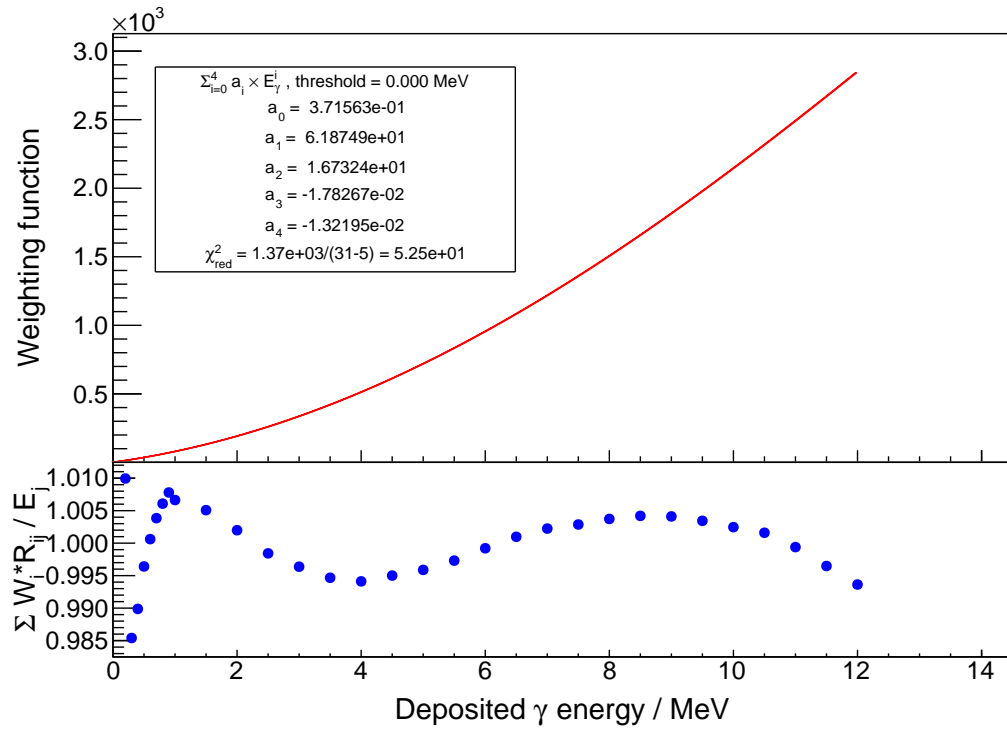
FIGURE 3.22: Weighting function for the case of the NaCl sample for one of the detectors used in this work along with the 'quality factor' $(\sum_i W(E_i)R(E_i, E_j))/E_j$ shown in the bottom panel (also discussed in the text).

a single cascade deposit energy in the same detector. This is problematic because the weighting functions are in general convex functions meaning that $W(E_1 + E_2) \neq W(E_1) + W(E_2)$.

Each of these corrections are in general larger for heavy nuclei where the level spacing is smaller leading to a softer gamma-ray spectrum (in turn leading to a larger number of 'missed' gamma-rays) with larger multiplicity (leading to a larger multiple-hit effect), and where internal conversion branching is larger. The corrections are nevertheless highly specific to the nucleus under study.

Since the saturated resonance method is used to normalise the yield, it can happen that the threshold and internal conversion effects described above, which are also present in the Au yield, act to cancel the same effects present for the sample of interest. This is not very accurate however, especially when the sample of interest is light as is the case in this work. A second way of dealing with the threshold effect is to impose the limit $E_d > E_{thr}$ rather than $E_d > 0$ during the calculation of the weighting function in Equation 3.15. This automatically accounts for the fraction of the responses R_d lying below E_{thr} and so partially corrects for the threshold effect, but does not account for the missing counts from events where $E_\gamma < E_{thr}$. The method adopted in

this work, and the most accurate method, is to use a specialist gamma-ray cascade generator such as NuDEX [72], DEGEN [73], or DICEBOX [74] to use as input to a Monte-Carlo simulation in order to fold the realistic gamma-ray energy spectrum from the calculated cascades with the detector responses. The correction factors above can then be evaluated by comparing the measured and calculated deposited energy spectra, which allows one to estimate how many counts, or how much of the 'total energy', has been missed below the threshold. This is described in detail below.

In this work, cascades from the NuDEX code (for ^{36}Cl and ^{24}Na) and DEGEN code (for ^{198}Au) were used [75] — details of the simulation method and results are given in Appendix A. It was assumed in this work that the gamma-ray energy spectrum for cascades calculated for thermal neutron capture on each of the isotopes of interest would be sufficient to use over the whole neutron energy range of interest, around 200 keV; this means a range of excitation energy $S_n \leq E^\star \leq S_n + 200$ keV. Since $S_n \sim 10$ MeV, the range of excitation energies is relatively small meaning this is not a bad assumption. It may be expected that differences could however arise from the fact that different resonances have different J^π which in principle will affect the cascade pattern from resonance to resonance. Since the resolution of the detectors is also poor, it was assumed that these small differences would average out over many cascades and would not have a significant impact on the deposited energy spectrum which are used to make the PHWT corrections. Moreover, one can see qualitatively from Figure 3.23 that the shape of the deposited energy spectrum does not change significantly with neutron energy for the same nucleus, and indeed that the shape is similar for Na and Cl; this provides further confidence in the above assumption.

To test the accuracy of the cascade generators, the gamma-ray energy spectrum associated with cascades from neutron capture on the NaCl and Au samples were used as source terms in the Geant4 simulations consisting of 10^6 cascades, where the experimental broadening (discussed in Section 3.5.2) was also included. The results of the simulations are shown in Figure 3.24. After subtracting the various background sources from the experimental data (which are described in detail in Section 3.7), the experimental and simulated deposited energy spectra, $C^{exp}(E_d)$ and $C^{sim}(E_d)$, agree very well meaning that the cascades are suitable to use to make the corrections described above. For Au, the $C^{exp}(E_d)$ is obtained by gating on the 4.9 eV saturated resonance, and for the NaCl sample it is obtained by gating on the neutron energy range $1 \leq E_n \leq 100$ eV. Based on the assumption stated above that the cascades are independent of neutron energy, it is therefore assumed that for the purpose of making what is a percent-level correction that these deposited energy spectra are also independent of neutron energy. The correction to the experimental data is thus made as follows:
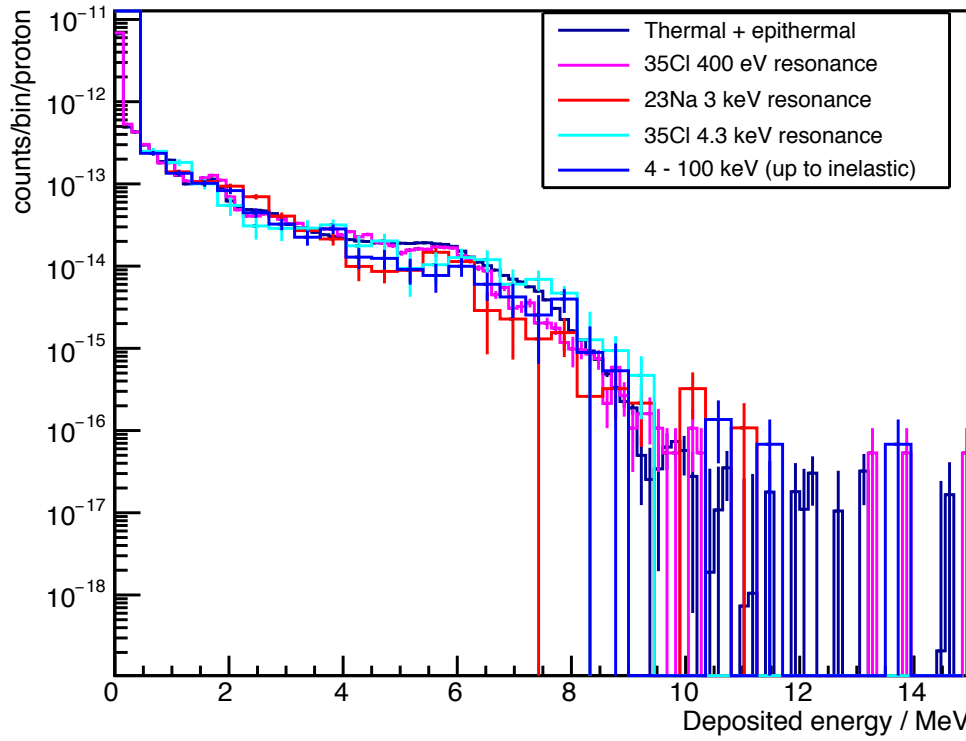
FIGURE 3.23: Deposited energy spectra for different neutron energy cuts for the NaCl sample with gates on different energy regions and on resonances of both Cl and Na.

The desired experimental weighted spectrum is given by

$$C_w(E_n) \underset{\text{Eq. 3.12}}{=} \sum_{E_d > 0} C^{exp}(E_n, E_d).W(E_d), \qquad (3.17)$$

where $C^{exp}(E_n, E_d)$ is the background subtracted experimental counting distribution and the lower deposited energy limit is zero. Since internally converted states can be included or not included in the simulated cascades and the threshold can be set to zero in the simulations, the weighted spectrum corrected for the electronic threshold and internal conversion (IC) is given by

$$C_w(E_n) = \left(\sum_{E_d > E_{th}} C^{exp}(E_n, E_d).W(E_d) \right) \times \underbrace{\frac{\sum_{E_d > 0} C^{sim}_{\text{No IC}}(E_d).W(E_d)}{\sum_{E_d > E_{th}} C^{sim}_{\text{with IC}}(E_d).W(E_d)}}_{f_{PHWT}}, \qquad (3.18)$$

where E_{thr} is the electronic threshold on the deposited energy, and where the fraction f_{PHWT} is the correction that appears in Equation 3.14. The same number of cascades are used in the simulation of $C^{sim}_{\text{No IC}}$ and $C^{sim}_{\text{with IC}}$. The correction factors for the four detectors are similar, and are shown for one detector in Table 3.4 for the case of three electronic thresholds, one of which (250 keV) is the one used in this work. The simulations and associated correction factors are further validated by comparing the

experimental weighted counting rates of Equation 3.18 with different thresholds, using the appropriate correction factor from Table 3.4. Assuming that the simulated detector responses, weighting functions and simulated cascades are accurate, the corrected weighted counting rates should be consistent for different choices of electronic threshold. A comparison of three such count rates for three thresholds (shown still as a function of time-of-flight) is shown in Figure 3.25 where it is seen that the agreement is once again very good.

TABLE 3.4: The threshold and internal conversion correction factors associated with the application of the pulse height weighting technique for different electronic thresholds (250 keV in this work) and for the two nuclei relevant to this work: ^{35}Cl being the isotope of interest and ^{197}Au for normalisation.

Threshold (MeV)	f_{PHWT} for the reaction	
	$n+^{35}$Cl	$n+^{197}$Au
0.25	1.0151	1.0432
0.50	1.0502	1.0893
0.75	1.0944	1.1487

The final small correction due to multiple hits (mentioned in Section 3.5.4) can be evaluated using the experimental data. Since the WF are convex functions calculated assuming a response from single gamma-rays, when two or more gamma-rays deposit energy in a single detector, the weight applied to the event is overestimated: $W(E_1 + E_2) > W(E_1) + W(E_2)$. By considering coincident events between adjacent detectors, one can estimate the multiple hit effect on the weighted data by selecting the coincident events (see Figure 3.18) and comparing $W(E_1 + E_2)$ with $W(E_1) + W(E_2)$. It is assumed that the probability for multiple gamma-rays interacting with a single detector is the same as the probability of them interacting with adjacent detectors. For the Au sample used for normalisation, the effect is 1.9% and for the NaCl sample, the effect is 1.7% — therefore the effect almost completely cancels in the saturated resonance normalisation procedure, and the remaining 0.2% is negligible in comparison to the % level uncertainties associated with the neutron flux and those discussed in the next section.
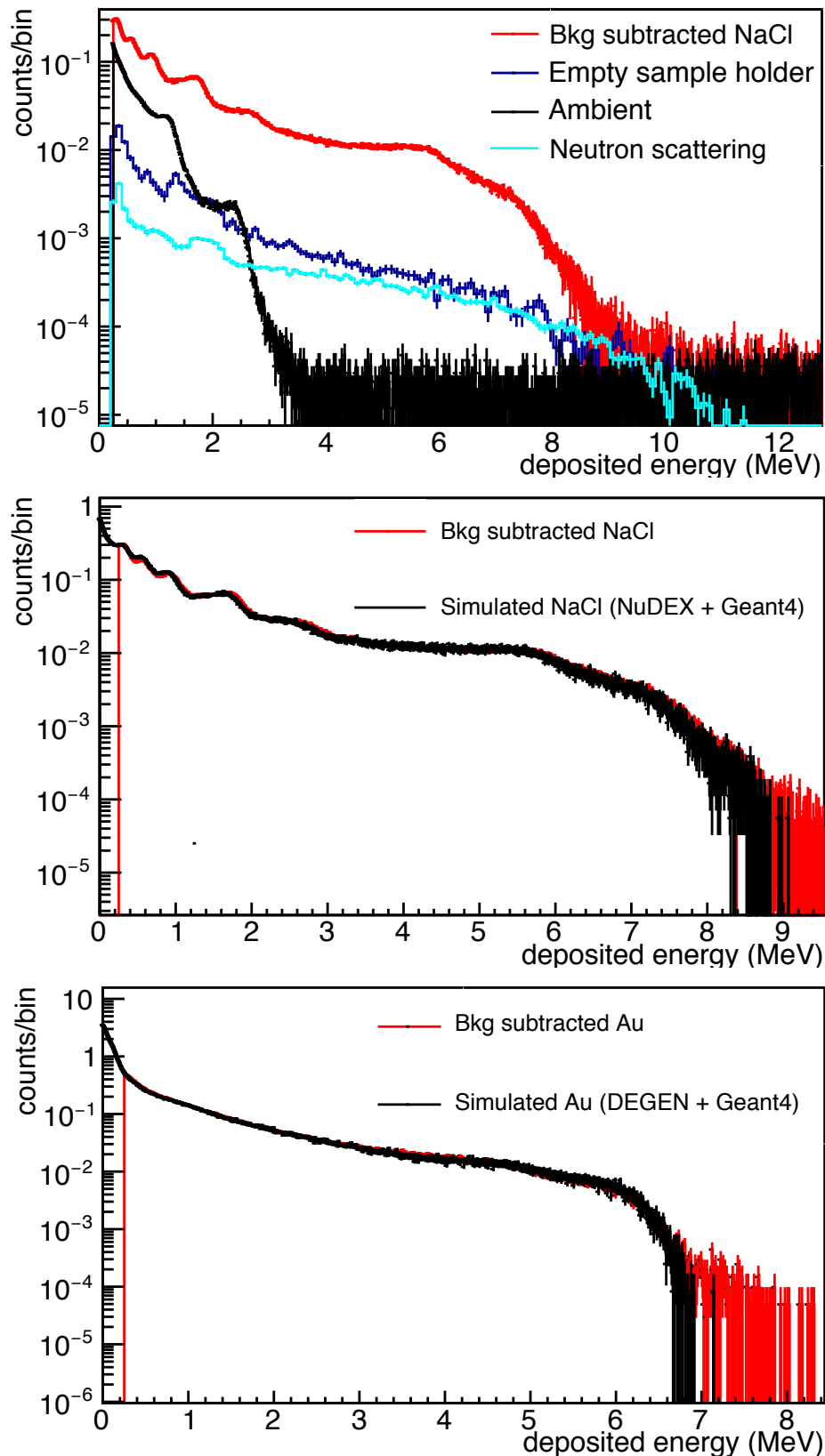
FIGURE 3.24: (Top) Deposited energy spectrum for the NaCl sample for one detector — background components are shown for reference (see Section 3.7 for further details). (Middle) Comparison of background subtracted deposited energy spectrum C^{exp} with the equivalent Monte-Carlo simulation C^{sim} (NuDEX+Geant4). (Bottom) Same as middle plot, but for the Au sample with cascades from the DEGEN code. For all plots, the lower energy threshold on the experimental data is 250 keV, below which are the 'missing counts' to be accounted for.
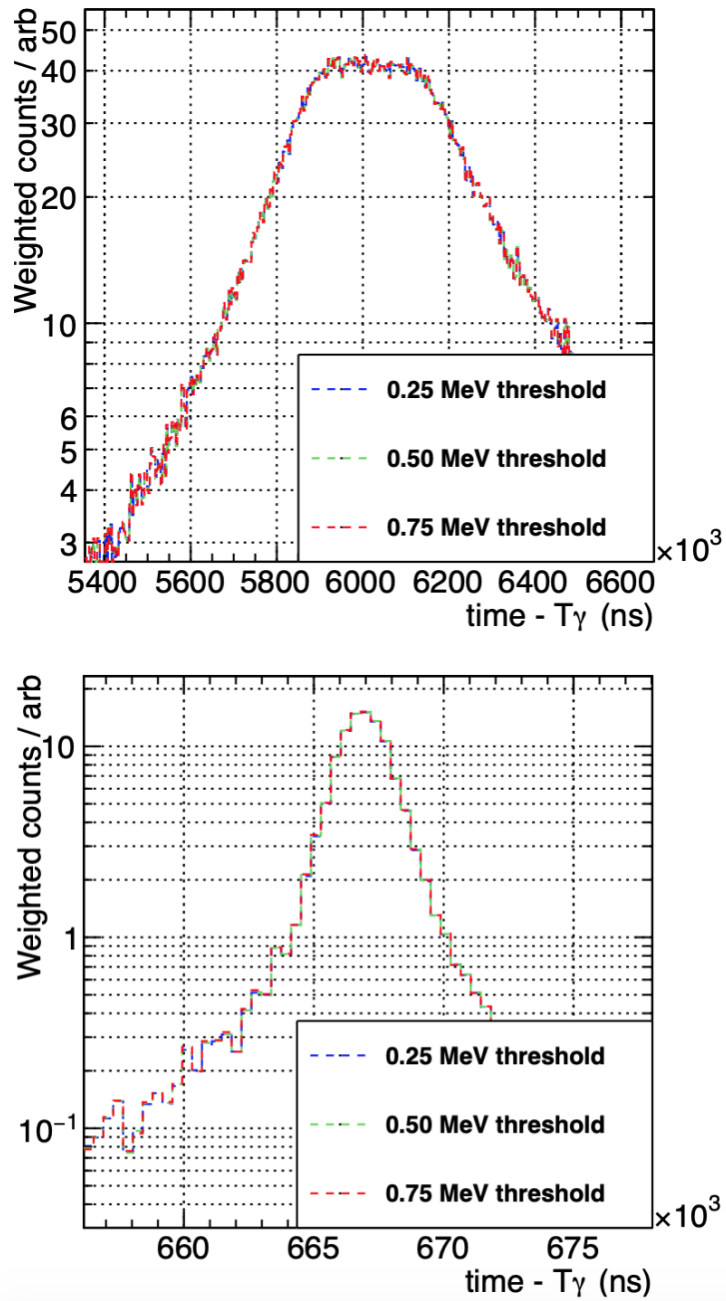
FIGURE 3.25: Examples of corrected experimental weighted counts for three different electronic thresholds, calculated using Equation 3.17 with the correction factors in Table 3.4, for the ^{197}Au saturated resonance at 4.9 eV (top) and the first (and largest) resonance of ^{35}Cl at 397 eV (bottom).

3.6.4 PHWT uncertainties and accuracy

There are two sources of uncertainty to consider:

1. the intrinsic uncertainty associated with the calculation and application of the WF

2. the uncertainties from cascade modelling which are propagated through the Monte-Carlo simulation to obtain the correction factors discussed in the previous section.

It is the systematic uncertainty that is important for the first source since the statistical errors can be made arbitrarily small when simulating the response functions R_d for the WF calculation. The systematic uncertainty is evaluated using the simulations described in the previous section. By definition, if N_c cascades are fed into the simulation, each with a total cascade energy E_c, then

$$\sum_{E_d>0} C^{sim}(E_d)W(E_d) = N_c E_c. \tag{3.19}$$

Therefore for a given weighting function and set of cascades convolved with the response of the detection system, the quantity $\sum_{E_d>0} C^{sim}(E_d)W(E_d)/N_c E_c$ should be unity for the ideal WF. Studying the deviation from unity gives a measure of the systematic uncertainty; this 'quality factor' is shown in Table 3.5 for each detector, set of cascades and weighting function (the weighting function is the same for Cl and Na since they are contained in the same sample). The conclusion is that the systematic uncertainty associated with the application of the WF to the experimental data in this work is around 1%.

TABLE 3.5: Weighting function quality factors defined in the text for each detector and for the cascades generated for the two relevant isotopes.

Detector	Quality factor, $\sum_{E_d>0} C^{sim}(E_d)W(E_d)/N_c E_c$	
	n+^{35}Cl	n+^{197}Au
1	1.0067	0.9939
2	1.0027	1.0008
3	0.9980	0.9950
4	1.0037	0.9937

The uncertainty associated with the correction factors calculated using the cascade generators is not straightforward to quantify. In light of the similarity between the simulated and experimental spectra in Figures 3.24 and 3.25, and the magnitude of

the corrections for the 250 keV threshold in Table 3.4, a conservative estimate of 2% uncertainty is assumed.

3.7 Background study and subtraction

There are several background components that one must subtract in order to produce the desired reaction yield given by Equation 3.13. For the resolved resonance region (RRR), the complete subtraction is not as crucial since any small residual background can be absorbed into the resonance fitting procedure detailed in Section 3.9.1. An accurate background subtraction is most important for the unresolved resonance region (URR) where there are no resonant structures and where the point-wise cross section is of interest; as will be shown however, for the case of this specific measurement, the high background level has been prohibitive for both the RRR and URR — an accurate assessment of the background is nevertheless useful in determining the limitations of the measurement. The limitation in this measurement is related to the fact that ${}^{35}Cl$ is a light nucleus and therefore has both a relatively small capture cross section a high scattering-to-capture cross section ratio, as can be seen in Figure 1.1, meaning that the signal-to-background is not as favourable as for the cases of heavier nuclei with larger cross sections and smaller scattering-to-capture ratios, more usually measured at n_TOF. This measurement therefore provides a good opportunity for understanding the limitations of EAR1 at n_TOF for making capture measurements of other such light nuclei.

After converting to neutron energy, applying the dead-time corrections, weighting functions and associated correction factors, the overall situation is shown in Figure 3.26, where the individual background components and their evaluation are discussed in depth below; the deposited energy spectra associated with the background components for the NaCl sample measurement were shown in Figure 3.24. Background subtraction is made especially difficult due to the fact that there are many processes that occur over many orders of magnitude, both in terms of neutron time-of-flight (and hence neutron energy) and their relative counting rates. A combination of experimental measurements and simulations are therefore used to evaluate the following components:

- The **ambient background**, or beam-off background, accounts for the naturally occurring background radiation such as from cosmic rays and the surrounding materials, including ${}^{40}K$ present in the concrete walls of the bunker, as well as the possible radioactivity of the sample being studied.

- The **sample independent background** is defined as those counts, aside from the ambient background, measured in the absence of the sample of interest but when the neutron beam is on. Sources include the interaction of neutrons with the vacuum windows, sample holder and other surrounding materials.
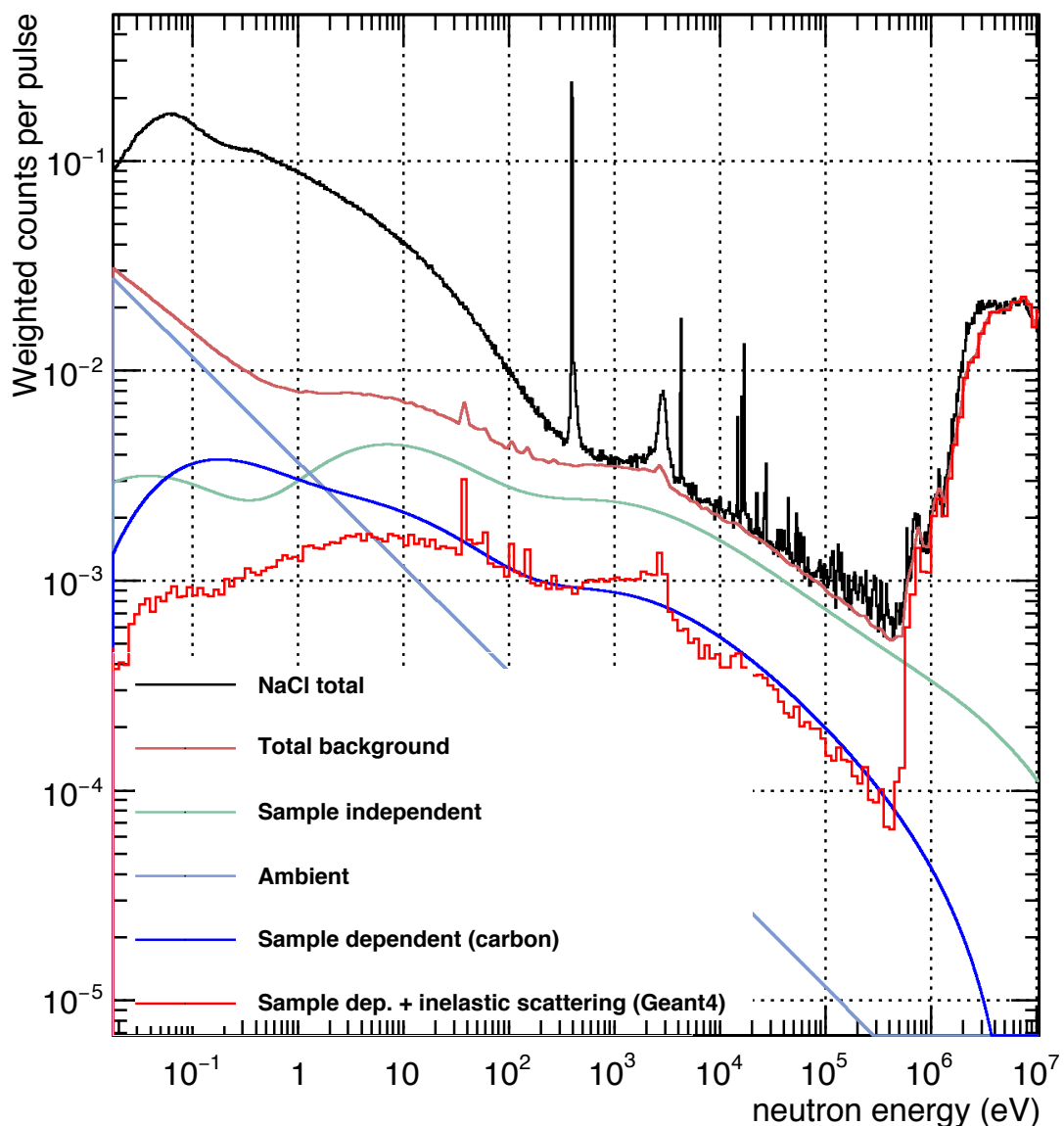
FIGURE 3.26: Total weighted counting rates from all detectors for the NaCl sample with all background components and methods for their evaluation, described in the text. The 'Total background' uses the Geant4 'sample dependent' background.

- The **sample dependent background** is the most complicated of background sources partly due to the fact that by definition it cannot be measured directly. It is due to neutrons scattering from the sample; there are two sub-components, *delayed* and *prompt*. The **delayed component** arises from neutrons that scatter from the sample material and interact with other materials in the experimental bunker, creating gamma-rays which are subsequently detected and which are assigned a time-of-flight that is not strongly correlated with the energy of the neutron that initiated the event giving rise to a smooth background. For this work, this component was evaluated both experimentally and by using Monte-Carlo simulations taking the entire geometry of the set-up into account.

The **prompt component** comes from the cases where neutrons scatter from the sample and interact immediately with the detectors and support materials. In this case, the time-of-flight is strongly correlated with the neutron energy, and in the case where for a specific resonance $\Gamma_n \gg \Gamma_\gamma$, the measured shape of the resonance can be artificially modified. The Legnaro-C_6D_6 detectors used in this work were designed to be as insensitive to neutrons as possible, as discussed in Section 3.2.3, and the relative scattering and capture widths of the resonances studied in this work mean that this prompt component is negligible, as will be demonstrated in the resonance analysis.

- **In beam gamma-rays** accompany neutrons in the beam and originate partially from the spallation reactions at the neutron source, but mostly from the moderating process as was discussed in Section 3.2; these gamma-rays can be Compton scattered by the sample and directly into the detectors. This background is partially suppressed by placing the detectors in the backwards hemisphere, but the overall result is a smoothly varying background that can be evaluated by measuring a sample with a high Z such as lead before scaling appropriately. It can be significant for samples with high atomic numbers, but for this work however, this background component was negligible because of the relatively low atomic number of the NaCl target.

- For higher neutron energies where neutrons have enough energy to populate the first excited states of the target nuclei (around a few 100 keV), **inelastic scattering** begins to dominate the count rate. Since this background is highly sample dependent, no measurement can be performed to determine its magnitude. As will be shown below, the counting rate from this background is several orders of magnitude larger than that from capture meaning that even small errors in simulations of the effect can be larger than the remaining counts after subtraction; this effect therefore dictates the upper neutron energy limit of the measurement. Up to $E_n \approx 200\text{-}300$ keV however, this background is automatically rejected because of the deposited energy threshold placed on the detectors (since by definition the minimum detectable gamma-ray energy is equal to the threshold).

The procedure for the measurement and subtraction of these components is given below. For each component, the counting spectra are weighted, and where possible are parametrised and fit in order to reduce statistical uncertainty; in general the background components are smooth as a function of time-of-flight and beam time was predominantly spent measuring the sample of interest meaning that in general the statistical uncertainties associated with the background runs are larger than those for the NaCl sample runs.

Ambient background

By taking measurement runs without the neutron beam, the ambient background is determined. A 'calibration trigger' (also used for calibration source data acquisition) is artificially generated to initiate data acquisition in the absence of the PS trigger and runs for the same 100 ms as for the proton bunches, allowing a 'time-of-flight' to be assigned to each event. In a run containing a sample, the level of the ambient background is proportional to the number of neutron bunches (the number of proton pulses). Therefore to subtract the ambient background from a 'sample in' measurement, the ambient counting spectrum is scaled according to the number of 'ambient bunches' $B_{ambient}$ (how many false triggers were used for its measurement) and the number of actual beam bunches B. The background subtracted spectrum is then given by

$$C_{sub} = C_{total} - \frac{B}{B_{ambient}} C_{ambient}. \qquad (3.20)$$

In principle there is an additional ambient component due to the neutron activation of the sample material; in practice this additional component is negligible, as was found by checking beam-off runs from before the measurement and after several hours of irradiation. The weighted spectrum $C_{ambient}/B_{ambient}$ is shown in Figure 3.27 as a function of $t - t_\gamma$. In the interest of reducing statistical error, the background spectra were parametrised and fitted. Since in this work isolethargic binning is used (to facilitate the visibility of structure across many orders of magnitude), for the case of the ambient background where the count rate is constant in time, it is parametrised as $C_{ambient} = a + be^{t-t_\gamma}$.

For the events corresponding to the 'dedicated' beam mode, the ambient background is smaller relative to the total count rate than for the case of the less intense 'parasitic' mode as shown in Figure 3.28; the results of subtracting the ambient components for both modes for the NaCl and Au samples are also shown in Figure 3.28 where the subtracted spectra for parasitic and dedicated are the same as expected.
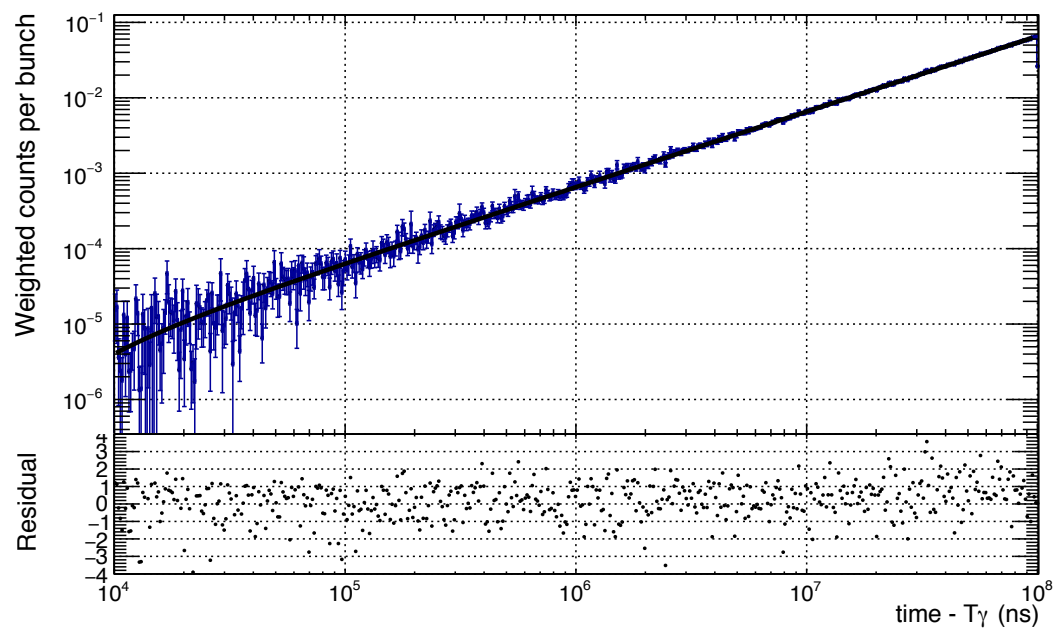
FIGURE 3.27: Ambient background measurement for one of the detectors, where the solid line indicates a fit to the data where the functional form is given in the text for which $\chi^2/ndof = 1.34$.
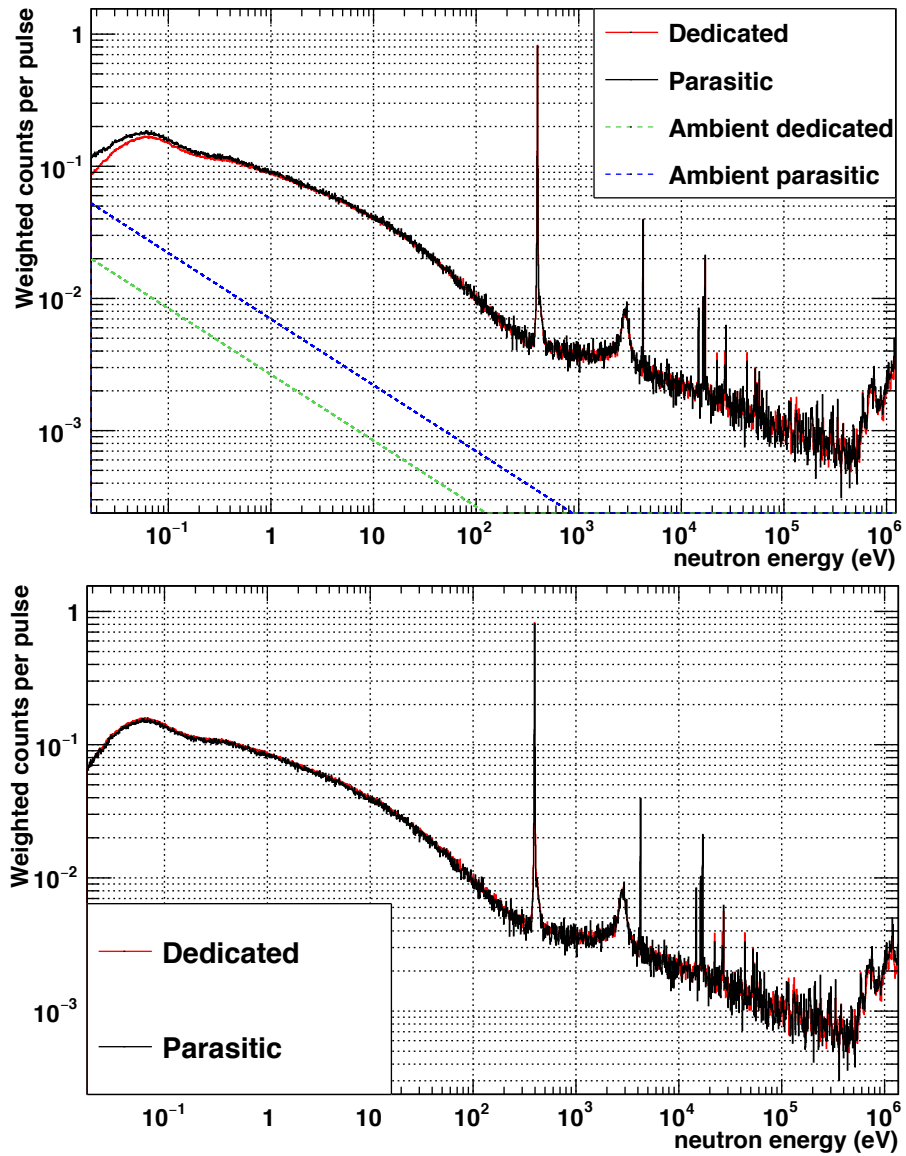
FIGURE 3.28: (Top) Total counting rates as a function of time-of-flight for the NaCl sample for both beam modes with the appropriate level of ambient background. (Bottom) Ambient subtracted count rates for parasitic and dedicated beam modes for which there is good agreement.

Sample independent background

This background component is measured by taking runs with the empty sample holder made from two thin mylar backings, glue and an aluminium ring used to fix the sample to the target exchanger. For the resolved resonance region it makes the largest contribution to the background as shown in Figure 3.26. The empty sample absolute counting error for neutron energies in the resolved resonance region is around twice that for the NaCl sample measurement. Therefore after subtracting the appropriate ambient contribution as per Equation 3.20, a fit was performed once again to reduce statistical error in an attempt to improve the statistical error in the final reaction yield for fitting the resonances. The small deviations from the phenomenological fit are absorbed into the resonance fitting procedure detailed in Section 3.9.1. The background component normalised to a single nominal proton pulse and a fit to the data are shown in Figure 3.29. It should be noted that the choice of the nominal number of protons per bunch is arbitrary, as long as a consistent value is used for each of the 'beam on' measurements (sample under study, background measurements and the Au sample used for normalisation).
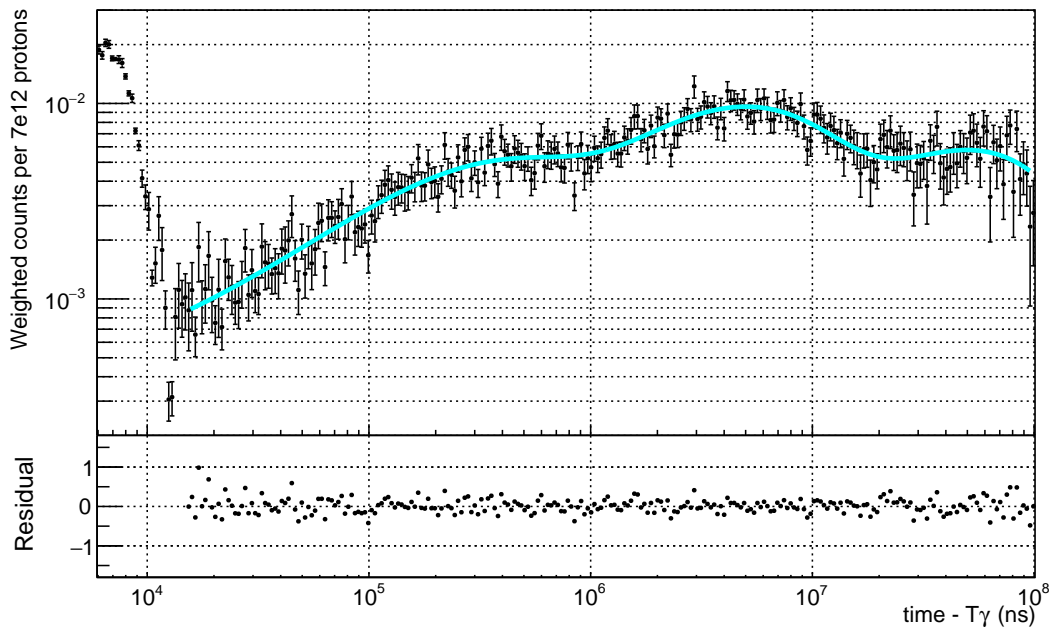
FIGURE 3.29: Sample independent background contribution for one detector normalised to one nominal proton pulse of 7×10^{12} protons, measured with the empty sample holder. The solid line denotes a fit to the data in the region of interest with $\chi^2/ndof = 0.85$, where the residuals are shown in the bottom panel. Inelastic neutron scattering on the empty sample holder and surrounding materials is clearly visible below time-of-flight $\approx 1.5 \times 10^4$ ns ($E_n \approx 500$ keV).

This component was parametrised using the phenomenological function

$$C(t - t_\gamma) = a_0 + \sum_{i=1}^{3} a_i \left(1 - e^{-b_i(t-t_\gamma)}\right) e^{-c_i(t-t_\gamma)} \tag{3.21}$$

over the region $1.5 \times 10^4 < t - t_\gamma < 10^8$ ns. Both the 'sample in' measurements and background components measured with the beam on scale with the number of neutrons (and hence the number of protons incident on the spallation target). Therefore after accounting for the ambient background, the subtraction is made according to

$$C_{sub} = \frac{C_S}{n_p^S} - \frac{C_E}{n_p^E}, \tag{3.22}$$

where n_p^S and n_p^E are the integrated number of protons for the 'sample in' and 'empty' runs respectively, C_{sub} is the desired counting spectrum with ambient and sample independent background subtracted, C_S is the ambient subtracted 'sample in' spectrum, and C_E/n_p^E is the quantity that is given by the fit to the experimental data shown in Figure 3.29. The number of protons for normalising data was taken from the BCT pulse intensity value from the PS, as discussed in Section 3.5.1.

Sample dependent background: *prompt* component

Accounting for the prompt component of the sample dependent background is more generally referred to as the neutron sensitivity correction, and pertains to a resonance-by-resonance correction based on the scattering to capture ratio. For resonances with large Γ_n/Γ_γ, it may be expected that the strength of the measured capture resonance would be artificially increased due to events associated with neutrons that have scattered from the sample and been captured within detection set-up (since the detectors do not directly detect neutrons, but the gamma-rays as a result of their capture).

Here, the neutron sensitivity α_{ns} is defined as the ratio between the probability to detect a neutron and that to detect a gamma-ray from a capture cascade. This is in principle neutron energy and sample dependent, but for the Legnaro-C_6D_6 set-up in this work its magnitude is $\alpha_{ns} \approx 10^{-5}$ [59, 60]. For a particular resonance, the probability that a given signal was from a neutron event rather than a gamma-ray originating from capture in the sample is given by

$$P_{ns} = \alpha_{ns} \frac{\Gamma_n}{\Gamma_\gamma} \tag{3.23}$$

such that the correction applied to the yield measured for a given resonance to account for the overestimation of the strength is given by

$$f_{ns} = \frac{1}{1 + P_{ns}}. \tag{3.24}$$

For the resonances measured in this work, the maximum Γ_n / Γ_γ was ≈ 400, implying a neutron sensitivity of $P_{ns} \sim 10^{-3}$ making the correction negligible with respect to the other multiple systematic uncertainties on the percent level (this includes the Au measurements for normalisation). It is this correction which for older measurements, performed at any time-of-flight facility, can be significant, with P_{ns} on the order of unity. The detector design described in Section 3.2.3 is predominantly based around reducing this correction as far as possible.

Sample dependent background: *delayed* component

Due to the complicated nature of this background, two independent methods have been used for its evaluation. The first of the two methods is based on the measurement of a 'pure neutron scatterer', the second is based on Monte-Carlo simulations. Cross checking with two methods is especially important for this work since the sample (NaCl) has a particularly high scattering-to-capture ratio and it was therefore anticipated that the sample dependent component would represent a significant contribution to the overall background.

For the first method, it is assumed that this background component is smooth and that it does not depend strongly on the precise energy dependence of the elastic scattering cross section of the sample material, but only on its average magnitude; the elastic scattering cross section is reasonably constant with neutron energy as shown in Figure 1.1. Carbon is an efficient neutron scatterer with a large elastic scattering-to-capture ratio of $\sigma_{n,n}/\sigma_{n,\gamma} \sim 10^4$ at $E_n = 1$ eV, $\sim 10^5$ at 1 keV, and $\sim 10^6$ at 100 keV; one can therefore be confident that the experimental counting rate when measuring a carbon sample is dominated by neutron scattering, the source of the sample dependent background. The sample dependent counting rate for the NaCl sample C_{SD}^{NaCl} was estimated by scaling the counting rate measured with the natural carbon sample C_C appropriately by taking the different areal densities n and elastic scattering cross sections $\sigma_{n,n}$ into account. As the neutron flux $\phi(E_n)$ and scattering cross sections are non-constant, a spectrum averaged ratio of the elastic cross sections was used:

$$C_{SD}^{NaCl} = C_C \frac{n_{NaCl}}{n_C} \frac{\int_{E_{low}}^{E_{high}} \phi(E_n) \frac{\sigma_{n,n}^{NaCl}(E_n)}{\sigma_{n,n}^{C}(E_n)} dE_n}{\int_{E_{low}}^{E_{high}} \phi(E_n) dE_n}, \tag{3.25}$$

where E_{low} and E_{high} were somewhat arbitrarily chosen to be 0.1 eV and 10^7 eV respectively giving an overall scaling factor $C_{SD}^{NaCl}/C_C = 0.169$. The ambient and empty counting rates were subtracted from the carbon counting spectrum using the fits from the previous sections, and the background subtracted spectrum was subsequently fit with the same phenomenological function in Equation 3.21 before scaling. The data and associated fit are shown in Figure 3.30; the scaled fit taken to be the sample independent background for the NaCl sample is also shown. The result converted to neutron energy is shown in Figure 3.31 alongside the remaining NaCl count rate after the ambient and sample independent backgrounds have been subtracted.
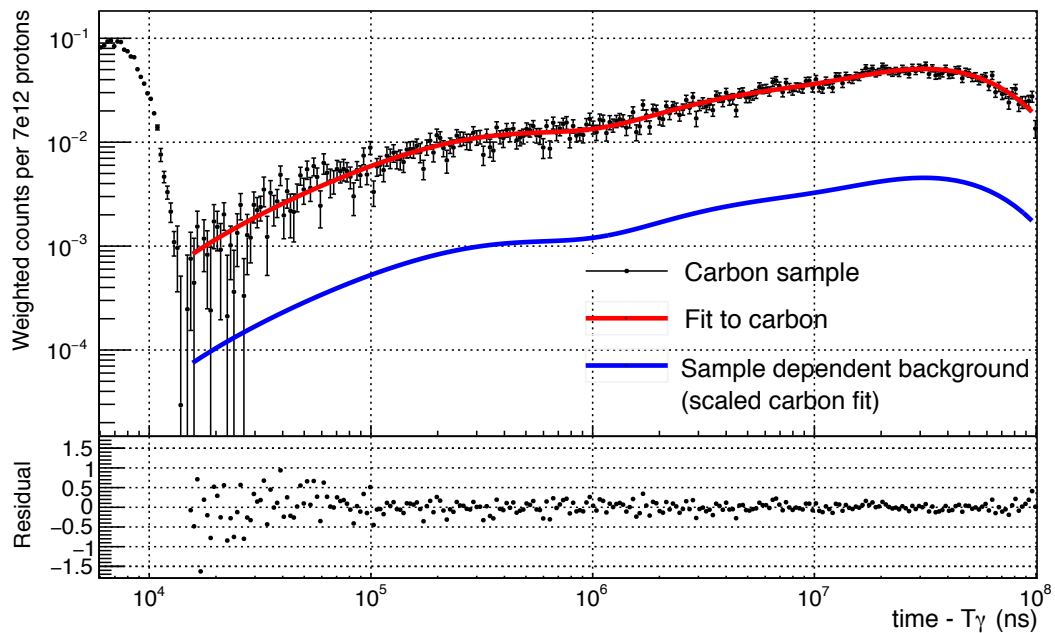
FIGURE 3.30: Count rate measured with the natural carbon sample (ambient and sample independent background subtracted), and associated fit. The scaled fit taken to be the sample dependent background contribution is also shown in blue. Results shown for one detector. For reference, a time-of-flight of 4×10^4 ns (the point at which the fit becomes poor) corresponds to a neutron energy of around 100 keV.

When the elastic scattering cross section is small relative to the capture cross section, the above method may be sufficient to evaluate the sample dependent background since its magnitude will be small relative to the capture counting rate, and hence any small deviations from the assumptions stated above become negligible. As shown in Figure 3.31 however, the sample dependent background evaluated using the method above accounts for a large fraction of the remaining counts, as anticipated. Given the significance of this background and the approximate nature of the carbon scaling method, a second method based on Monte-Carlo simulations was also applied.
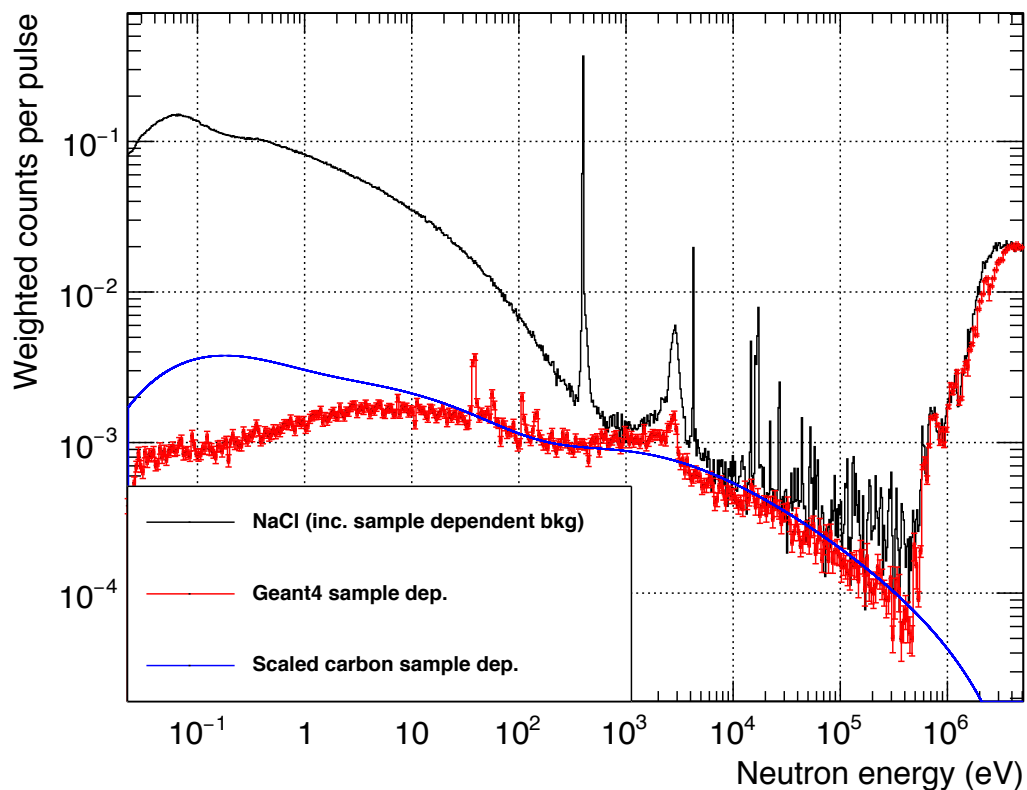
FIGURE 3.31: Experimental NaCl counting rate including the sample dependent background and the results of the two methods for its evaluation, shown for the sum of all four detectors. For neutron energies > 1 keV, the counting rate is dominated by background. The sharp increase around 400 keV is due to inelastic scattering on the NaCl sample, which the Geant4 simulation describes very well.

A comprehensive Monte-Carlo study of the backgrounds and their sources present at n_TOF EAR1 was performed by Žugec *et al.* [61] in which an accurate representation of the entire experimental bunker and its contents was implemented in Geant4. It was shown as expected that for the sample dependent background there is in general a non-trivial relation between the true neutron energy that is the initiator of a background event and the neutron energy one would determine via the time-of-flight method; this partially relates to the fact that neutrons can be scattered around the bunker for some finite time before being captured giving rise to gamma-rays, leading to a delayed background. Furthermore, there are reaction channels specific to each sample that give rise to delayed background events. For example in the the case of a carbon sample, the simulations showed that the $^{12}C(n, p)$ threshold reaction produces the β^- emitter ^{12}B, which has a half-life of 20.2 ms and a mean electron energy of $\langle E_\beta \rangle = 6.35$ MeV; the energetic electrons are able to penetrate into the active C_6D_6 detection volume giving rise to signals tens of ms after the (n, p) event (for reference, thermal neutrons have a time-of-flight of around 84 ms). In practice therefore, it is insufficient to measure one sample and simply scale the result to obtain the result relevant to the sample of

interest — the only reliable way to obtain the sample dependent background is to perform a similar Monte-Carlo study for the specific sample being studied.

The same simulations as those described above were run for the case of our NaCl sample and experimental set-up; the Geant4 geometry consisted of that shown in Figure 3.12 and that of Reference [61]. Figure 3.32 summarises the results for the sample dependent background. The effects described above leading to a non-correlation between 'real' neutron energy (energy of the neutron that came from the spallation source) and 'measured' neutron energy (that would be determined from the time-of-flight) can be seen, where notable structures are the horizontal bands at 'real' neutron energies of ≈ 3 keV and ≈ 1 MeV which correspond to the strong scattering resonance of ^{23}Na and the peak of the neutron flux respectively. The data from the simulation were analysed in exactly the same way as for the experimental data, applying the same experimental broadening, weighting functions and deposited energy thresholds. The result of the simulation is shown in Figure 3.31 alongside the result of the scaling method, after converting from time-of-flight to neutron energy, and the experimental data. As expected, the structures seen in the simulation are not captured by the carbon scaling method, but overall the agreement between the two methods is very good for the resonance region. The difference at neutron energies < 100 eV is due to the differences in the delayed component from sample specific threshold reactions discussed above. From around 400 keV, the simulation reproduces the inelastic scattering on the NaCl sample very well; nevertheless, the magnitude of the inelastic scattering component is too great to accurately subtract from the measured NaCl counting rate to yield the capture rate (which is at least two orders of magnitude less), and so the upper limit on the measurement is around 300 keV at best. Due to the fine detail achievable with the simulation, and given its good agreement with the carbon scaling method, the simulation was used in the final background subtraction.

Background determination with 'black resonance filters'

A routinely applied method at neutron time-of-flight facilities for estimating the smooth sample dependent background is to take measurements of the sample of interest and the empty sample holder with filters in the beam; it is described here for completeness. The in-beam filters were described in Section 3.2; thick slabs of materials with sufficiently strong absorption resonances, or 'black' resonances, effectively remove all neutrons from the beam at discrete energies. Therefore the counting rate at the position of these resonances is due entirely to scattered neutrons (the delayed component of the sample dependent background) and other background
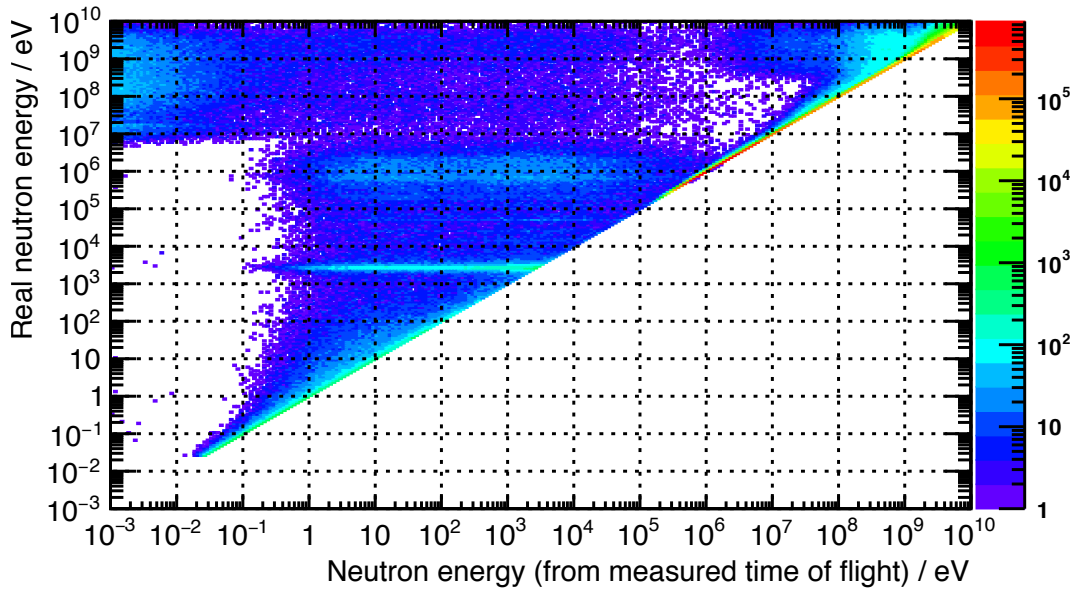
FIGURE 3.32: Geant4 simulation of the correlations between the real neutron energies and those determined from the time-of-flight for the sample dependent background for the NaCl sample, shown for the sum of all four detectors. There are significant delayed components: i.e. the measured energy is less than the real energy, since the time-of-flight measurement is delayed.

events since there are no neutrons that lead to prompt interactions. The difference in count rates at these resonance energies with the filters in the beam between the empty sample and sample of interest therefore gives the level of the sample dependent background. This provides an independent means of scaling the *shape* of the sample dependent background obtained from the measurement of a pure scatterer (taken from the carbon measurement as described above), to the level of the background measured at the positions of the black resonances; this method bypasses the need to scale the carbon data using prior knowledge of the scattering cross sections. The count rates for the empty and NaCl sample with filters are shown in Figure 3.33. The statistics gathered during the experiment were unfortunately insufficient to be able to derive a meaningful background level, since given the error bars shown in Figure 3.33, the sample dependent background derived from the difference of the empty and sample measurements is essentially consistent with zero. Indeed for times-of-flight relevant to the resonance region, there is no statistically significant difference between the sample and empty measurements; the resonance dips of ^{27}Al (at 34 keV and 86 keV) are not seen above the overall background. At best, the filter measurements in this work confirm that the sample dependent background represents only a small component of the total background, as was found to be the case using the other methods described above (even if this background component is still large in comparison to the count rate from neutron capture).
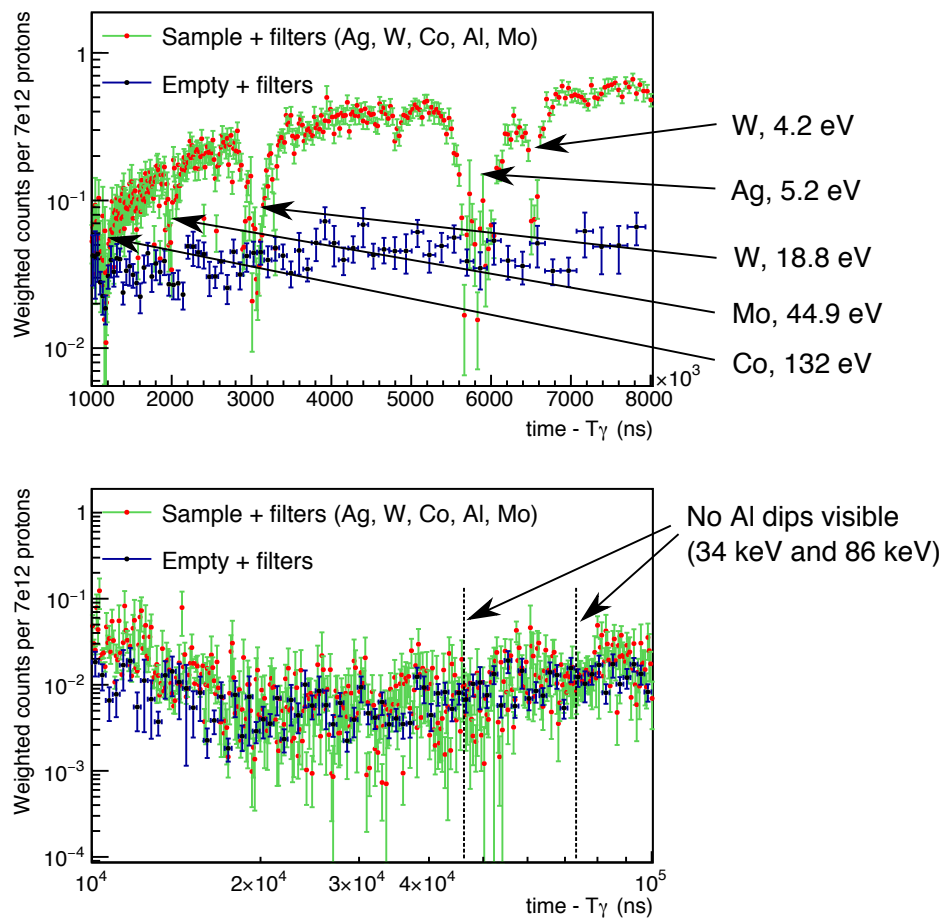
FIGURE 3.33: Counting rates with the NaCl sample and in-beam filters, and the empty sample with the filters for the evaluation of the level of the sample dependent background. The black resonances appear as the sharp dips, and are shown with their corresponding energies labelled. With these statistics, the count rates in the troughs of the black resonances measured with the NaCl sample are consistent with the count rates with the empty sample.

3.7.1 Implications of the background level

As is clear from Figures 3.26 and 3.31, the overall count rate from a few 100 eV (around the first resonance of ^{35}Cl) is dominated by background. After the background subtraction, there are 13 ^{35}Cl resonances visible over the whole neutron energy range — these are studied in detail in the following sections. As shown in Figure 1.1, there are many more weaker resonances (around 250 resonances) which in principle should be resolvable as discussed in Section 3.2.2 — these weaker resonances were however dominated by background, in turn dominated by the delayed sample dependent and sample independent background components. In the past, the subjects of the majority of capture measurements at n_TOF have been heavier nuclei where in general the capture cross section is larger. It is therefore clear that there are limitations at n_TOF

for making measurements of such light nuclei, and that the sources of background, dominated by the sample independent component, need to be addressed to allow more complete resonance analyses. The comprehensive background study presented in this work may form the basis for such a background optimisation.

3.8 Final reaction yield

As discussed in Section 3.6.1, the final ^{35}Cl capture yield is given by

$$Y(E_n) = f_{Norm} f_{PHWT} \frac{C_w(E_n) - B_w(E_n)}{\left(S_n + \frac{A}{A+1}E_n\right)\phi(E_n)}.$$

(3.26)

The evaluation of the normalisation factor f_{Norm}, verification of the shape of the neutron flux $\phi(E_n)$, and combination of the data from each detector and for the two beam modes (parasitic and dedicated) are detailed below.

3.8.1 Verification of the neutron flux

Due to the fluctuations of the ^{10}B content of the water moderator circuit surrounding the spallation target, the low energy neutron flux changes year-by-year and must therefore be monitored during each experiment. This was performed with the SiMon detectors, by monitoring the yield of tritons from the ^{6}Li(n, t) reaction as a function of neutron energy; monitoring tritons rather than alphas is preferred as the triton peak in the deposited energy spectrum is better separated from the noise than is the case for the heavier, less energetic alpha particles. An example deposited energy spectrum from one of the SiMon detectors is shown in Figure 3.34.
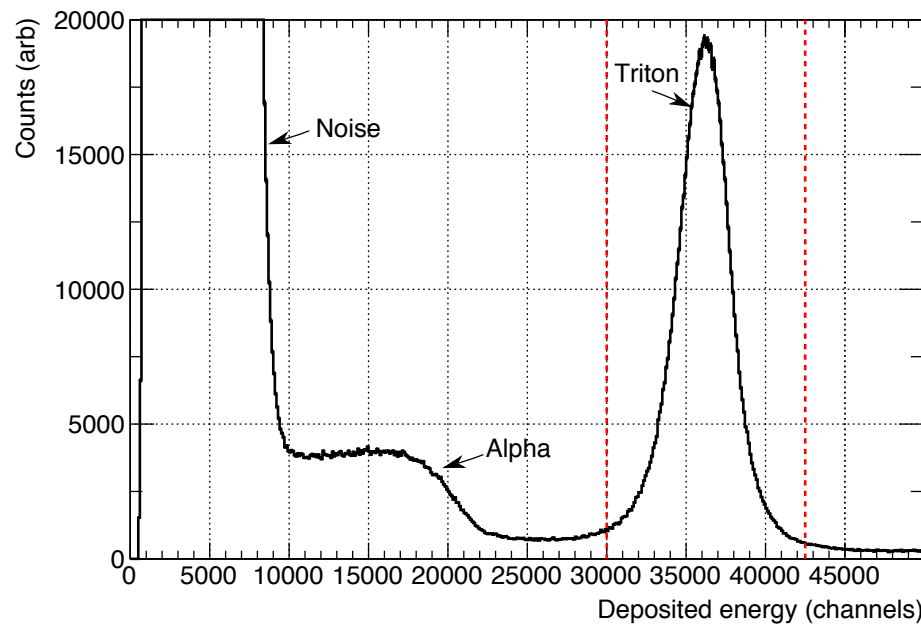
FIGURE 3.34: Deposited energy spectrum for one of the four SiMon silicon detectors where the triton peak within the dashed red lines, used to monitor the shape of the neutron flux, is clearly distinguishable from alpha events and noise.

The thickness of the ^{6}Li foil used as a neutron converter in the SiMon detection system is such that the thin target approximation ($Y = n\sigma$ in Equation 2.2) can be applied in order to determine the shape of the neutron flux using Equations 2.2 and 2.5:

$$\phi(E_n) = \frac{C_{triton}(E_n)}{n\sigma_{n,t}(E_n)\epsilon(E_n)},$$

(3.27)

where the efficiency for the detection of tritons $\epsilon(E_n)$ comes from a Geant4 simulation, and the (n, t) count rate C_{triton} is obtained by gating on the region bound by the dashed lines in Figure 3.34 as a function of neutron energy. In principle the deposited energy gates change with neutron energy due to the changing kinematics with increasing neutron energy, but for energies up to ~ 100 keV, these changes are negligible [52]. The flux determined in this way is shown in Figure 3.35. When suitably normalised, one can see that the boron content was slightly higher during this experiment leading to a reduced flux at neutron energies less than around 10 eV — the maximum difference between the flux evaluation and the measured flux is around 10%. Below 10 eV therefore, the evaluated flux was corrected to take this difference into account before using the flux to calculate the final reaction yield; although there are no ^{35}Cl resonances below 10 eV, the correction is still required since the 4.9 eV gold saturated resonance measured for normalisation, discussed below, also requires the flux correction. For neutron energies > 10 eV, the evaluated flux was used in the calculation of reaction yields. The final systematic uncertainties associated with the shape of the neutron flux were given in Table 3.1.

3.8.2 Saturated resonance normalisation

In principle the calculations of the weighting functions from the simulated detector responses R_d take the absolute detection efficiency of the detectors into account such that the modified efficiencies are identical to the excitation energy. In reality the the absolute efficiency, or the precise normalisation of the simulated responses, is non-trivial to accurately measure or simulate since it depends on the exact position of the detectors with respect to the sample, the precise volume of scintillation liquid in the detectors, and the optical coupling between the active scintillation volume with the photomultiplier tube. Moreover the neutron flux $\phi(E_n)$ in Equation 3.14 refers to the number of neutrons that actually pass through the sample; as discussed in Section 3.2.1 the beam interception factor is the relevant quantity to calculate this flux — despite the extensive studies of the n_TOF flux and beam interception factor made via simulations and measurements, the most robust method for absolute normalisation is
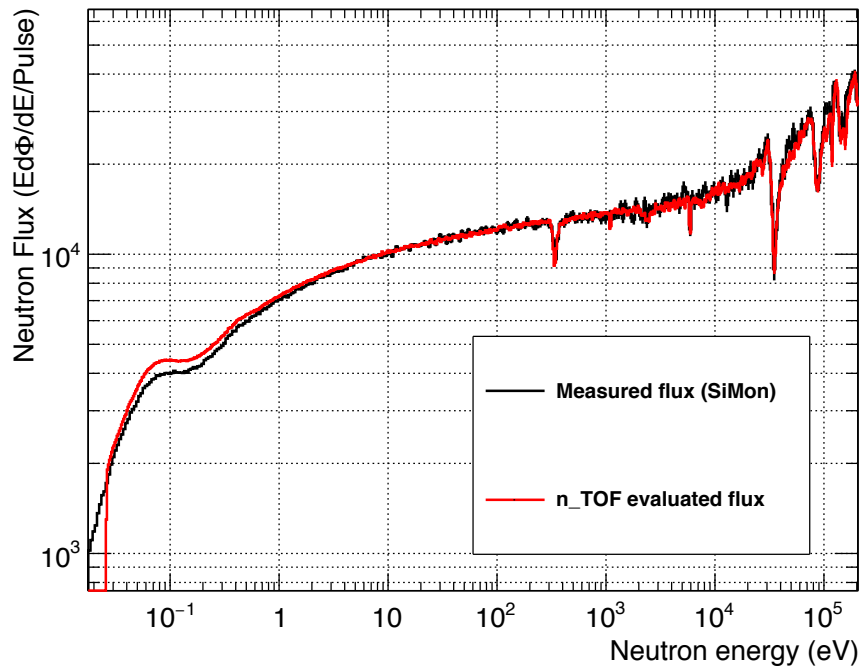
FIGURE 3.35: Neutron flux as measured using the SiMon detectors as discussed in the text, normalised to the the evaluated flux, also shown, over the region 50 eV to 1 keV. The difference at the lowest neutron energies is explained in the text. The sharp decrease of the evaluated flux around 0.03 eV is artificial, and represents the lower limit of the evaluation.

to measure relative to a sample which has a saturated resonance, and perform a final normalisation of the reaction yield using the *saturated resonance method* (SRM).

Saturated resonances are those for which the cross section is very large, and the scattering width is smaller than the capture width — this may occur for the sample of interest, but where this is not the case, a separate sample is used. The most commonly used sample is ^{197}Au, for which the 4.9 eV resonance has a capture cross section of $\approx 3 \times 10^4$ b, and widths Γ_γ = 121.4 eV and Γ_n = 14.96 eV. In this case, even for a sample with a thickness of ~ 10 μm, all neutrons with energies close to the resonance energy of 4.9 eV passing though the target are absorbed, and the resonance appears 'saturated'; the measured capture yield $Y \approx 1$ since even neutrons that scatter within the sample multiple times are also mostly captured. If a ^{197}Au sample of the same diameter as the sample of interest is measured at the same position in the neutron beam (so that the beam interception factors are the same meaning that the same number of neutrons pass through each sample per neutron bunch), the experimentally measured yield at the plateau of the saturated resonance can be compared to the calculated value, and one can obtain an absolute normalisation that absorbs all of the complications described above. This normalisation factor (f_{Norm} in Equation 3.14) also applies to other samples. This method is robust since the yield at the plateau of

the saturated resonance is almost independent of the precise values of the resonance parameters Γ_γ and Γ_n, as well as the precise thickness of the sample.

The analysis procedures described in the previous sections of this chapter were applied to the Au sample; the weighted counting rates (using the WF specific to the saturated resonance, see Section 3.6.2) and backgrounds are shown in Figure 3.36. The sample dependent background for the Au sample has not been taken into account since the addition of such a background would only contribute <0.1% to the final yield, and is thus negligible. The yield not yet corrected with the saturated resonance normalisation given by

$$Y^{exp}(E_n) = f_{PHWT} \frac{C_w(E_n) - B_w(E_n)}{(S_n + \frac{A}{A+1}E_n)\phi(E_n)} \tag{3.28}$$

is shown in Figure 3.37 for one of the detectors for the energy range of interest. The R-Matrix code SAMMY was used to calculate the theoretical yield $Y^{th}(E_n)$ for the 4.9 eV saturated resonance using resonance parameters from the ENDF-BVIII.0 library (more details of the SAMMY resonance fitting procedure is given in the following section), and fit the experimental data with a function of the form

$$Y^{exp}(E_n) = aY^{th}(E_n) + b. \tag{3.29}$$

The correction factor $f_{Norm} = 1/a$ and b is a constant to take account of any small residual background in the experimental reaction yield. This correction factor is also applicable to the NaCl sample, since it depends only on geometrical factors which are common to both NaCl and Au samples. For the Au sample, a section of the final corrected reaction yield was shown in Figure 3.17, where there is good agreement with the SAMMY calculation. The constants a for the four detectors are shown in Table 3.6:

TABLE 3.6: Saturated resonance normalisation factors and uncertainties for the four detectors, taken from fits such as the one shown in Figure 3.37.

Detector	a	$f_{norm} = 1/a$	Uncertainty (%)
1	0.740	1.351	4.081
2	0.616	1.623	4.205
3	0.627	1.595	5.167
4	0.706	1.416	4.249
Average:	0.677	1.486	2.185

The average value of 0.677 for the constants a agrees well with the beam interception factor at $E_n = 4.9$ eV shown in Figure 3.4, meaning that the absolute efficiency implicit in the Geant4 response simulations used to determine the weighting functions was

indeed accurate. After calculating the average yield by combining the separate yields from each detector, the overall uncertainty relating to the final normalisation was taken to be 2.2%. The other relevant uncertainty is that of the relative beam interception factors for the NaCl and Au samples (assumed to be the same in the application of the SRM): an uncertainty of 2% was estimated, based on an accuracy in the position of the samples of 0.5 mm (discussed in Section 3.3), and the sensitivity of the beam interception factor to misalignments (discussed in Section 3.2.1).
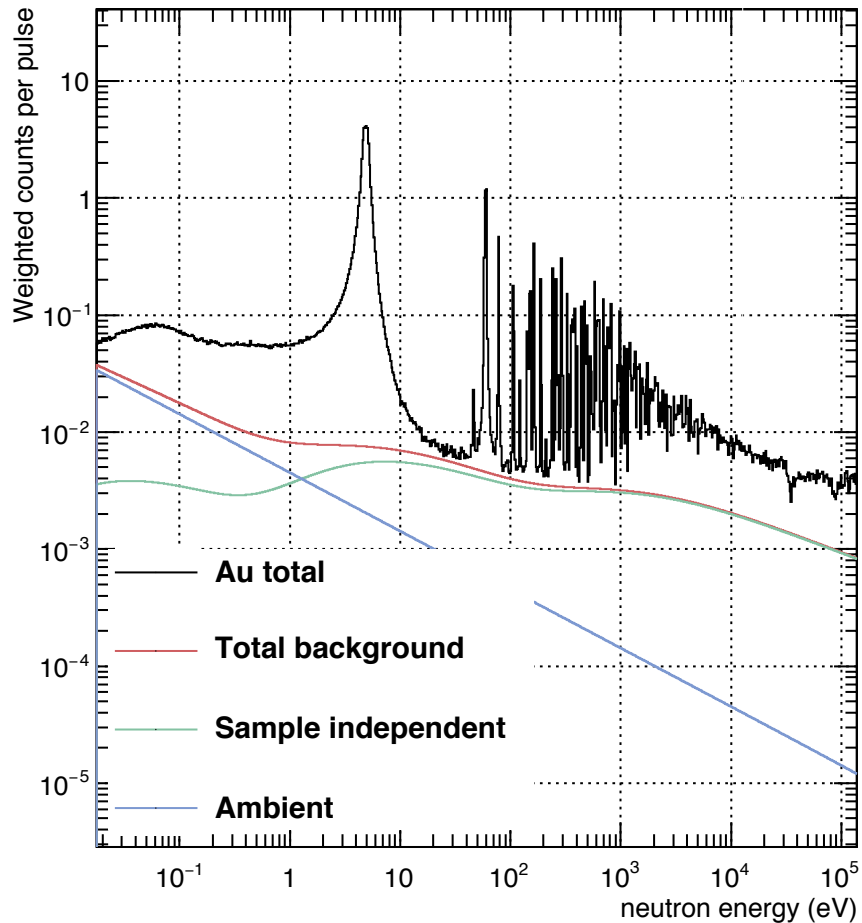
FIGURE 3.36: Weighted counting rates from the Au sample with associated background components used for implementing the saturated resonance method.

3.8.3 Final yield and uncertainties

As previously stated, an independent analysis was performed for each detector and for the dedicated and parasitic beam modes in order to check for the consistency of each of the systematic corrections detailed in previous sections, which was found to be satisfactory; each of the eight independent yields were consistent within statistical errors. The final reaction yield was calculated as the weighted average of these eight
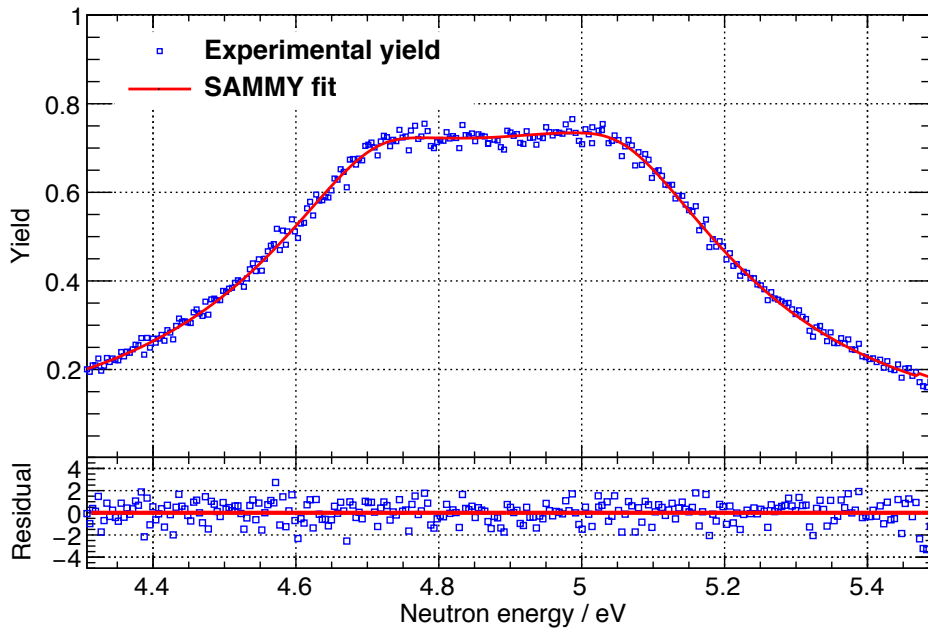
FIGURE 3.37: Au yield for the 4.9 eV saturated resonance prior to normalisation with the saturated resonance method, given by Equation 3.28, for a single detector (detector 1). The residuals are given in units of the statistical error associated with each point.

independent yields, where the weights for each detector were given by the factors a in Table 3.6 since these effectively represent the overall efficiency of each detectors, and the weights for the combination of the parasitic and dedicated beam modes was the number of protons on target for the respective mode, n_p^{par} and n_p^{ded}. The final yield was calculated as:

$$Y_{n,\gamma}(E_n) = \frac{1}{(n_p^{par} + n_p^{ded})\sum_{i=1}^{i=4} a_i} \sum_{i=1}^{i=4} a_i \left(n_p^{par} Y_i^{par}(E_n) + n_p^{ded} Y_i^{ded}(E_n) \right), \qquad (3.30)$$

where the sum is over the four detectors and $Y_i(E_n)$ are the respective independently determined reaction yields. A summary of the systematic uncertainties associated with the final reaction yield are given in Table 3.7. The total uncertainty is dominated by the flux and beam interception factors. These factors cannot feasibly be improved without modifying the experimental setup, and combined, represent the best case uncertainty.

TABLE 3.7: Systematic uncertainties associated with the ^{35}Cl(n, γ) reaction yield.

Contribution	Uncertainty (%)	see Section ...
Sample areal density	0.5	3.3
Neutron flux shape:		
25 meV to 10 keV	2	3.2.1
10 keV to 1 MeV	4	3.2.1
Efficiency (pulse height weighting technique)	1.5	3.6.2
PHWT correction factors	2	3.6.2
Saturated resonance normalisation	2.2	3.8.2
Beam interception factor (misalignment)	2	3.8.2
Dead-time	*negligible*	3.5.4
Multiple hits	*negligible*	3.5.4
Total uncertainty:		
25 meV to 10 keV	**4.4%**	
10 keV to 300 keV	**5.6%**	

3.9 ^{35}Cl(n, γ) cross section analysis and results

3.9.1 Resonance analysis for $E_n < 100$ keV

As discussed in Section 1.2, the cross section in the resolved resonance region (RRR) can be described by the parametrisation of each of the Breit-Wigner resonances by their partial widths Γ_i, energies E_R and spin-parity J^π. Before the analysis of resonances from the compound reaction channel however, the inevitable small residual background after the background evaluation and subtraction described in Section 3.7 must be checked and if necessary subtracted from the reaction yield. In principle there is also a smoothly varying component from direct neutron capture on both ^{23}Na and ^{35}Cl present in the NaCl sample. This direct capture component is indistinct from resonant capture on an event-by-event basis. For the RRR, the direct component for ^{35}Cl is relatively small as shown in [43], and it is also expected to be the case for ^{23}Na. In the RRR, the R-Matrix software SAMMY used to fit the data deals only with the resonant channel, not the direct component. Therefore the sum of the residual background and possible contribution from direct capture was determined by fitting the valleys between resonances, which provides an independent measure of the background above the theoretically calculated resonant capture yield. As shown below, thirteen resonances were measured from the yield for which the residual background was approximately constant at an average level of -7.9×10^{-6} — i.e. the background was over-subtracted by a small amount; the total counting rate including each of the background components and from the NaCl sample itself has therefore been accounted for to within an accuracy of ~ 1 neutron in 10^5. This level of background is negligible in practice, but was nevertheless subtracted before performing the resonance analysis.

The resonance analysis fits obtained using SAMMY are shown in Figures 3.38, 3.39 and 3.40. Each of the effects discussed in Section 3.2.2 are included in the fitting procedure. For the plots which show groups of resonances, the resonances were fit simultaneously; the groups of resonances were sufficiently widely spaced that the tails of resonances from one group have a negligible effect on adjacent groups. The initial resonance parameters E_R, Γ_γ, Γ_n and Γ_p (since the ^{35}Cl(n, p) channel is open with a Q-value of $+615$ keV) were taken from the ENDF-BVIII.0 evaluation, as were the spin assignments. For a number of the resonances measured in this work, the proton width represents a significant fraction of the total width; the fitting strategy was therefore to keep the proton width fixed, whilst leaving E_R, Γ_γ and Γ_n as free parameters. The proton widths in the ENDF-BVIII.0 library are those resulting from the evaluation of Sayer *et al.*, in turn based on the consistency of their transmission

and capture data, the $^{35}Cl(n, p)$ data of Druyts *et al.* [76] and the transmission data of Singh *et al.* [77]. For some resonances, manual adjustment of resonance parameters were required in order to obtain satisfactory SAMMY fits, and for two resonances only a single width was varied, again to obtain satisfactory fits. The resonance shapes are dependent on the final spin of the state upon neutron capture - the spin is also in principle a free parameter in the fitting procedure, although as discussed in Section 2.7, the best spin assignments are made by combining capture data with transmission datasets. The ground state spin-parity of ^{35}Cl is $\frac{3}{2}^+$; the capture of a neutron with orbital angular momentum $\ell = 0$ or 1 (since radiative neutron capture is dominated by *s*- and *p*- waves) gives possible spin-parities of $1^+, 2^+$, or $0^-, 1^-, 2^-, 3^-$ respectively. For this work, the resonances were best described using the existing assignments (both firm and tentative) in the evaluation of Guber *et al.* made on the basis of detailed shape and area analysis of both capture and transmission data. Indeed 7 of the 13 measured resonances have tentative spin assignments (14.8 keV, 16.3 keV, 22.3 keV, 27.2 keV, 44.0 keV, 51.4 keV, 52.7 keV, 57.6 keV); the statistics gathered in this single measurement of the capture reaction channel are not a sufficient basis to contribute to the multi-channel analysis already performed by Sayer *et al.* especially since 6 of the 7 ambiguous assignments are associated with resonances with poor statistics. Since the experimental yield also by definition contained components from the other contents of the sample (^{23}Na and a small amount of ^{37}Cl), these components were also included in the SAMMY fitting procedure; although the resonances from these contaminants are not the subject of this work, they are important to include in the fitting procedure since the multiple scattering (potential scattering of neutrons one or more times before being captured) depends strongly on all isotopes present in the sample, and their respective scattering cross sections and densities — the resonance parameters for these contaminants were taken from ENDF-BVIII.0. Only at the first resonance at around 397 eV were the reaction yield statistics sufficient to observe the multiple scattering component present as the tail to higher neutron energies shown in the top of Figure 3.38, described well by SAMMY; the tail is present at higher energies of the resonance centroid since neutrons of higher energy lose energy when they scatter to a value that matches the resonance energy (neutrons of lower energy do not gain energy when they scatter). For all measured resonances though, the multiple scattering contribution was on the order of 1% or less and therefore any systematic uncertainty associated with the modelling of multiple scattering in SAMMY can be safely neglected.

As already discussed the number of resonances measured in this work was greatly hindered by the background. In the two previous measurements, those of Guber *et al.* and Macklin *et al.*, many more resonances were measured: 54 in the older Macklin

measurement, and 217 in the more recent Guber measurement. For a comparison of the quality of the n_TOF data with respect to the previous measurements, spectra from previous experiments are shown in Figure 3.41; data is shown for the entire measured energy range for the Macklin measurement, and a subset of the energy interval covered by the Guber measurement is shown.

Both of these measurements were made at the ORELA facility at Oak Ridge National Laboratory. There are a number of reasons why these previous measurements measured many more resonances. Firstly, the statistics gathered for the measurement in this work are poorer than for either of the two previous measurements; this is in part related to beam-time, and partly related to the areal density of the sample used for this work. As mentioned in Section 3.3, there was an issue with contamination of the sample during its manufacture, which meant that a significant amount of material was lost resulting in a thinner sample (indeed, the multiple scattering effects were almost negligible with the target used in this work, affording the possibility of a thicker sample). Secondly, both previous measurements used natural LiCl samples; compared to Na (present in the NaCl sample), Li has a more favourable scattering cross section (on average around 5× less over the RRR). This results in a reduced sample dependent background, and is hence less prohibitive when measuring weaker resonances. Finally, since the background in this work was dominated by the sample independent background, it is clear that ORELA at ORNL is simply more suited to measurements of light nuclei. Indeed prior to the Guber measurement [43], the ORELA capture set-up had been optimised by further reducing the structural material surrounding the detection system, further increasing its suitability for capture measurements of light isotopes with small cross sections.

As discussed in Section 2.7, in any single neutron capture experiment, it is only the resonance kernel $\kappa = g\Gamma_n\Gamma_\gamma/\Gamma$ (proportional to the resonance area) that can be independently evaluated without using the results of transmission experiments which would yield the total reaction cross section, due to the strong correlation between the partial widths associated with each resonance. The experimental kernels are given in Table 3.8, where the values from evaluated data libraries are also shown for reference; a more complete comparison is given below. For reference, the individual best fit resonance parameters are given in Appendix B.

TABLE 3.8: Resonance kernels (κ) for ^{35}Cl+n calculated from the results of the R-Matrix analysis with SAMMY for the n_TOF alongside those from evaluations for reference. The kernel uncertainties relate to the point-wise statistical errors in the reaction yield. The resonance energies E_R are those determined from the n_TOF data. (A comparison of the resonance energies and partial resonance widths and spins are given in Appendix B).

	n_TOF		ENDF B-VIII.0 (and JEFF 3.3)	JENDL-4.0
E_R (eV)	κ (meV)	Unc. κ (meV)	κ (meV)	κ (meV)
397.36	22.98	0.43	20.23	32.68
4243.56	88.63	10.27	83.58	99.01
14758.68	226.44	14.83	213.60	253.50
16312.30	363.30	15.47	309.69	519.46
17088.01	814.90	25.81	662.77	1184.03
22327.11	86.69	60.79	77.42	55.56
26526.64	154.23	24.16	189.59	236.79
27262.17	298.95	33.22	260.09	295.02
43995.36	409.10	89.45	378.18	450.21
51400.88	82.09	30.94	36.97	86.89
52757.27	256.93	61.02	208.08	229.23
54705.00	152.20	76.44	136.64	168.25
57585.17	341.44	72.45	331.55	398.32
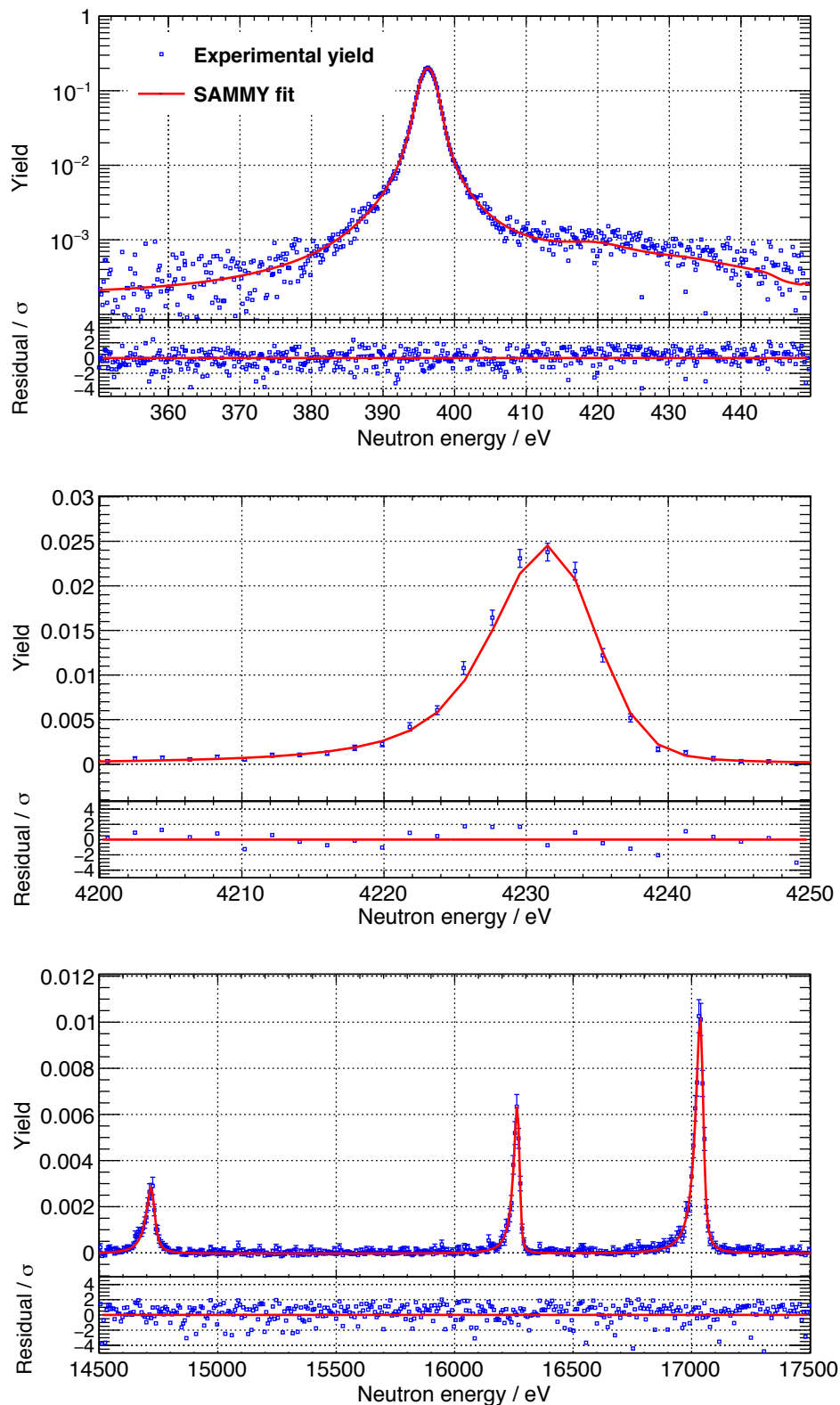
FIGURE 3.38: Fits to the final ^{35}Cl(n, γ) experimental reaction yield with SAMMY. The error bars pertain only to the statistics, not to the systematic uncertainties given in Table 3.7 (this is also the case for the subsequent similar plots). The correction due to the experimental effects, such as the thick sample multiple scattering correction for the 397 eV resonance in Cl, are included by the code SAMMY.
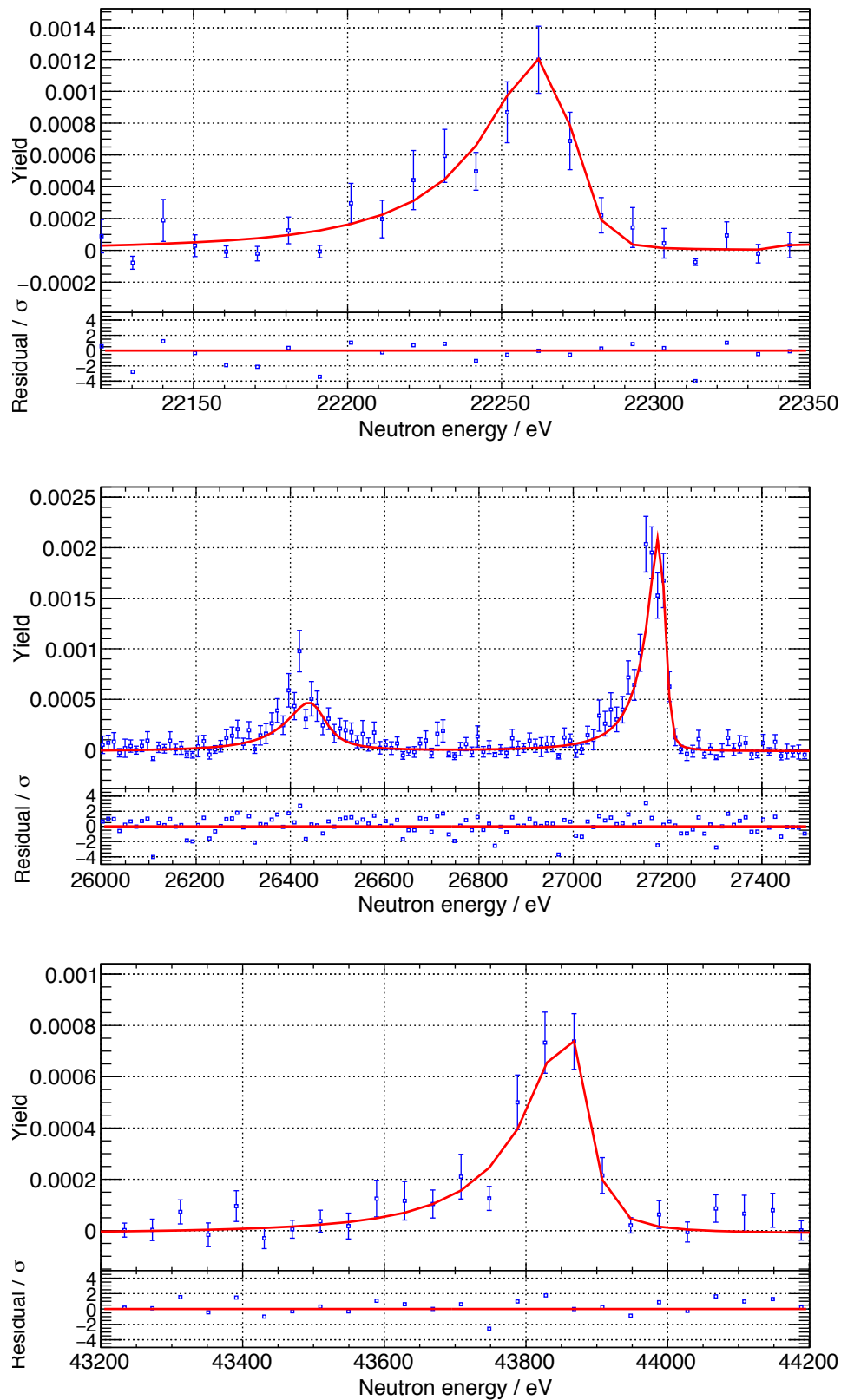
FIGURE 3.39: Fits to the final ^{35}Cl(n,γ) experimental reaction yield with SAMMY.
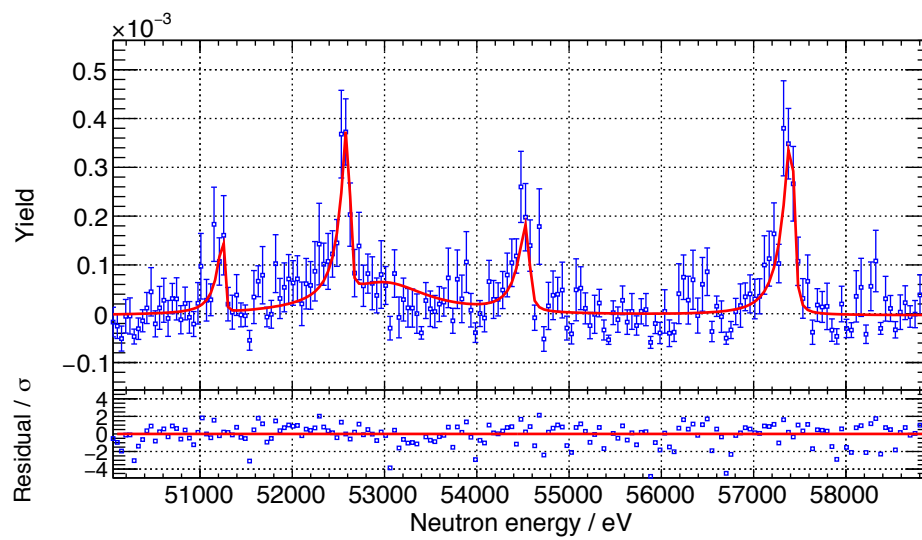
FIGURE 3.40: Fits to the final ^{35}Cl(n, γ) experimental reaction yield with SAMMY.
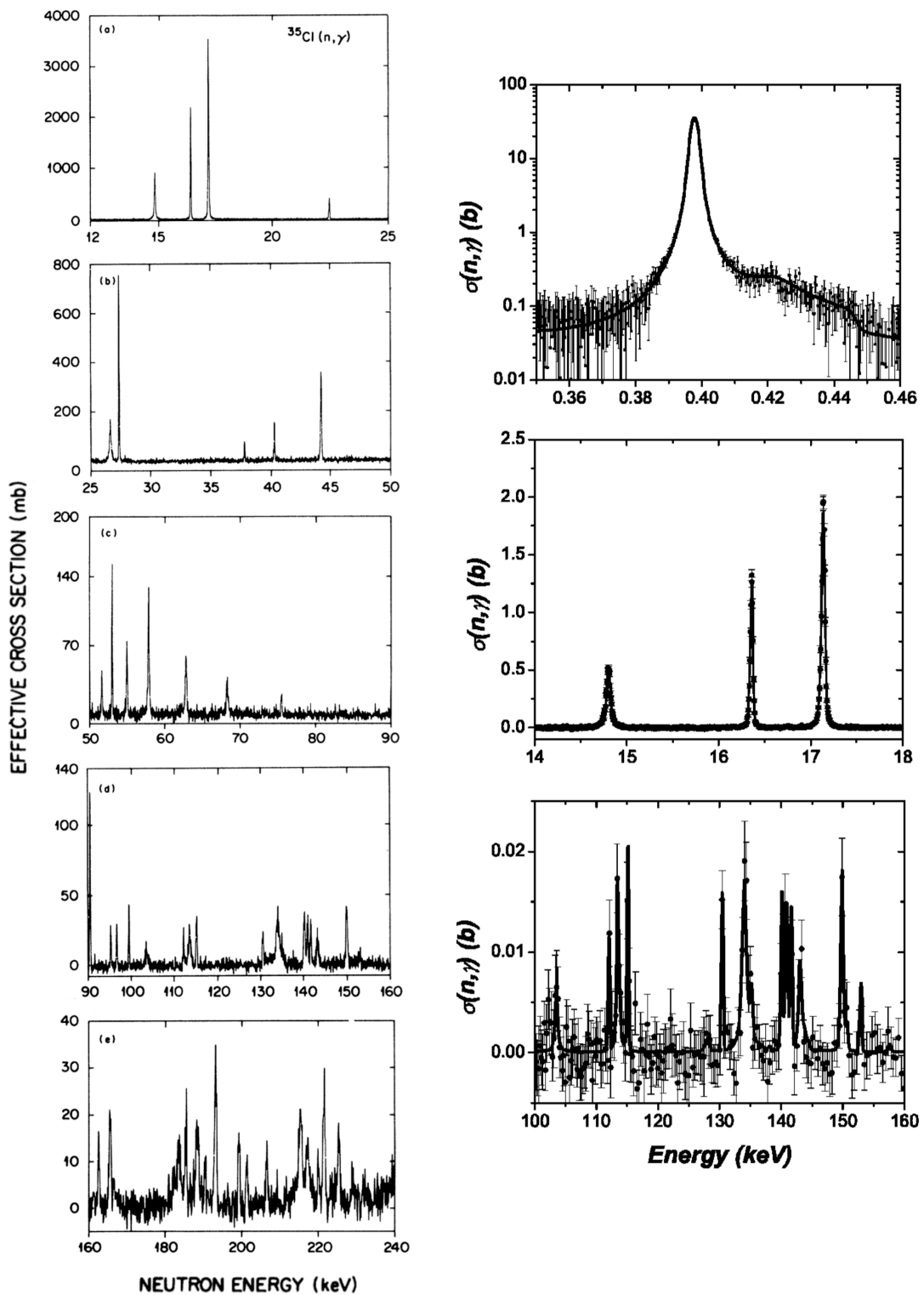
FIGURE 3.41: Samples of the capture data from the two existing experimental datasets; those of Macklin *et al.* (shown in the left column, figures reproduced from Reference [42]) and Guber *et al.* (shown in the right column, figures reproduced from Reference [43]). Both measurements were made using LiCl samples, the advantages of which are discussed in the main text.

3.10   Discussion of results

The resonance kernels given in Table 3.8 are explicitly compared to those from the different evaluations in Figure 3.42, where the ratios between the respective quantities are shown for each measured resonance. The ratio uncertainties pertain to the errors associated with the calculation of the kernels from the SAMMY fits to the reaction yield (the systematic yield uncertainty is not included). The comparison of the experimental results to JEFF-3.3 is not shown since the JEFF-3.3 evaluation is identical to that of ENDF B-VIII.0; they are both based on the evaluation performed by Sayer *et al.* [44], also shown. The experimental results are also compared to the only previous measurement for which the resonance parameters are explicitly reported, that of Macklin *et al*. The weighted average of the ratios shown in Figure 3.42 are given in Table 3.9. It is evident that for the ENDF and JEFF evaluations (and hence the Sayer evaluation) that the kernels are consistently underestimated with respect to the n_TOF results by 15.0(2)%; even when the systematic uncertainties associated with the overall normalisation of the reaction yield are considered (around 5%), the average difference between the results of this work and the ENDF evaluation are still inconsistent. Conversely, the JENDL evaluation in general overestimates the kernels. The results of Macklin *et al.* are in better agreement with the n_TOF results than is the case for any evaluation; the average kernel ratio with respect to the Macklin measurement is indeed consistent unity, which therefore resolves the inconsistency between the two previously existing measurements. Assuming that the 15% difference of our kernels with respect to the ENDF/JEFF evaluations would also apply to other resonances if they had been seen above the background, then the n_TOF results imply that the total cross section is on average around 15% higher than is the case in the ENDF/JEFF evaluations used by industry. It is envisaged that a re-evaluation of the cross section will therefore have a sizeable impact on applications — this impact is quantified in Section 3.11. It should also be noted that no new resonances were found, and the resonance energies found in this work are within 0.1% of those given in previous measurements and evaluations, as expected.

A final check on the resonance analysis was performed to confirm that there was no systematic effect on the shapes of the measured resonances due to prompt neutron scattering (neutron sensitivity), the effect of which was discussed in Section 3.2.1 where it was shown that for this measurement the prompt interactions generated due to resonant neutron scattering should have a negligible effect on the measured shapes of the resonances. The kernel ratios with respect to the ENDF evaluation are shown in Figure 3.43 as a function of the ratio Γ_n/Γ_γ. If in fact neutron scattering was having a significant effect on the measured resonances, one would expect that
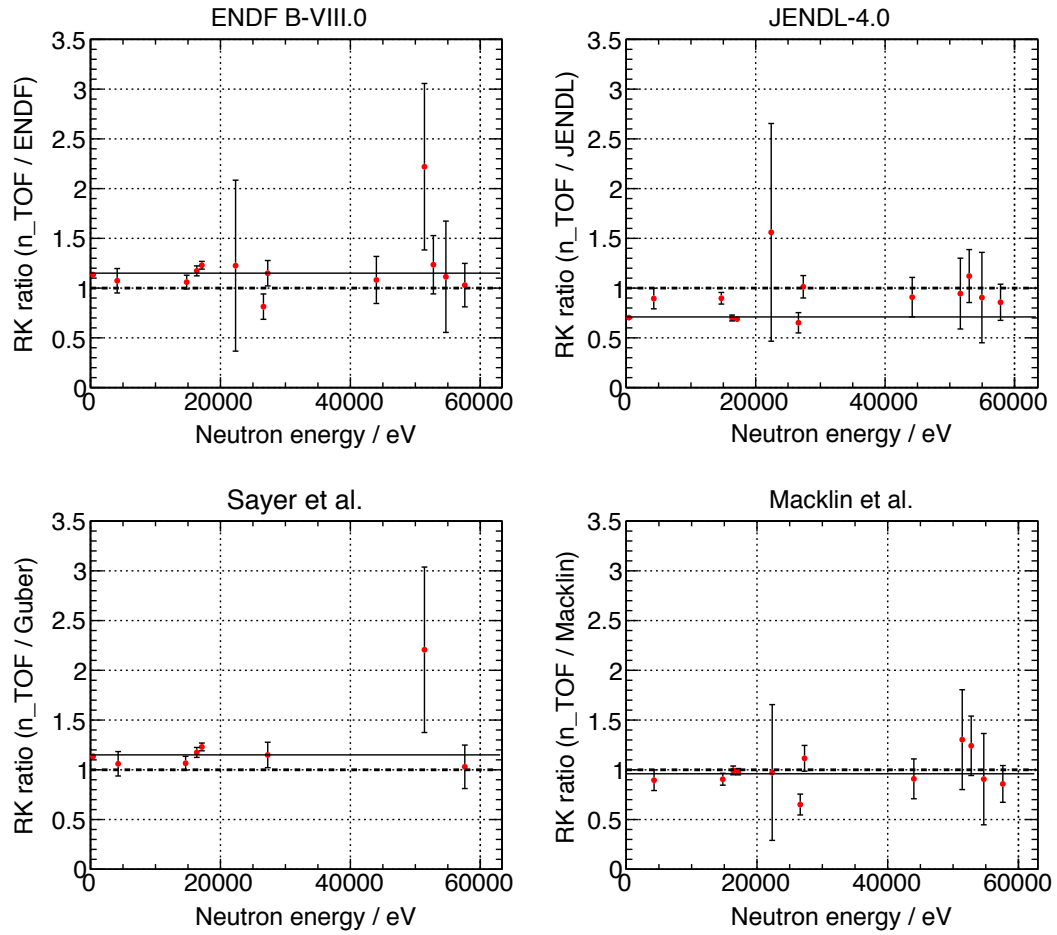
FIGURE 3.42: Comparison of measured resonance kernels (RK) to those of evaluated data libraries and previous measurements, see text for further discussion. The solid horizontal lines indicate the (weighted) average ratio, given numerically in Table 3.9. The individual kernels and statistical uncertainties were given in Table 3.8.

TABLE 3.9: Average difference between experimental resonance kernels and those from previous measurements and evaluated data libraries (for the measured resonances).

Reference	Average $\kappa_{n\_TOF}/\kappa_{Ref.}$
Evaluations:	
ENDF B-VIII.0	1.15(2)
JEFF-3.3	1.15(2)
JENDL-4.0	0.71(2)
Measurements:	
Sayer & Guber [43]	1.15(2)
Macklin [42]	0.96(2)

for resonances with a larger Γ_n/Γ_γ, there would be an increased proportion of the resonance strength coming from the prompt neutron interactions with respect to the true capture resonance strength, leading to an upwards trend in Figure 3.43. Indeed the only trend, if any, is of the opposite sense, perhaps indicating that the kernels

from the ENDF evaluation (based on only two previous measurements at the same facility) suffered from the effect of neutron sensitivity, although this conclusion is not clear. The lack of an upwards trend confirms, as expected, that the neutron sensitivity was indeed negligible for the resonances measured in this work.
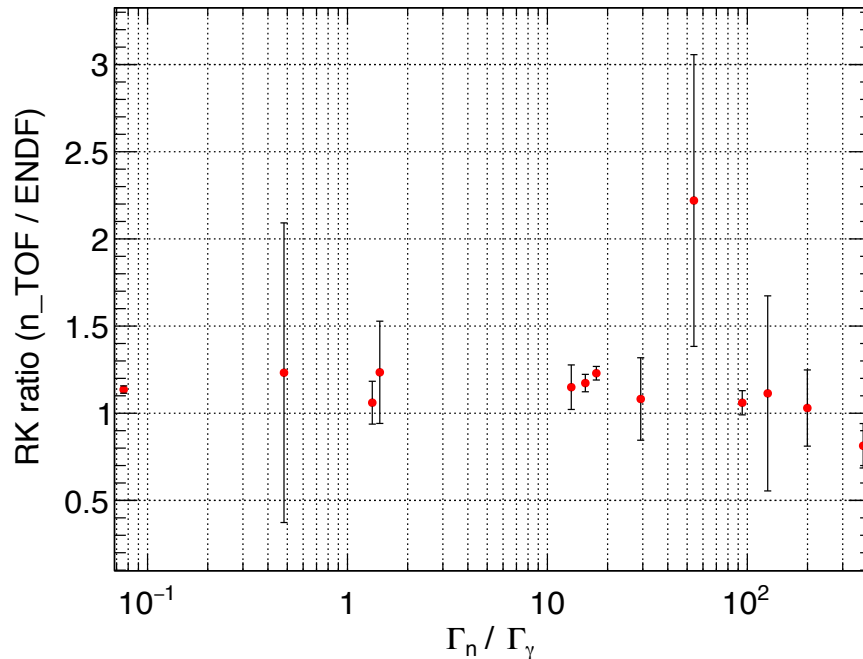
FIGURE 3.43: Ratio of the measured capture kernels to the ENDF B-VIII.0 values as a function of the relative neutron and capture widths to assess the potential impact of the prompt neutron scattering background on the resonance analysis — see text.

3.10.1 Thermal cross section

The thermal cross section $\sigma_{n,\gamma}(E_{th})$ is best evaluated using the resonance parameters, given by the sum of the tails of the Breit-Wigner resonances extrapolated to thermal energy. Although in principle the thermal cross section could be deduced from the reaction yield directly, this is complicated since the total neutron reaction cross section is on the order of tens of barn, as is the capture cross section; the yield given by Equation 2.2 is therefore on the order of 0.1, meaning that the thin target approximation does not apply. A Monte-Carlo simulation would be required to correct for the self-shielding and multiple scattering effects which in turn depend on a priori knowledge the total neutron cross sections of both ^{35}Cl and ^{23}Na. The direct measurement of the thermal cross section from the yield is further complicated since the beam interception factor varies by a significant amount for low neutron energies, depending on the precise position of the target in the beam as shown in Figure 3.4, introducing a further source of systematic uncertainty to the measurement. Deducing

the cross section using the resonance parameters is independent of these corrections, and is furthermore a robust way of assessing the consistency of the resonance analysis with the previous dedicated thermal measurements in the literature as well as the evaluated values. The thermal cross section was calculated from the resonance parameters using SAMMY, and is given by the following expression which in turn follows from Equation 1.6:

$$\sigma_{n,\gamma}(E_{th}) = \sum_i g_i \frac{\pi}{k_n^2(E_{th})} \frac{\Gamma_{n,i}\Gamma_{\gamma,i}}{(E_{th} - E_{R,i})^2 + \Gamma_i^2/4} + \sigma_{n,\gamma}^{Direct}(E_{th}), \qquad (3.31)$$

where the sum is over all resonances and gives the total resonant channel component, and $\sigma_{n,\gamma}^{Direct}(E_{th})$ is the direct capture component, also varying as $\sim 1/v$, which can be significant in comparison to the resonant component for low energies — the direct component was taken from [43], and is given in Table 3.10. The experimental resonance parameters for the 13 measured resonances were included in the sum; the missing resonances, the 259 (weaker) resonances present in the ENDF B-VIII.0 evaluation not measured due to the prohibitive background, were included using the parameters from ENDF-BVIII.0. Their contribution to the cross section was scaled based on the results of the measured resonances: since the measured resonance kernels (proportional to the area and hence magnitude of the cross section) were consistently larger than those tabulated in ENDF by 15%, as per Table 3.9, the contribution from the missing resonances to the thermal cross section was also increased by the same factor. Because the number of resonances not measured in the n_TOF data greatly outnumbers the measured resonances, the thermal cross section deduced in this way is not a direct measurement, but a means of testing the consistency between the result that the cross section is increased across the whole neutron energy range, with the previous dedicated thermal measurement. The evaluated thermal cross section from the ENDF, JEFF and JENDL data libraries (which all adopt the same value) is shown in Table 3.10, as is the single previous direct activation measurement of the thermal cross section [78]. The values for the direct and resonant components of the thermal cross section determined using the sum detailed above are also shown, as well as their sum, shown as the 'total' value: as a benchmark, the thermal cross section was calculated directly from the ENDF parameters without scaling the contributions from any resonances, giving a result consistent with the evaluated thermal value, as expected. The result using the measured n_TOF parameters and the scaled ENDF parameters is naturally larger than the evaluated value, and interestingly even further from the activation measurement than the evaluated values. Clearly this approach is not the most accurate; the most accurate thermal measurements come from dedicated measurements such as the ^{13}C measurement in this work where the

systematic uncertainties are much smaller (see Chapter 4). A dedicated activation measurement is envisaged — in addition to complementing the n_TOF data, there is a strong motivation for a dedicated thermal measurement since there is only one such measurement in the literature. The measurement will likely comprise of sample irradiation at ILL and subsequent AMS measurement at the Dresden AMS facility (DREAMS); indeed there has been a previous ^{35}Cl measurement at the DREAMS facility dedicated to astrophysics demonstrating the suitability of the facility for a thermal measurement.

TABLE 3.10: Summary of evaluated and experimentally derived values for the thermal cross section — see text for a full discussion.

	Cross section at E_n = 25.3 meV (barn)
Previous thermal measurement:	
Activation measurement, Sims *et al.* [78]	41.8(12)
Evaluations (inc. direct capture):	
ENDF B-VIII.0 (= JEFF-3.3 = JENDL-4.0)	43.6(4)
From resonance parameters (ENDF):	
Resonant component	43.40
Direct capture component [43]	1.58(48)
Total	44.98(48)
From n_TOF experimental parameters + scaled ENDF component	
Resonant component	49.7(24)
Direct capture component [43]	1.58(48)
Total	51.3(25)

3.10.2 Averaged cross section

One of the objectives of this work was a measurement of the averaged cross section in the energy range where a resonance analysis is not possible due to either insufficient statistics, large background level or resonances becoming unresolved (spacings closer than their widths). Figure 3.44 shows the capture cross section associated with the NaCl target, deduced via the thin target approximation ($Y = n\sigma$) — since for this work a NaCl sample was measured, it is the sum of the ^{23}Na and ^{35}Cl cross sections that are determined when averaged over wide energy bins. The measured cross section is compared to that determined from the ENDF B-VIII.0 library, but where the Cl component has been scaled by the 15% discussed previously. In general the measured cross section is in reasonable agreement with ENDF, especially for the regions associated with better statistics where the cross section is largest (where individual resonances have been studied). The high energy tail present at the large

^{23}Na resonance at 2 keV is associated with multiple scattering. For the regions where the averaged cross section is small ($\sim 10^{-2}$ b), the respective reaction yield is around 10^{-5}. As was already discussed, the *residual* background yield discussed in Section 3.9.1 was $\sim 10^{-6}$ and the total background yield between $E_n = 10^4$ and 10^5 eV was around $\approx 10^{-4}$ on average; this explains the differences between the measured and evaluated cross sections in these regions: any small systematic error associated with the background subtraction is large compared to the remaining capture counts. It is for this reason that no meaningful cross section measurement can be made in this energy range.
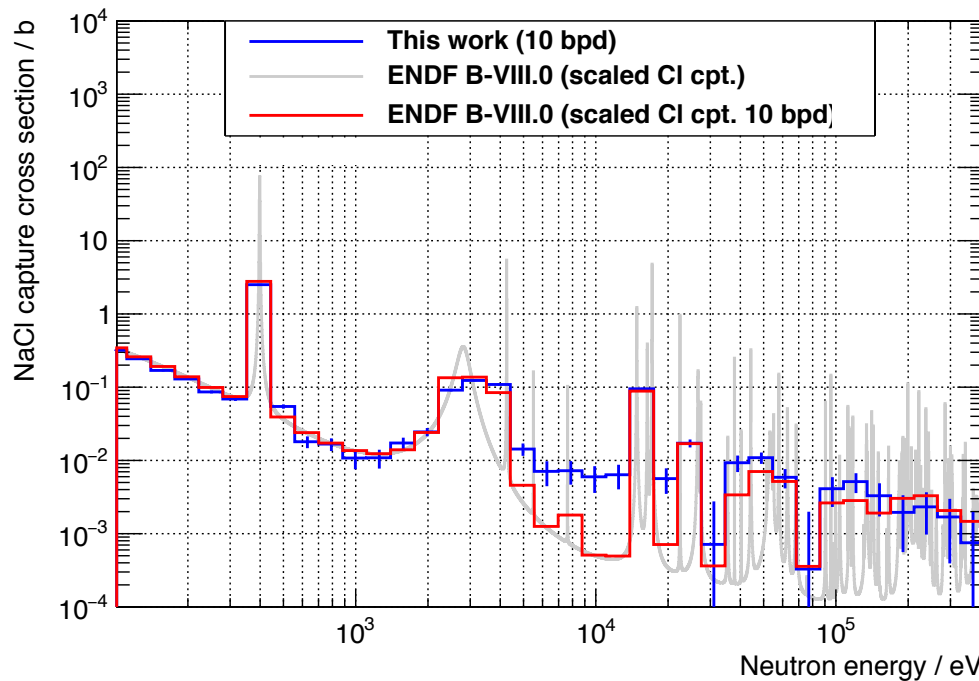
FIGURE 3.44: Comparison of measured and evaluated ^{23}Na^{35}Cl capture cross section. The ENDF B-VIII.0 Cl component has been scaled by the factor of 1.15 discussed previously. Note that the effects of multiple scattering and self shielding have not been corrected here. The error bars relate to the statistical errors.

3.11 Implications of the n_TOF results

An assessment of the implications of the n_TOF data on the three main applications discussed in Section 3.1 is given below. As was the case when evaluating the thermal cross section in the previous section, the total cross section has been constructed by SAMMY using the directly measured resonance parameters, and the ENDF B-VIII.0 parameters for the unmeasured resonances, and where the ENDF component is scaled by 15% to match the findings of consistently larger resonance kernels in the n_TOF data.

Astrophysics

The astrophysical application is concerned with stellar averaged reaction rates which are used as input to asymptotic giant branch stellar models which aim to describe the synthesis of the elements via the astrophysical s-process [39, 40]. The nuclei in stellar interiors are considered to be in thermodynamic equilibrium, and are hence described by a Maxwell-Boltzmann (MB) distribution associated with a particular temperature $k_B T$. The stellar neutron capture rate, key to the calculations of the abundances of elements, is given by

$$\langle \sigma_{n,\gamma} v \rangle_{k_B T} = \int_0^\infty \sigma_{n,\gamma} v f(v, k_B T) dE, \qquad (3.32)$$

where v is the neutron velocity and $f(v, k_B T)$ corresponds to a MB velocity distribution associated with a particular stellar temperature $k_B T$. The *Maxwellian averaged cross section* (MACS) is given by

$$\text{MACS} = \frac{\langle \sigma_{n,\gamma} v \rangle_{k_B T}}{v_T} = \frac{2}{\sqrt{\pi}} \frac{1}{(k_B T)^2} \int_0^\infty \sigma_{n,\gamma}(E_n) E_n e^{-\frac{E_n}{k_B T}} dE_n, \qquad (3.33)$$

where $v_T = 2k_B T / \mu$ with μ as the reduced mass of the neutron-nucleus system. The integration in Equation 3.33 was performed numerically for multiple $k_B T$ values, using the capture cross section generated using SAMMY. The integration was performed in the centre-of-mass where $E_n^{CM} = E_n A/(A+1)$. The direct capture component was also taken into account, using the calculation from Reference [43]. The results of the MACS calculation for different stellar temperatures are shown in Figure 3.45; the contribution to the total MACS is dominated by the 13 measured resonances as would be expected since by definition these were the 13 strongest resonances — at $k_B T = 30$ keV, the measured resonances comprise around 82% of the total MACS meaning that our result is not strongly dependent on the many resonances not measured in this experiment.

In principle there is a finite contribution to the MACS from the unresolved resonance region — in practice since for ^{35}Cl the resolved resonance region extends to around 1.5 MeV, this contribution is negligible, contributing < 0.1% to the MACS at 100 keV, and is smaller for smaller temperatures. At 30 keV the direct capture component is around 3% of the total MACS, and the 29% uncertainty associated with its magnitude is therefore negligible.
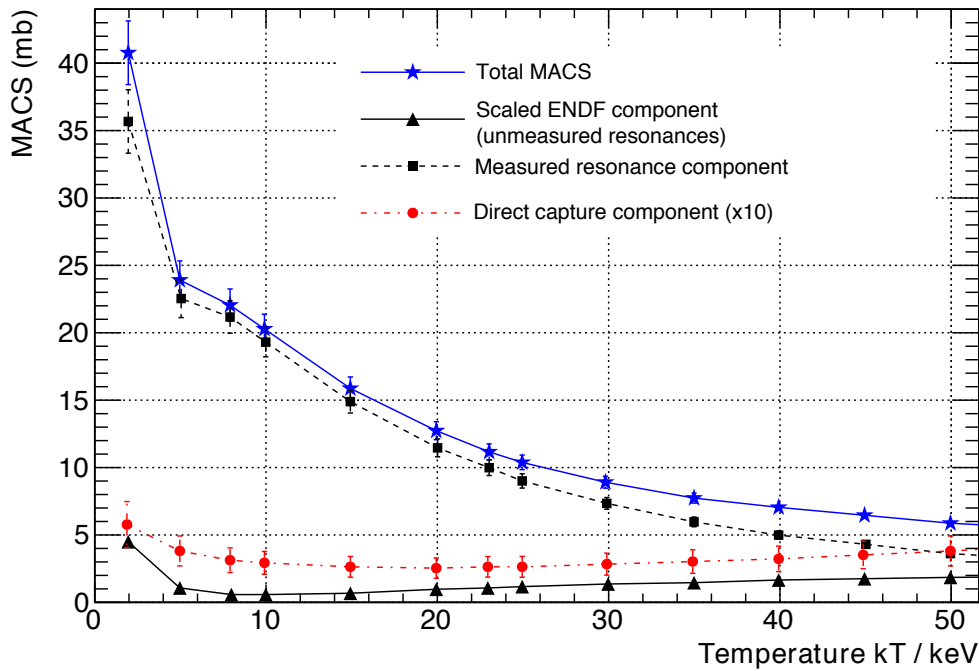
FIGURE 3.45: Maxwellian averaged cross section, and contributing components as a function of stellar temperature.

The existing MACS at 30 keV derived from experimental data, theoretical calculations and evaluations are summarised in Table 3.11: in general the value from this work is larger than those derived from the major nuclear data libraries ENDF/JEFF/JENDL, and less than the previous time-of-flight measurements and the value from the KADo-NiS compilation[8] (based on a single previous measurement, Guber *et al.*). Moreover, our results strengthen the general finding that the theoretical calculations (based on Hauser-Feshbach calculations) consistently overestimate the MACS with respect to the previous measurements; this may not be surprising since these calculations rely on statistical models of the properties of nuclear levels which in general are less applicable to lighter nuclei where the level density is low.

The 30 keV MACS reported in the two previous time-of-flight measurements (Macklin and Guber) are in fair agreement, and are consistent to within the reported uncertainties; the 30 keV MACS measured via neutron irradiation and AMS (Pavetich *et*

---

[8]Karlsruhe Astrophysical Database of Nucleosynthesis in Stars — KADoNiS is an online database for cross sections relevant to the astrophysical s- and p-processes [79].

TABLE 3.11: Summary of MACS values at $kT = 30$ keV including theoretical, evaluated and experimental values. The experimental values deduced from time-of-flight and AMS experiments are denoted 'TOF' and 'AMS' respectively.

Reference	MACS at $kT = 30$ keV (mb)
Theoretical calculations:	
Woosley *et al.* [80]	11
Rauscher *et al.* [81] (NON-SMOKER code)	15.9
Goriely [82] (MOST(2005) code)	51.5
Compiled data:	
KADoNiS-v1.0 [79]	9.39(29)
From evaluations:	
ENDF B-VIII.0 / JEFF-3.3	7.63
JENDL-4.0	8.54
Direct capture component:	
Guber *et al.* [43]	0.271(80)
Experimental values:	
Macklin (TOF) [42]	10.0(3)
Guber *et al.* (TOF) [43]	9.39(29)
Pavetich *et al.* (AMS) [45]	8.33(32)
This work (TOF)	8.70(45)

al.) is however significantly lower than the MACS associated with the time-of-flight measurements, an as yet unexplained difference more generally observed for AMS MACS measurements of other nuclei (e.g. [83–85]). It is encouraging that the MACS associated with time-of-flight measurement presented in this work is more in line with the AMS measurement, although the relatively large uncertainty means that it is also statistically consistent with the Guber time-of-flight measurement. Interestingly, despite the finding that the resonance kernels found in this work are reasonably consistent with those of the Macklin measurement (see Figure 3.42), the MACS are quite different. It is not clear what the cause of this deviation is, or indeed how the MACS was calculated in the Macklin measurement. For this older measurement it was reported that there were issues with the neutron sensitivity of the detection set-up, and the associated corrections; if the MACS was calculated simply by deducing the cross section from the measured yield (rather than constructing it from the resonance parameters) it may be that the contribution to the capture yield from neutron scattering (the neutron sensitivity) may have not been fully accounted for, leading to a larger MACS. As expected the resonant contribution to the MACS in this work is around 15% larger than that from ENDF. It is important to note that the previous AMS measurement gave a result around 10% larger than the ENDF value; AMS is an independent technique with different sources of systematic uncertainty, which

in general are smaller than those associated with time-of-flight measurements. Our results confirm the finding that ENDF B-VIII.0 underestimates the cross section across the whole resolved resonance region by a factor on the order of 10%.

Since the MACS derived from the measurement in this work is consistent with the AMS measurement, the implications of the results of this work should be expected to be similar to that of the AMS measurement, detailed in Reference [45]. In summary it was found that relative to the results derived adopting the MACS data from KADoNiS, for massive and thermally pulsing asymptotic giant branch (TP-AGB) stars [86], the extent to which ^{35}Cl acts as a neutron poison is changed by < 0.1%. The abundance of ^{35}Cl is increased by around 10% which in turn leads to small differences in the abundances of ^{36}Cl and ^{36}S of around 1% and 2% in TP-AGB and massive stars respectively — further details can be found in Reference [45] and the references therein.

Reactor physics

The production of ^{36}Cl in irradiated nuclear graphite by neutron capture on ^{35}Cl (present at the level of around 2ppm) is the application of this measurement in the context of reactor physics. In general the approach taken when planning for the safe disposal of a large amount of irradiated material, such as irradiated nuclear graphite from graphite moderated reactors, is to combine knowledge of the abundance of nuclides present in the material with reaction cross section data in order to simulate the history of a given reactor to produce an estimate of the amount of the activation product — this avoids expensive destructive analysis. Such a study was performed in relation to nuclear graphite in Reference [37]. For the purposes of this work, a rough study assessing the sensitivity of the production rate of ^{36}Cl via neutron capture with respect to the reaction cross section has been performed [87] in which the energy dependence of the neutron flux in the Oldbury MAGNOX reactor [34] has been combined with cross section data taken from the JEFF-2.2 nuclear data library[9]. The results, shown in Table 3.12, indicate that neutron capture in the resonance region accounts for around 4% of the total neutron capture rate; this implies that by changing the current ENDF BVIII.0 or JEFF-3.3 evaluated cross section by 15% (as discussed previously) that the capture rate will change by around 0.5%, a modest change, as expected in a thermal reactor. Although the change is small however, the uncertainties on the resonance parameters in a future evaluation should be reduced which will in turn lead to a reduction in the final uncertainty on the amount of the activation product ^{36}Cl. The thermal value derived from the measurement in this work is

---

[9]JEFF-2.2 is the standard (validated) library currently used for most industrial calculations in Europe, including those associated with MAGNOX reactors.

based on the measured resonance parameters, and is around 18% larger than the evaluated value (see Table 3.10). This would therefore lead to an increase of $\approx$14% to the ^{36}Cl production for the case of a MAGNOX reactor. As was discussed in Section 3.10.1 however, the most accurate thermal measurements are those from dedicated measurements and as such no clear conclusion can be drawn from this work about the implications for the thermal capture component.

TABLE 3.12: Results of the simulation of the production rates of ^{36}Cl in the Oldbury MAGNOX reactor from the $^{35}Cl(n, \gamma)$ reaction, and the contribution to the total production rate from different neutron energy ranges: fast ($\sim$ MeV energies and above), the resolved resonance region, and thermal region.

Energy region	Cross section integral (arb)	Flux (arb)	Reaction rate (arb)	Contribution to total rate (%)
Fast	0.006	0.199	0.001	0.010
Resonance region	1.624	0.304	0.493	3.836
Thermal	24.872	0.497	12.361	96.154

Medical physics

A Monte-Carlo simulation has been performed with MCNP [68] in order to assess the impact of our results on the dose rates to healthy tissue associated with boron neutron capture therapy, in the specific case of brain tumour therapy [88]. The 'Snyder head phantom model' [89] as a model for brain tumour treatment has been adopted in which a 'generic epithermal neutron beam' with an energy spread similar to that of those proposed for future clinical trials has been implemented (see Reference [89] for details). The simulated dose rate delivered to brain tissue as a function of depth is shown in Figure 3.46, where the total dose rate includes the dose from all constituents of the brain composition, not just that from $^{35}Cl(n, \gamma)$. The reference dose rate is calculated using reaction cross sections from the ENDF B-VI library (these are the cross sections used as standard in the Monte-Carlo code MCNPX v2.5 [90] and the results serve as reference calculations in the literature). This benchmark calculation is compared to similar simulations but assuming the cross sections from ENDF B-VIII.0, and a further comparison assuming the finding that the $^{35}Cl(n, \gamma)$ cross section is 15% larger than that reported in ENDF B-VIII.0, as found in this work. The impact of the n_TOF results are modest, indicating an increase of around 1.5-1.8% in the total dose rate, where the $^{35}Cl(n, \gamma)$ reaction is responsible for around 10-11% of the total dose; the uncertainty on a future evaluation is however likely to decrease, leading to a decreased dose rate uncertainty. Once again, this result has assumed that the thermal value is also scaled up based on the resonance analysis, and a dedicated thermal measurement would be required to complement the n_TOF resonance analysis to

draw accurate conclusions about the effect of the cross section in this low neutron energy region.
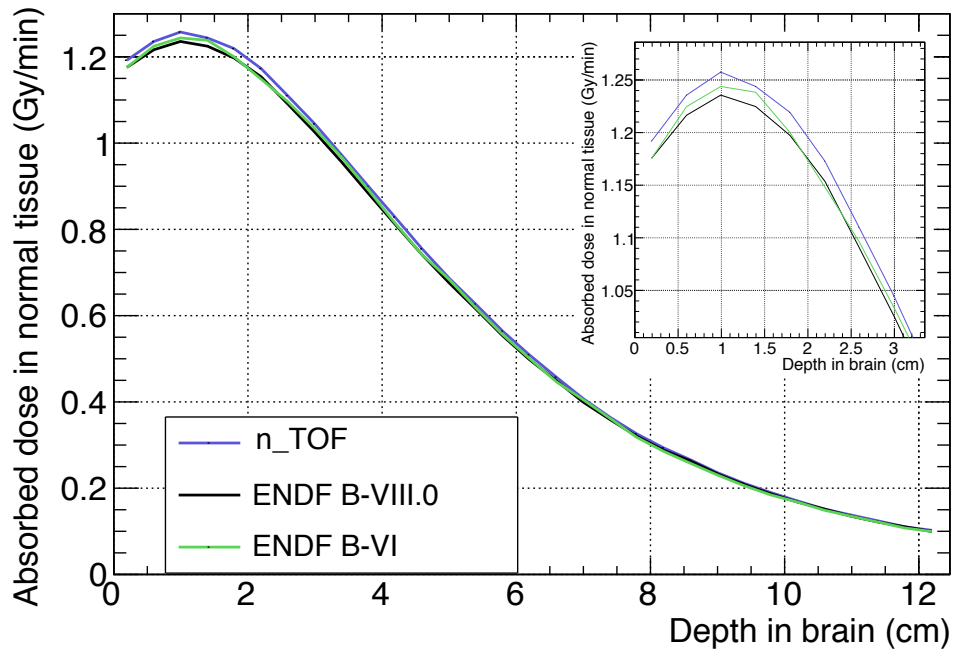
FIGURE 3.46: Simulated BNCT dose rates in the brain from the $^{35}Cl(n,\gamma)$ reaction as a function of depth into the brain. The results derived from the n_TOF cross section are compared to those derived using cross sections from the ENDF B-VI library, and the updated values in the ENDF B-VIII.0 library.

3.12 Summary, conclusions and outlook

The ^{35}Cl(n, γ) reaction is relevant to a number of diverse fields including astrophysics, waste management associated with the numerous graphite moderated reactors in the nuclear power industry, and in the novel cancer therapy 'boron neutron capture therapy'. Only two precision time-of-flight measurements exist in the literature, one of which did not report the cross section below 4 keV meaning that evaluations rely on only one data set in this region. In the region covered by both measurements, evaluations differ by around 15%, motivating a new precision measurement, the aim of this work.

The ^{35}Cl(n, γ) reaction yield was measured over a wide energy range from thermal energies to around 60 keV using the total energy detection set-up at the 185 m beamline at the n_TOF facility at CERN. The Legnaro-C_6D_6 set-up was used for the measurement, and its low neutron sensitivity meant that corrections associated with prompt background resulting from neutrons scattered from the sample were negligible. The systematic uncertainty associated with the measured yield was 4.4% up to 10 keV and 5.6% above 10 keV. Beyond 60 keV, limited statistics and a prohibitive background level prevented an accurate measurement. The individual analysis steps have been documented, and in places novel strategies have been presented. The steps included:

- Corrections for dead-time and multiple hits

- A comprehensive background study facilitated by dedicated ancillary measurements and Monte-Carlo simulations both to perform an accurate background subtraction and to understand the limitations of the measurement in this work.

- Application of the pulse height weighting technique in order to implement the total energy detection method, for which dedicated Monte-Carlo simulations of the capture cascades have been used to correct for the effect of finite electronic thresholds and internal conversion.

- Final normalisation of the reaction yield relative to that of the 4.9 eV saturated resonance of ^{197}Au using the saturated resonance method.

The cross section was determined from the measured reaction yield via a resonance analysis with the R-Matrix code SAMMY taking the response of the time-of-flight spectrometer into account. The parameters of thirteen resonances in the resolved resonance region were determined (with 272 reported in the ENDF B-VIII.0 library);

for these measured resonances, the kernels are consistently larger than those reported in the major evaluations ENDF B-VIII.0 and JEFF-3.3 by around 15%. They are however more consistent with one of the previous measurements (Macklin *et al.* [42]), further strengthening the conclusion that evaluations systematically underestimate the cross section in the resolved resonance region. The background level dominated the counts for the remaining resonances reported in the major evaluations. The thermal cross section was not directly measured from the reaction yield, but was inferred from the resonance parameters resulting in a value larger than the cross section in the major evaluations by around 20%; the thermal value was however based on many unmeasured resonances whose contribution were inferred using resonance parameters from the ENDF B-VIII.0 library and scaled based on the comparison of the strengths of the measured resonances to those in the library. A complementary measurement via neutron irradiation and AMS is foreseen, with a neutron irradiation at the ILL (Institut Laue-Langevin) research reactor and the DREAMS AMS facility for example.

The detailed background study highlights the issues when measuring the capture cross sections of light nuclei at the 185 m beam-line at n_TOF. The energy resolution of the time-of-flight spectrometer should in principle have allowed the measurement of resonances of the $^{35}Cl+n$ reaction up to the inelastic scattering threshold (around 200 keV); in practice, this was hindered by a large background associated with the neutron beam interacting with the experimental set-up and ancillary equipment in the experimental bunker (as opposed to background related to the scattering of neutrons from the sample or background from in-beam photons for example). This background study may have potential therefore to form the basis of a future optimisation allowing the resolution of weaker resonances especially important in the measurement of light nuclei.

A preliminary assessment of the implications of this measurement on the applications was made: the 30 keV Maxwellian averaged cross section relevant to astrophysical reaction rates (specifically the effect of ^{35}Cl as a neutron poison in the s-process) determined from this measurement was in better agreement with a recent dedicated AMS measurement than is the case for the two previous measurements. The implications of this measurement on the neutron poisoning effect of ^{35}Cl is < 0.1%, whilst the effect on the abundances of ^{36}Cl and ^{36}S in TP-AGB and massive stars is around 1% and 2% respectively. Based on the results of the cross section in the resolved resonance region, the effect on the production rate of the radionuclide ^{36}Cl in MAGNOX reactors is modest, leading to a $\approx 0.5\%$ increase. The thermal value from this work would imply a $\approx 14\%$ increase, although as mentioned the determination of the thermal value relied on the inclusion of many unmeasured resonances from the ENDF B-VIII.0 library.

Finally, in Boron Neutron Capture Therapy, the dose to healthy tissue in a brain tumour therapy would be 1.5-1.8% larger assuming the results of this measurement with respect to the data taken from ENDF B-VIII.0.

Chapter 4

$^{13}\mathrm{C}(n,\gamma)$ thermal cross section measurement via neutron irradiation and AMS[1]

4.1   Introduction, applications and objectives

As discussed in Section 2.2, accelerator mass spectrometry (AMS) is a post-irradiation sample analysis technique that offers a highly sensitive method for atom counting and determining the number of nuclear reactions that have occurred in certain suitable cases; it is therefore being used more frequently to measure accurate cross sections for these reactions. The ^{13}C neutron capture cross section is particularly suitable for being measured using this technique due to the wealth of experience through the use of AMS for carbon dating. The $^{13}\mathrm{C}(n,\gamma)$ cross section is of importance to both nuclear energy applications [37,91] and the slow neutron capture process in nuclear astrophysics [92]. The former is mostly concerned with the cross section at low neutron energies (meV to eV), the latter at tens of keV. The AMS measurement in Reference [92] focussed on the cross section at keV energies and thus the astrophysical implications clearly demonstrating the suitability of these techniques for measuring the ^{13}C neutron capture cross section. In this work, the thermal cross section is of interest which has implications for nuclear energy applications, in the context of waste nuclear graphite.

As was already discussed in Section 3.1, the extensive use of graphite as the moderator in nuclear reactors in Europe and elsewhere means that it represents a large proportion

---

of the current intermediate level nuclear waste (around 23% by volume in the UK). Nuclear graphite is composed of natural carbon, containing 1.1% ^{13}C. After capturing a neutron, the radioisotope ^{14}C is produced which decays via β^- radiation to ^{14}N with a half-life of 5730 ± 40 years [93]. ^{14}C is a radionuclide that can be readily incorporated into the biosphere and is of concern to nuclear regulators; to decommission and manage waste nuclear graphite in a cost-effective and safe manner, one must know how much ^{14}C is present. To avoid expensive destructive measurement techniques, one relies on the nuclear data associated with its four main production routes; $^{13}C(n,\gamma)^{14}C$, $^{14}N(n,p)^{14}C$, $^{17}O(n,\alpha)^{14}C$ and $^{18}O(n,n'\alpha)^{14}C$ in order to predict the amount of ^{14}C present in irradiated graphite via simulations of the irradiation history of the reactor. A more complete description of the issues around the presence of ^{14}C in waste graphite can be found in References [94] and [95].

Current data

The available data on the $^{13}C(n,\gamma)$ cross section is summarised in Table 4.1:

TABLE 4.1: Current experimental and evaluated data for the thermal (E_n = 25.3 meV) ^{13}C neutron capture cross section.

Reference	σ_{thermal} (mb)	Measurement technique
Measurements:		
Hennig (1954) [96]	0.9 ± 0.2	Activation + chemical separation
Bartholomew (1961) [97]	0.8 ± 0.2	PGAA
Motz (1963) [98]	1.0 ± 0.2	PGAA
Mughabghab (1982) [99]	1.37 ± 0.04	PGAA
Firestone (2016) [100]	1.496 ± 0.018	PGAA
Evaluations:		
ENDF B-VIII.0, JENDL/D-2017, TENDL 2017	1.496 ± 0.018	—
JEFF-3.3	1.37 ± 0.04	—

All but the oldest measurement used Prompt Gamma-ray Activation Analysis (PGAA) discussed in Section 2.3, detecting the 8.17 MeV γ-ray from the de-excitation of $^{14}C^\star$ formed by neutron capture on ^{13}C before normalising to the 2.2 MeV γ-ray from $^2H^\star$ as a result of neutron capture on ^{1}H which is present in a known quantity due to use of a stoichiometric sample. The previously measured values are discrepant, and the most recent results are inconsistent. As discussed in Section 2.3, the application of gamma-spectroscopic methods (such as PGAA) require prior knowledge of the level scheme of the compound system being measured; over time, the uncertainties associated with the previous measurements have decreased as knowledge of the ^{14}C and ^{2}H level schemes have improved along with improvements in detection apparatus,

leading to the most recent data from [100] having an uncertainty of ~1%. The majority of the major evaluated nuclear data libraries (ENDF B-VIII.0, JENDL/D-2017 and TENDL 2017) all adopt this value whereas JEFF-3.3 uses the smaller value from Reference [99]. Given the discrepancies between the existing measurements, the most precise of which use the same measurement technique, and the importance of this cross section, there is strong motivation for a new measurement utilising a different experimental approach.

Objectives

Neutron activation and subsequent AMS analysis, for which a sketch of the principles was given in Section 2.2, has no reliance on the level schemes of ^{14}C and ^{2}H required for PGAA measurements and thus offers an opportunity for a precise independent measurement of the ^{13}C$(n, \gamma)^{14}$C reaction cross section. It is thus the objective of this work to perform a measurement of the thermal cross section, by first irradiating isotopically pure samples of ^{13}C at the cold neutron source at the ILL research reactor and then performing an AMS measurement of the irradiated sample at the VERA facility (Vienna Environmental Research Accelerator). Such a measurement may allow for the resolution of the discrepancies between data evaluations, and will provide valuable data to complement previous measurements.

4.2   Experimental facilities

A brief description of the experimental facilities, and the specific details relevant to this measurement are given below; more general descriptions of the ILL research reactor (Institut Laue-Langevin) and VERA (Vienna Environmental Research Accelerator) can be found in References [101] and [102] respectively.

4.2.1   ILL Research reactor

The Institut Laue-Langevin houses a high-flux research reactor, operating at a power of ~ 50 MW and producing a thermal neutron flux of ~ 1.5×10^{15} neutrons/cm^2/s, using a single highly enriched ^{235}U fuel element. Neutrons are delivered to multiple experimental stations for multiple applications spanning condensed matter physics, biology, materials science, and nuclear physics. In addition to thermal neutrons (25 meV), there are two cold neutron sources ($\approx$ 4 meV and the ultracold source providing neutrons with energy $\approx$ 200 neV), and a hot source (200 meV). As shown in Figure

4.1, whilst multiple experiments are situated within the reactor hall, there are many experiments located in adjacent halls to which neutrons are delivered via efficient ballistic neutron guides [103, 104]. There are seven experiments dedicated to nuclear and particle physics; these include the fission fragment separator Lohengrin, the fission product prompt γ-ray spectrometer FIPPS, and the cold neutron beam line PF1b, the experimental station used in this work. Neutrons from the cold source (4 meV mean energy) are delivered to the PF1b station via the 76m long H113 neutron guide, with a flux of $\approx 2 \times 10^{10}$ neutrons/cm^2/s; the exit collimator of PF1b is 6×20 cm^2. PF1b is thus an ideal location for the activation of materials for thermal cross section measurements.
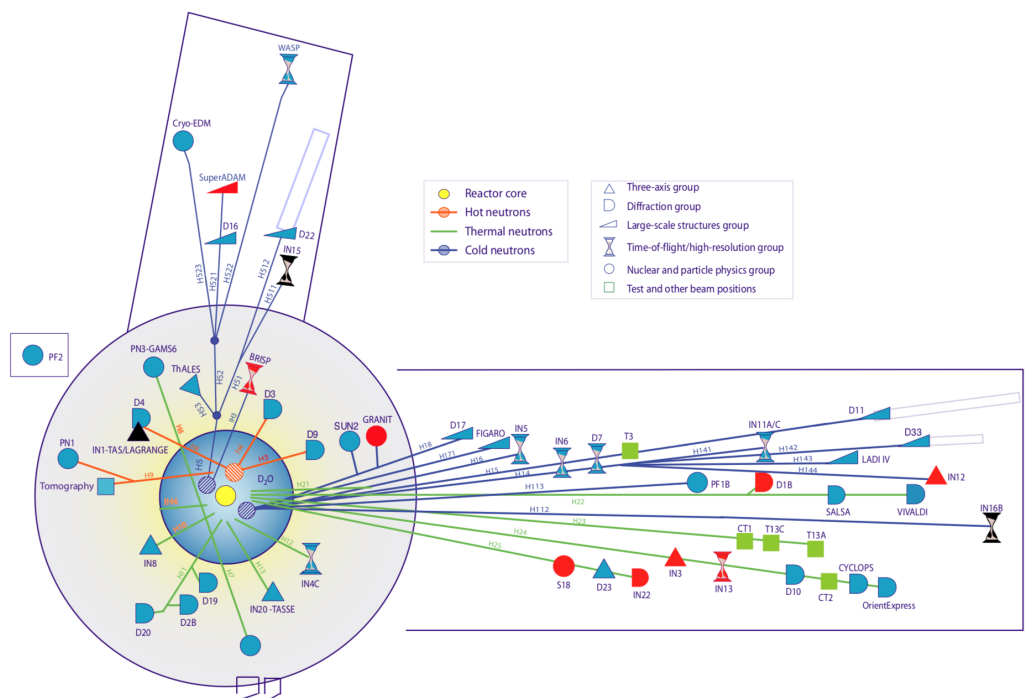
FIGURE 4.1: Schematic plan view of the ILL research reactor and associated beam-lines and experimental measuring stations. PF1b, the beamline used in this work, is situated around 80 m from the reactor core.

4.2.2   AMS and The Vienna Environmental Research Accelerator facility

AMS is a technique capable of measuring isotopic ratios as small as $\sim 10^{-15}$ for certain suitable cases, the main requirement being that the isotope of interest must form an ion (atomic or molecular) suitable for acceleration. In general an isotope of low abundance is counted relative to a stable, more abundant isotope of the same element. After acceleration, isotopes are separated via electrostatic and magnetic filters; the more abundant isotope(s) are measured using Faraday cups and the rare isotope is counted using particle detectors, either gas ionisation detectors or silicon, capable of

registering single ion counts. Normalisation and systematic background corrections are performed by measuring samples of known isotopic composition.

VERA houses an AMS facility at the University of Vienna, which is based around a 3 MV pelletron tandem accelerator. The facility opened in 1996 for the purpose of tracing long-lives isotopes in the environment; further research areas include more basic nuclear physics, archaeological studies using carbon dating, and paleoclimatology. A brief description of the main components of the acceleration scheme for the specific measurement in this work, performed at VERA, is given below making reference to Figure 4.2:

A circular sample magazine capable of holding up to 40 cathodes containing sub mg amounts of the material to be measured is mounted at the start of the accelerator (labelled 'Source 1' in Figure 4.2). Each sample is sputtered with a Cs^+ beam (produced by the heating of Cs gas on a tantalum anode), producing negative carbon ions which are extracted and pre-accelerated across a potential of 75 kV; the ion current from the ion source is typically on the order of μA, although this is dependent on the specific ionisation efficiency for a given isotope. The ion source also acts as the first filtering stage since some isotopes do not form negative ions, e.g. noble gases and nitrogen (for the case of this work, this eliminates the isobaric contaminant ^{14}N). In the 'low-energy' stage of the accelerator, an electrostatic analyser focusses the ion beam both spatially, and in energy according to E/q (energy to ionic charge) ensuring a mono-energetic beam. The ions are mass selected ($^{12}C^-$, $^{13}C^-$ or $^{14}C^-$) for a charge state of -1 by the injection magnet according to ME/q^2 where M is the mass, before being injected into the main accelerator. To switch between different masses quickly, the injection magnet features a multi beam switcher (MBS) which provides an additional accelerating stage of up to 13 kV; this is important for characterising the transmission through to the high energy side of the accelerator for making isotopic ratio measurements, without needing to ramp the magnetic field of the injection magnet. Additional components in the low energy side include electrostatic steerers, a magnetic quadrupole doublet and Einzel lens for refining beam optics, and two offset Faraday cups are used to ensure transmission of the beam into the main accelerator.

The main accelerator at VERA is a +3 MV pelletron tandem: negative ions in the -1 charge state are accelerated towards the positive terminal as they traverse a stripper (a gas stripper was used in this work: O_2 at ~ μbar pressure, but thin metallic foils can be used where higher charge states are required) producing positive ions, as well as dissociating any molecular ions, further reducing isobaric contaminants. The positive ions are further accelerated by the same potential. On the high energy side of the accelerator, there is the potential for velocity selection using a Wien filter (not used in

this work), and elements for beam optics. A subsequent analysing magnet separates the carbon isotopes by mass; the beams of the two stable isotopes (^{12}C^{3+} and ^{13}C^{3+}) impinge on separate Faraday cups where their current is measured and individual ^{14}C^{3+} ions are directed by a further electrostatic analyser into a gas ionisation chamber. Recording the currents measured with the Faraday cups in relation to the count rate in the ionisation chamber yields isotopic ratios, after calibrating the system using samples of known isotopic composition. This procedure is detailed in Section 4.4.
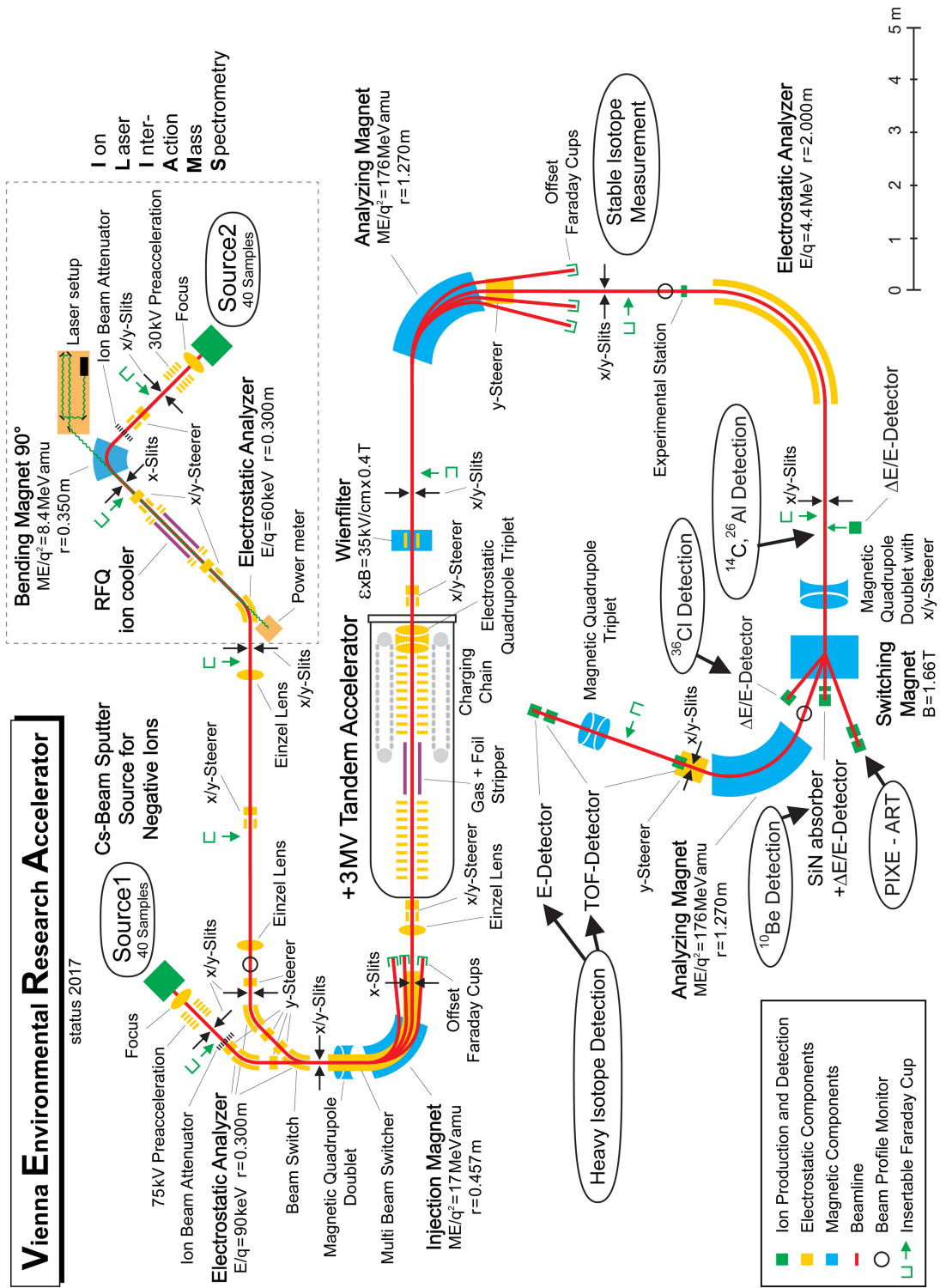
FIGURE 4.2: Schematic of the VERA AMS facility used for this measurement [105]. The ion source used in this measurement is 'Source 1'.

4.3 Neutron irradiation

4.3.1 Sample preparation

Samples of ~ 10 mg amorphous graphite powder enriched to 99.5% ^{13}C were prepared for irradiation by firstly removing the impurities, described below, and flame sealing in cylindrical quartz ampoules shown in Figure 4.3. The mass and dimensions of the samples were chosen such that the thin target approximation ($Y = n\sigma$) in Equation 2.2 is valid. MCNP simulations confirmed that the neutron flux downstream of the carbon containing quartz ampoules is unperturbed by the samples, and that any effect due to the decrease of neutron flux with distance through the samples can be neglected.
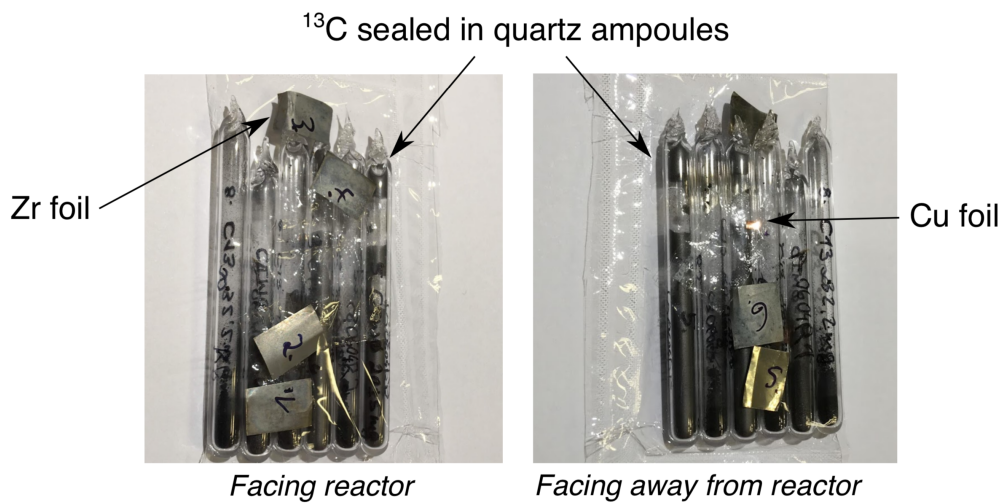
FIGURE 4.3: Photograph of the graphite powder ^{13}C samples and flux monitors in close proximity to the samples prior to irradiation. For reference, the diameter of the cylindrical ampoules is 4 mm.

Since the post-irradiation AMS measurement is not sensitive to the mechanism by which ^{14}C is produced during the irradiation, all other potential production routes must be considered as sources of systematic background, and if necessary mitigated:

- The other main production route of ^{14}C is via the ^{14}N(n, p)^{14}C reaction, where the cross section is over 1000× larger than is the case for the ^{13}C(n, γ)^{14}C reaction; the presence of trace amounts of the adsorbate ^{14}N in the graphite samples (from prior exposure to atmospheric conditions) may therefore represent a significant source of systematic error when inferring the ^{13}C(n, γ) cross section from the measured ^{14}C content in the irradiated samples; indeed there was a large effort to account for the effects of ^{14}N, discussed below.

- The production of ^{14}C from the ^{17}O(n, α) reaction from the presence of atmospheric ^{17}O is negligible due to the combination of the low natural abundance of ^{17}O (0.038%) and the relatively small reaction cross section (0.235 b) — the presence of ^{17}O as an adsorbate in the graphite samples is also reduced via the steps taken to reduce the ^{14}N content; see below. The quartz ampoules contain 0.02% ^{17}O by mass and any produced ^{14}C has a recoil energy of 0.4 MeV and an average longitudinal range of 0.93 μm in quartz. It is therefore foreseeable that ^{14}C could implant into the amorphous carbon powder increasing its ^{14}C content. The production rate of ^{14}C from this mechanism is however three to five orders of magnitude less than the production rate from ^{13}C(n, γ) depending on assumptions made about the spatial distribution of carbon within the ampoule, and is thus negligible.

- Finally the ^{18}O$(n, n'\alpha)$ reaction is negligible as a source of ^{14}C because of the high neutron energy threshold (several MeV) for this reaction.

Due to the difficulty in accurately measuring the ^{14}N content of the samples pre-irradiation in order to account for the ^{14}N$(n, p)^{14}$C production route, there was a concerted effort to remove as much ^{14}N from the samples as possible such that any final systematic correction associated with its content would be kept to a minimum. There were two iterations of the experiment; in the first iteration, five samples containing between 9 and 99 mg ^{13}C were prepared at PSI (Paul Scherrer Institute, Switzerland) by heating the graphite within 0.4 cm diameter, 3.5 cm length quartz ampoules with a blow torch to red heat under vacuum before flame sealing, thereby allowing any adsorbates to escape. As is explained in Section 4.4.1 however, the nitrogen content of this initial set of samples was not verifiable, prompting a second experiment. The second set of samples was prepared under more controlled and stringent conditions; five ^{13}C samples, with masses between 12 and 36 mg, were prepared at VERA by baking at 900°C under vacuum in quartz ampoules for two hours, before furnace sealing. Three further samples of natural (fossil) carbon weighing between 20 and 36 mg were prepared using the same method at VERA as a means to estimate the effectiveness of the nitrogen removal (see Section 4.4.1). The first and second batches were irradiated and analysed via AMS in two separate measurements, referred to as experiment A ('a' samples) and experiment B ('b' samples) hereafter[2].

Due to the difference in equipment and change in experimental procedure for the two sample production methods, one may expect that the effectiveness of the nitrogen removal would be different in the two experiments; a non-negligible nitrogen content

---

[2]Experiment A was performed in 2016 and for which none of the experimental work was performed by S. Bennett, but by the co-authors of Reference [1]. Experiment B was performed in 2018.

would therefore be made apparent by comparing the measured ^{14}C production cross section ($\sigma_{13}C_{n,\gamma}$ + $\sigma_{14}N_{n,p}$) from the two irradiations. Similar cross sections would indicate either a negligible nitrogen content or, more unlikely, that both methods of nitrogen removal were equally, but not perfectly, effective. Significantly different values would indicate that either one or both methods of removal were not successful. Furthermore, by irradiating natural carbon in experiment B, any ^{14}C production from ^{14}N would be more pronounced due to the natural isotopic reduction by a factor of ∼100 of ^{14}C produced by ^{13}C. The natural carbon used in experiment B had a visibly larger grain size than the enriched ^{13}C; is was therefore not possible to directly infer the ^{14}N content in the enriched samples from the natural carbon measurement as in principle one may expect that the level of nitrogen adsorption to depend on the surface area of the powder. This check nevertheless provided reassurance in the effectiveness of the ^{14}N removal. There is further discussion regarding the nitrogen content in Section 4.4.1. Details of each of the samples used for the measurement are summarised in Table 4.3.

4.3.2 Irradiation and neutron flux measurement

For both experiments A and B, the samples (inside the quartz ampoules) were irradiated in the primary casemate of the PF1b beam-line at ILL (operating at a power of 52.8 and 52.5 MW respectively), where a thermal equivalent flux (defined below) of $\sim 2 \times 10^{10}$ neutrons/cm^2/s is achieved with an area of 120 cm^2. The irradiations were performed within an active area of ∼20 cm^2 selected to exclude non-uniform regions close to the borders of the neutron guide. Simulations with the McStas code [106–108] showed that within the active area, the neutron flux varies by ±1% in the horizontal direction and ±2% in the vertical direction. For most of the samples, for both experiments A and B, the samples were irradiated for around 10 hours such that the final ^{14}C/^{13}C ratios were $\sim 10^{-12}$, optimal for the AMS isotopic ratio measurements at VERA; this ratio is large enough to gather statistics in a reasonable time, but small enough that sample cross-contamination can be avoided during the 'sputtering' stage, and that corrections associated with large count rates and dead-time are kept to a minimum. For experiment A, samples 1-3a were irradiated for a longer period of time than sample 4a in order to produce different ^{14}C/^{13}C ratios to assess any systematic error associated with the AMS measurements. For experiment B, sample 12b was irradiated for a longer period for the same reason. In all cases, the quartz ampoules were held in a 25 μm thick fluorinated ethylene propylene bag. For experiment A, the samples were also supported on an aluminium plate; this however was found to be unnecessary and therefore not used for experiment B.

Although the neutron flux $\phi(E_n)$ at the PF1b beam-line is well characterised in terms of its energy dependence, its absolute magnitude depends on the precise irradiation position and reactor power meaning that to obtain the most accurate cross section result, the flux must be measured during the irradiation. As discussed in Section 2.6, this is performed using a number of 'flux monitors', small ($\sim$ 10 - 100 mg) metallic foils whose thermal neutron capture cross sections are well known, as are the decay properties of the activated isotopes. For a given flux monitor isotope X, if the neutron flux is constant in time, the activity of a gamma-line i at a time T after the end of the neutron irradiation of length t_{irr} is given by

$$A_i^X = \alpha_X N k_{\gamma,i} \left(1 - e^{-\lambda_i t_{irr}}\right) e^{-\lambda_i T} \int_0^\infty \sigma_{n,\gamma}^X(E_n)\phi(E_n)\mathrm{d}E_n, \qquad (4.1)$$

where α_X is the natural abundance of the isotope which has been activated (taken from [109]), N is the total number of atoms in the flux monitor, $k_{\gamma,i}$ is the self-attenuation factor (for the foils and gamma-ray energies in this work, $k_{\gamma,i} = 1$), $\sigma_{n,\gamma}^X$ is the capture cross section for the isotope X (taken from [110]), and λ_i is the decay constant associated with the level i. Since the cross section is desired at $E_n = 25.3$ meV and the beam is not truly mono-energetic, it is the *thermal equivalent* neutron flux which is relevant: it is assumed that the cross sections of both the monitors and ^{13}C vary as $\sigma \sim 1/v$ or $\sigma \sim 1/\sqrt{E_n}$ (as described in Section 1.2) for the energy range covered by the neutron flux, with Westcott factors equal to unity[3] [111]. Under this assumption, the thermal equivalent flux, the thermal neutron flux that would have resulted in the measured activity of the flux monitor, associated with the measurement of the gamma line i is then given by

$$\phi = \int_0^\infty \sqrt{\frac{25.3 \text{ meV}}{E_n}} \phi(E_n)\mathrm{d}E_n = \frac{A_i^X}{\alpha_X N k_{\gamma,i} \sigma_{n,\gamma}^X(E_n = 25.3 \text{ meV})} \frac{e^{\lambda_i T}}{(1 - e^{-\lambda_i t_{irr}})}. \quad (4.3)$$

Two different flux monitor materials, Cu and Zr, were chosen in order to reduce systematic uncertainties associated with the nuclear data (natural isotopic abundances, activation cross sections, branching ratios and half-lives). An Au foil was also used as a flux monitor (Au is a cross section standard [26]); in this measurement however, the large neutron flux at PF1b (and hence the large activity of any activated material) stipulated the use of a sub mg foil which led to results suggesting a significantly lower

---

[3]The Westcott factor g_w quantifies the deviation from a pure $1/v$ cross section behaviour for thermal cross section measurements. For a pure thermal Maxwell-Boltzmann neutron energy spectrum ϕ_{th} whose mean energy is 25.3 meV, the Westcott factor g_w is defined such that

$$\langle\sigma\rangle_{th} = \frac{\int_0^\infty \sigma(E_n)\phi_{th}(E_n)\mathrm{d}E_n}{\int_0^\infty \phi_{th}(E_n)\mathrm{d}E_n} = g_w\sigma_{th} \qquad (4.2)$$

where σ_{th} is the cross section at 25.3 meV. For a pure $1/v$ dependence of the cross section, $g_w = 1$.

flux than for the other foils — this was likely a result of the mass measurement of such a small foil, possibly due to contaminants electrostatically attaching to the foil; the Au measurement was therefore not used. The foils were placed in close proximity to the carbon samples during the irradiation and were distributed throughout the irradiation area, both upstream and downstream of the carbon samples in order to assess any non-uniformity of the neutron beam — see Figure 4.3. The activities A_i^X of the irradiated monitors were measured using a low background high purity germanium (HPGe) detector at two discrete measuring distances (50 mm and 118 mm) to reduce any uncertainty associated with the efficiency of the device. The gamma-ray spectra for the irradiated foils were analysed with Genie2000[4]; examples of typical spectra obtained for the Cu and Zr foil measurements are shown in Figure 4.4 where the specific lines used for the measurement are indicated. The dead-time corrections associated with the activity measurements were $\sim$ 1% and $\sim$ 0.1% for the Cu and Zr foil measurements respectively; any systematic error associated with these corrections were therefore negligible.

TABLE 4.2: Measured thermal equivalent neutron flux using the flux monitors for both experimental phases A and B. See text for further details on the quoted uncertainties.

Activated isotope	Number of foils	ϕ ($\times 10^{10}$ neutrons/cm^2/s)
^{64}Cu/a	8	2.24±0.14
^{95}Zr/a	12	1.96±0.21
^{97}Zr/a	12	2.11±0.21
All foils/a	32	2.09±0.15
^{64}Cu/b	2	2.23±0.07
^{95}Zr/b	6	2.17±0.09
^{97}Zr/b	6	2.21±0.11
All foils/b	14	2.20±0.09

As predicted, no statistically significant differences were found between the foils upstream and downstream of the carbon ampoules, neither with regards to the foil positions spatially within the irradiation area. For each activated isotope, a weighted mean of the flux determined from the measurements of the different gamma-lines and physical measuring positions in the HPGe set-up was taken as the best estimate of the flux for that isotope/foil; this was in order to reduce the effect of the systematic errors associated with the Ge detector calibration at each measuring position. From these values, best estimates for the flux associated with measurements of each isotope were

---

[4]^{152}Eu was used for the Ge detector efficiency calibration. For reference the half-lives, γ-ray energies and intensities I_γ included in the Genie2000 library used were as follows:

^{64}Cu: λ=1.52×10^{-5} s^{-1}, γ_1=511 keV and I_{γ_1}=35.2%, γ_2=1345.9 keV and I_{γ_2}=0.475%.

^{95}Zr: λ=1.25×10^{-7} s^{-1}, γ_1=724.2 keV and I_{γ_1}=43.7%, γ_2=756.7 keV and I_{γ_2}=55.3%.

^{97}Zr: λ=1.14×10^{-5} s^{-1}, γ_1=743.4 keV and I_{γ_1}=92.8%.

^{97}Nb (daughter of ^{97}Zr): λ=1.60×10^{-4} s^{-1}, γ_1=657.9 keV and I_{γ_1}=98.09%.
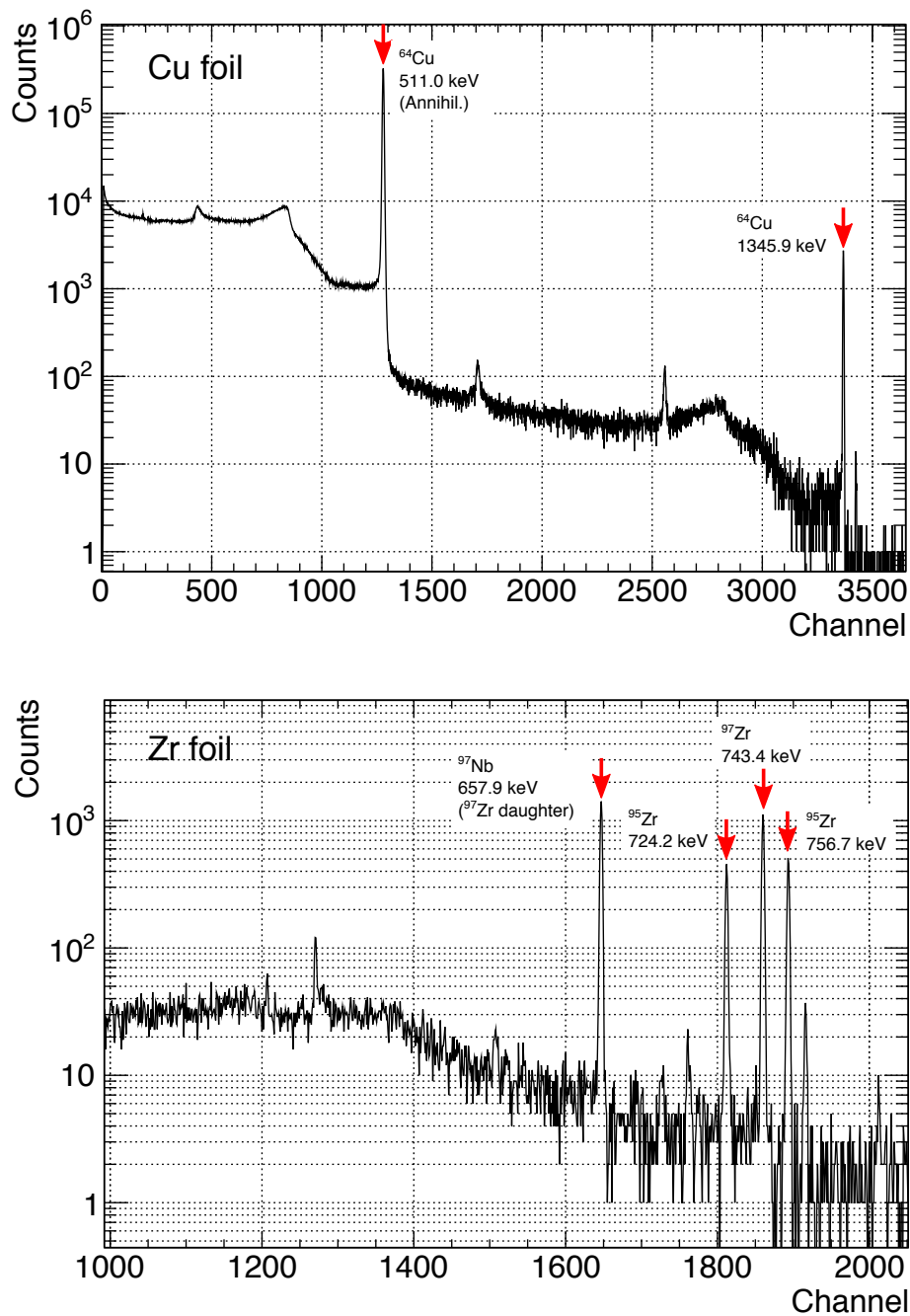
FIGURE 4.4: Example gamma-ray spectra for the Cu and Zr flux monitor foils — the lines used for determining the neutron flux are labelled.

calculated using a mean weighted by the total uncertainty (statistical and systematic) and an estimate of the error taken as one standard deviation of the measurements included in the average. These values are shown in Table 4.2. The statistical uncertainties associated with the activity measurements are linked to the duration each activated foil was measured for. For experiment A, these were approximately 6%, 5% and 4% for ^{64}Cu, ^{95}Zr and ^{97}Zr respectively; they were approximately 3%, 3%

and 2% for experiment B. For both experiments A and B, the systematic uncertainties from the neutron activation cross sections, decay constants and branching ratios were approximately 0.4%, 3.3% and 3.0% for ^{64}Cu, ^{95}Zr and ^{97}Zr respectively. The final flux values for experiments A and B, labelled 'All foils' in Table 4.2, are taken from a weighted average of all individual isotope measurements from all foils. In an improved future experiment, the systematic uncertainty associated with the flux measurement could be reduced through the use of flux monitors with 0.1% Au (where the uncertainties associated with the nuclear data: cross section, branching ratios, etc. are smaller) in an Al alloy, or in the form of a powder incorporated into the carbon samples. As will be shown in the next section, it was the flux measurement that limited the final cross section measurement uncertainty.

4.4 AMS measurement and analysis

The ^{13}C(n, γ) cross section is given by

$$\sigma_{^{13}C_{n,\gamma}} = \frac{^{14}C}{^{13}C} \frac{1}{\phi t_{irr}} \tag{4.4}$$

as per Equation 2.3, where ϕt_{irr} is the thermal equivalent neutron fluence, and $\frac{^{14}C}{^{13}C}$ is the isotopic ratio of ^{14}C (produced by the reaction ^{13}C(n,γ)) to ^{13}C, measured accurately via AMS. The decay of ^{14}C in the period between the irradiation and AMS measurement (around two months) is negligible due to the relatively long ^{14}C half-life (5730 ± 40 years [93]).

Samples suitable for AMS were firstly prepared at VERA; the quartz ampoules were broken open under normal atmospheric conditions and multiple sub-mg amounts of irradiated graphite were pressed into the aluminium sample holders (cathodes), in turn loaded onto the circular sample magazine; samples of similar expected ^{14}C/^{13}C ratios were placed adjacent to one another in order to minimise the effects of any cross-contamination. Prior to the direct measurement of the irradiated material, samples were first prepared where the irradiated material was diluted by a factor of ~100 by adding stable carbon in order to reduce the levels of ^{14}C — this was to check for the expected levels of ^{14}C without running the risk of saturating or potentially contaminating the apparatus. Each sputter sample within the sample magazine was sputtered for around five minutes during which the AMS setup switched between ^{12}C, ^{13}C or ^{14}C measurements five times per second. In both experiments A and B, the sample magazine contained three sputter samples from each carbon sample (except 12b where only one sputter sample was measured at the end of the run due

to its large ^{14}C content, see Section 4.4.1 for details), 'standard' calibration samples containing carbon with well known (<1% uncertainty) ^{14}C/^{13}C and ^{13}C/^{12}C ratios, and 'old' carbon samples which were used to periodically tune and thus optimise the detection efficiency of the set-up. Each sample was sputtered once per turn of the sample magazine and for experiments A and B there were nine and five turns of the magazine respectively.

The unknown ^{14}C/^{13}C ratios were determined by a comparison of the ion currents (associated with Faraday cup measurements of the more abundant ^{12}C and ^{13}C) and count rates (associated with the ionisation chamber measurements of the less abundant ^{14}C) to those from the well characterised 'standard' carbon samples. For experiment A, the 'IAEA C3' and 'C6' standards were used, whereas for experiment B the 'CTW2' standard was used; the ^{14}C present in the IAEA standards is from natural sources [112] whereas for CTW2, it originated from irradiating fossil carbon in the Vienna TRIGA reactor and characterizing the resultant material against multiple other standards via AMS — this is detailed in Reference [113]. Mean calibration factors that convert measured isotopic currents and count rates to true isotopic ratios were determined during each periodic tuning of the accelerator as a means to account for any systematic shifts in time. For the non-irradiated ^{13}C samples (5a, 8b and 9b) the ^{14}C count rates were only 0.09-0.1% of those measured with the irradiated samples; the contribution of this background to the measured ^{14}C cross section was therefore negligible. The AMS isotopic ratios for each of the samples are given in Table 4.3 and the resultant ^{14}C production cross sections for each sample and repeat measurement are shown in Figure 4.5. The error bars are indicative of the total error: statistical errors associated with the AMS isotopic ratio measurements dominated by counting errors, and systematic errors dominated by the relatively large uncertainty associated with the neutron fluence measurement. For each data set shown in Figure 4.5 associated with a particular sample, the uncertainties reported for the average cross sections $\bar{\sigma}$ pertain only to the statistical uncertainties, and therefore provide a means of assessing the consistency of the AMS isotopic ratio measurements for each of the samples for experiments A and B. Indeed for both experiments A and B, the isotopic ratio measurements are consistent to within 1-σ.

The ^{14}C production cross sections for each of the samples are consistent, as are the repeat measurements. This consistency implies homogeneity throughout the various experimental procedures: sample preparation, irradiation with a constant neutron flux and AMS sputter sample production. The dominant uncertainty from the AMS current and isotope measurement is expected to be statistical and of the order 1-2% [114]; this is confirmed in Table 4.3. As shown in Figure 4.5, the result of

TABLE 4.3: Summary of the irradiated carbon samples, and AMS isotopic ratios of all samples for measurements A and B. The isotopic ratio uncertainties are taken as one standard deviation of the isotopic ratios of all sputter samples associated with a given sample. No uncertainty is given for 12b because only one AMS measurement was made at the end of the experiment in order not to contaminate the apparatus with ^{14}C.

Sample	Mass (mg)	t_{irr} (min)	^{14}C / ^{13}C ($\times 10^{-12}$)
^{13}C/1a	9.1	600	1.173±0.021
^{13}C/2a	46.1	600	1.172±0.013
^{13}C/3a	99.1	600	1.199±0.022
^{13}C/4a	33.5	317	0.622±0.010
^{13}C/5a	74.7	0	0.0011±0.0003
^{13}C/6b	20.0	571	1.154±0.025
^{13}C/7b	32.2	571	1.166±0.014
^{13}C/8b	13.2	0	0.0013±0.0007
^{13}C/9b	20.0	0	0.0017±0.0008
^{nat}C/10b	23.4	571	2.41±0.14
^{nat}C/11b	201.5	571	1.86±0.15
^{nat}C/12b	36.0	13833	5150
IAEA C3	-	-	139.9±1.4
IAEA C6	-	-	164.5±1.3
CTW2	-	-	135.5±4.4

sample 4a is consistent within statistical uncertainties with samples 1-3a suggesting no systematic shifts associated with the AMS measurements.

4.4.1   Isobaric contamination from ^{14}N

As already discussed, a crucial aspect of the analysis was determining to what extent the measured ^{14}C originated from the $^{14}N(n,p)$ reaction rather than from $^{13}C(n,\gamma)$. Since the samples for the two experiments were prepared under different laboratory conditions, the similarity between the ^{14}C production cross section measurements shown in Figure 4.5 suggests that in both experiments A and B the nitrogen content was either negligible, or the techniques used for the nitrogen removal reached the same saturation limit. To quantify this, attempts were made to estimate the nitrogen content of the samples for both experiments. Since ^{14}N does not form a negative ion, it is not possible to directly measure its presence via conventional AMS techniques (this is of course advantageous for ^{14}C measurements due to the suppression of ^{14}N as isobaric background). Moreover, once the irradiated ampoules are broken open and exposed to the atmosphere, ^{14}N re-adsorbs to the carbon meaning that measuring the
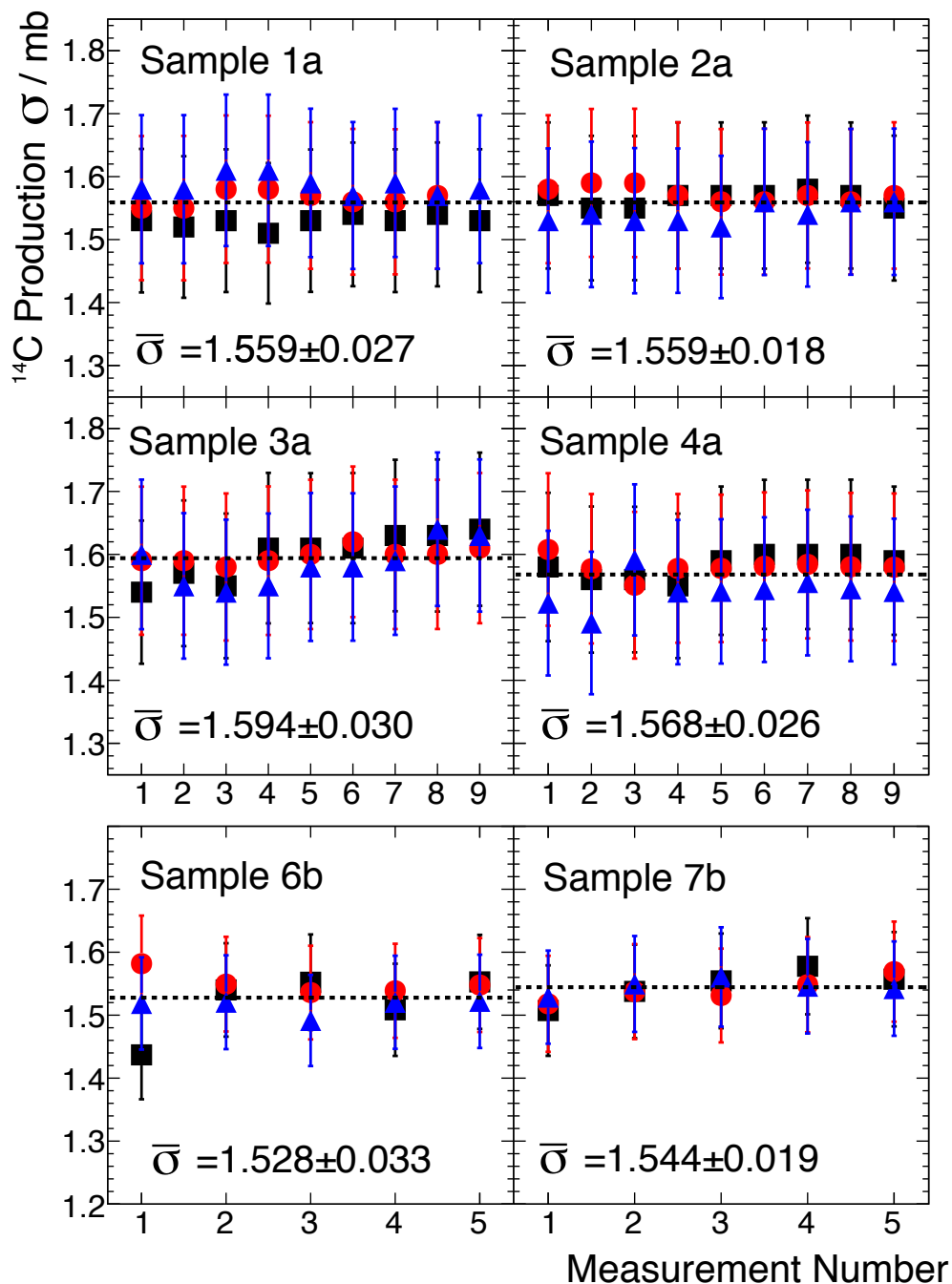
FIGURE 4.5: ^{14}C production cross sections for each carbon sample in the two AMS measurements. Circles, squares and triangles represent the three different sputter samples produced from each carbon sample. The error bars represent the total measurement error: statistical (counting statistics from the AMS measurement) and systematic (associated with the neutron fluence). The mean values $\overline{\sigma}$ state only the statistical uncertainty. Figure reproduced from Reference [1].

nitrogen content at the point of the AMS measurement is not necessarily indicative of the content during the irradiation phase.

Despite these issues, efforts were made in experiment A to estimate the ^{14}N content

using AMS by following the procedure described in Reference [92]. This involves mass selecting $A = 27$ which contains the molecule $^{13}C^{14}N^-$ and measuring the $^{14}N^{3+}$ as a result of molecular break up upon passing through the analysing magnet[5]. The 3+ charge state eliminates any background from the isobaric compound $^{13}C_2\,^1H$ which does not exist in a charge state $\geq +3$, similarly for other contaminants such as Al^-. In order to quantify the ^{14}N content with respect to the ^{13}C content, $A = 26$ was selected and the molecule $^{13}C_2^-$ measured. Comparing this count rate with that of the $^{14}N^{3+}$ measurement gives a quantity proportional to the ^{14}N to ^{13}C ratio. These measurements were performed for the carbon samples produced for experiment A (samples 1-5a) and the mean ratio was $\frac{^{14}N}{^{13}C} = (7.8 \pm 1.6) \times 10^{-5}$. In principle however, this ratio cannot be used to directly infer the ^{14}N content due to the potentially different ionization yields of $^{13}C^{14}N^-$ and $^{13}C_2^-$ and thus their respective ion extraction efficiencies. In an attempt to correct for this, a stoichiometric compound containing carbon and nitrogen must be measured; for this work sputter samples containing uracil ($C_4H_4N_2O_2$) were prepared and the measured $^{14}N/^{12}C$ ratio was compared to the true isotopic ratio of 1:1.986. The negative ion yield from the sputter samples is in principle affected by the sample matrix and composition; various uracil sputter samples were therefore prepared and measured. Some were diluted with graphite in order to simulate the real targets, but all measurements showed similar ionization yields for $^{12/13}C_2^-$ and $^{12/13}C^{14}N^-$. Comparing the currents associated with these molecules as described above is therefore sufficiently representative of the $\frac{^{14}N}{^{13}C}$ ratio for these purposes, suggesting a ~78 ppm nitrogen content in the AMS sputter samples prepared from samples 1-5a. It follows that, if this level of nitrogen contamination was present during the ampoules that underwent neutron irradiation, ~9.5% of the ^{14}C present after the irradiation would have originated from $^{14}N(n,p)$. As mentioned above however, there is no way to quantify the amount of nitrogen present in the samples during the irradiation or afterwards introduced during the production of the AMS sputter samples. This 9.5% contribution value therefore represents an upper limit and is likely an over-estimate. For this reason, the results from experiment A (samples 1-5a) were not included in the final calculation of the $^{13}C(n,\gamma)$ cross section.

For experiment B, the approach taken was to use the natural carbon samples (10-12b) to estimate the nitrogen content. The samples were prepared following the same procedure used for the ^{13}C samples and were irradiated in order to produce measurable levels of ^{14}C. For these samples, the production of ^{14}C from ^{13}C is suppressed by a factor of ~ 100 due to the lower natural isotopic abundance of ^{13}C, such that the ^{14}C content of the irradiated samples is more sensitive to the ^{14}N content at the time of

---

[5]Mass selecting $A = 27$ also gives $^{12}C^{15}N^-$ — this molecule can be neglected in this case due to the high ^{13}C enrichment of the samples and the low ^{15}N natural abundance.

irradiation. For example, a natural carbon sample with a nitrogen content of 78 ppm would produce almost a factor of ten more ^{14}C from the ^{14}N(n,p) production route compared to that from ^{13}C(n,γ). Assuming a similar ^{14}N content in the ^{nat}C and ^{13}C samples after flame sealing (despite their different grain sizes as discussed in Section 4.3.1), the best estimate of the nitrogen content with respect to the ^{12}C content is given by

$$n_{^{14}\text{N}} = \frac{1}{\phi t_{\text{irr}} \sigma_{^{14}\text{N}_{n,p}}} \left(\frac{N_{^{14}\text{C}}}{N_{^{12}\text{C}}} - \frac{N_{^{13}\text{C}}}{N_{^{12}\text{C}}} \phi t_{\text{irr}} \sigma_{^{13}\text{C}_{n,\gamma}} \right), \qquad (4.5)$$

where $n_{^{14}\text{N}}$ is the fractional ^{14}N content, $N_{^{12,13,14}\text{C}}$ are the number of atoms of the relevant carbon isotope, ϕ is the neutron flux and σ_i are the relevant thermal capture cross sections; $\sigma_{^{13}\text{C}_{n,\gamma}}$ was taken from [110] and $\sigma_{^{14}\text{N}_{n,p}}$ taken from [115]. The experimental values $n_{^{14}\text{N}}$ for the natural carbon samples are given in Table 4.4. Although this approach relies on prior knowledge of the cross sections (not least the ^{13}C(n,γ) cross section) which have their own associated uncertainties, the variation of the ^{14}N contents of the samples deduced using this method dominates any such uncertainties.

TABLE 4.4: Results for the three irradiated ^{nat}C samples and their inferred nitrogen content.

Sample	^{14}N content (ppm)
10b	9.7±0.6
11b	5.5±0.6
12b	40800±200

An 8 ppm ^{14}N content would contribute ~1% to the ^{14}C production in a thermal neutron irradiation of the enriched ^{13}C samples. It is therefore clear from Table 4.4 that the sample production method, baking under vacuum and flame sealing, was successful in removing nitrogen to levels within the various other experimental uncertainties for two of the samples. The third sample, however, which was irradiated for ~ 24 times longer contained over 2000 times more ^{14}C, implying a nitrogen content of 4%. This huge difference could perhaps be due to an incomplete flame sealing after the ampoule had been heated.

If the assumption is made that all the carbon samples prepared for experiments A and B have a negligible ^{14}N content, and therefore that all measured ^{14}C is produced from ^{13}C(n,γ), the cross section for this reaction is given by Equation 4.4. Values for the cross section calculated in this way are shown in Figure 4.5 for each of the ^{13}C samples. The consistency of the cross sections for the different samples is indicative of the nitrogen content being similar for both sets of samples, for experiments A and B, despite the samples being produced separately under slightly different conditions. It was therefore assumed that the nitrogen contents measured from the ^{nat}C samples

(shown in Table 4.4) could be used to calculate the contribution of nitrogen to the final cross section; the ^{14}N is expected to contribute (0.93±0.39)% to the post-irradiation measured ^{14}C for the ^{13}C samples.

4.5   Results

Only samples 6b and 7b were included in the cross section calculation, since these were the samples for which estimates of the nitrogen content were most reliable. The mean ^{14}C/^{13}C ratio of $(1.159 \pm 0.021) \times 10^{-12}$ produced during an irradiation with a length of 34260 s and a thermal equivalent flux of $(2.20 \pm 0.09) \times 10^{10}$ n/cm^2/s implies a ^{14}C production cross section of 1.538±0.069 mb. This value was reduced by (0.93±0.39)% to account for the estimated ^{14}C production from ^{14}N(n, p) to give a final result of σ=1.52±0.07 mb, which is compared to existing data in Figure 4.6. The result is in agreement with the most recent value measured via PGAA [100] which used experimental and analytical methods independent to those of this measurement, and is subject to different systematic sources of uncertainty. For example in the case of the PGAA measurements, nitrogen contamination is not problematic since the 8.17 MeV γ-ray (characteristic of the decay of ^{14}C*) is not produced in the ^{14}N$(n, p)^{14}$C reaction, since its Q-value is only 625.9 keV. A new normalisation of the results from Reference [99] was performed in Reference [100], using more precise data giving a cross section value of 1.502±0.027 mb, also in excellent agreement with the result of this work. The other previous measurement sensitive to nitrogen contamination is that of Reference [96]; it is likely that the nitrogen contribution to the ^{14}C production cross section was overestimated in this measurement as before accounting for this, their measured production cross section was 1.5±0.2 mb, also in agreement with the most recent PGAA value and the result of this measurement.

4.6   Summary and Conclusions

Details of the first measurement of the ^{13}C(n, γ) thermal cross section using neutron irradiation and AMS have been presented; the result of σ=1.52±0.07 mb suggests that the nuclear data evaluations should adopt the higher thermal cross section value used in ENDF/B-VIII.0, 11% larger than that reported on the other major evaluations[6]. For this measurement, understanding the amount of ^{14}C produced from the ^{14}N(n, p) reaction was crucial for an accurate result and it has been shown that through a

---

[6]The results and summary of the experimental procedures for this measurement is also available on EXFOR [116].
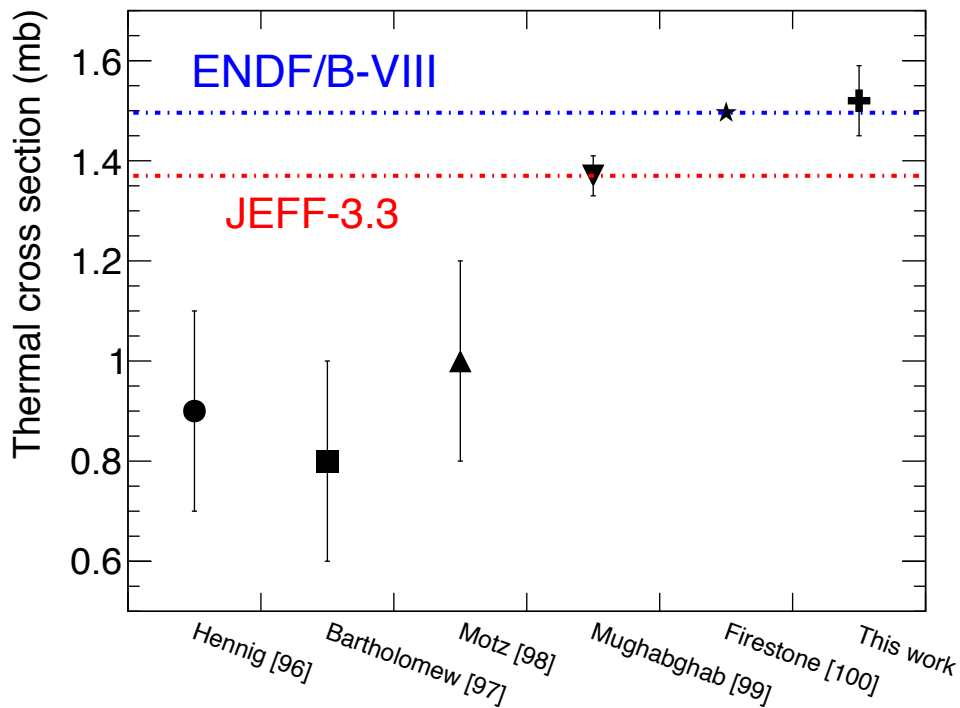
FIGURE 4.6: The measured ^{13}C(n, γ) thermal cross section compared to other measurements and evaluations. Figure reproduced from Reference [1].

stringent sample preparation procedure, the nitrogen content of the samples has been managed so that its contribution is almost negligible.

The confirmation of the nuclear data used in the calculations for ^{14}C production in graphite moderated reactors suggest that any disagreements between calculated and measured ^{14}C activation levels are likely due to the chosen elemental composition and distribution within the graphite for the calculations rather than the nuclear data; as was demonstrated by one of the samples for which the flame sealing process was not successful (sample 12b), the natural adsorbant level of ^{14}N in the graphite samples used for this work produced around 50 times more ^{14}C than from the other production routes including ^{13}C(n,γ). Therefore, it is likely that the nitrogen content in graphite moderated reactors is the most important quantity for the calculation of ^{14}C levels in nuclear graphite, particularly if the reactor core was regularly exposed to air.

The use of AMS to directly count the number of transmutated nuclei is further proving to be a sophisticated and complementary technique for certain cross section measurements.

Appendix A

Capture cascade simulations

The codes NuDEX [72] and DEGEN [73] used in this work to generate accurate correlated cascades from the neutron capture state are both based on the same principle (the same also for the DICEBOX code [74]). In principle these codes can be used to calculate cascades specific to a particular resonance, but for this work cascades for thermal (off-resonance) neutron capture were calculated (as discussed in Section 3.6.3).

The approach taken is to firstly generate a full level scheme and branching ratios for the nucleus and excitation energy for which cascades are required; since excitation energies from neutron capture $> S_n$, for most nuclei this means that the capture state and the upper portion of the cascade is in a region of high level density where the properties of individual states are not known. For the upper energy region of the scheme therefore, levels are generated based on statistical models of the level density and photon strength function (which describe average gamma-ray transition probabilities). The lower energy portion of the level scheme is based on existing experimental data (energy, spin, parity, transitions and intensities, including internally converted transitions) from ENSDF [117] for example. Cascades including gamma-rays and internally converted electrons are generated by Monte-Carlo sampling of the level scheme, observing transition rules. Details can be found in References [72–74].

For this work it was the gamma-ray and internal conversion electron energy distributions that were required in order to fold with the experimental resolution to compare with the measured distributions (see Section 3.6.3). These distributions generated from the simulation of 10^6 cascades are shown in Figures A.1, A.2 and A.3. The average properties of the multiplicity and energy distributions are summarised in Table A.1 for reference.
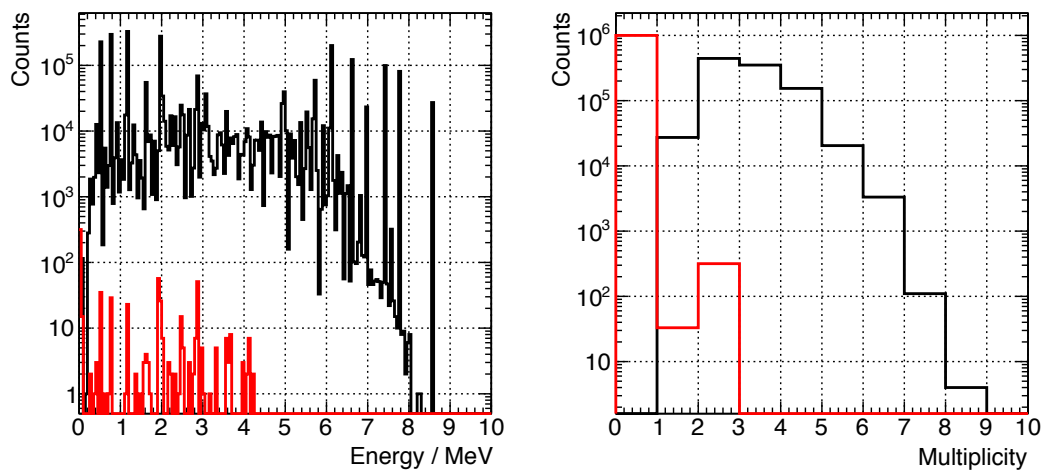
FIGURE A.1: NuDEX cascade simulation of the gamma-ray and internally converted electron energy and multiplicity distributions for thermal neutron capture on ^{35}Cl.
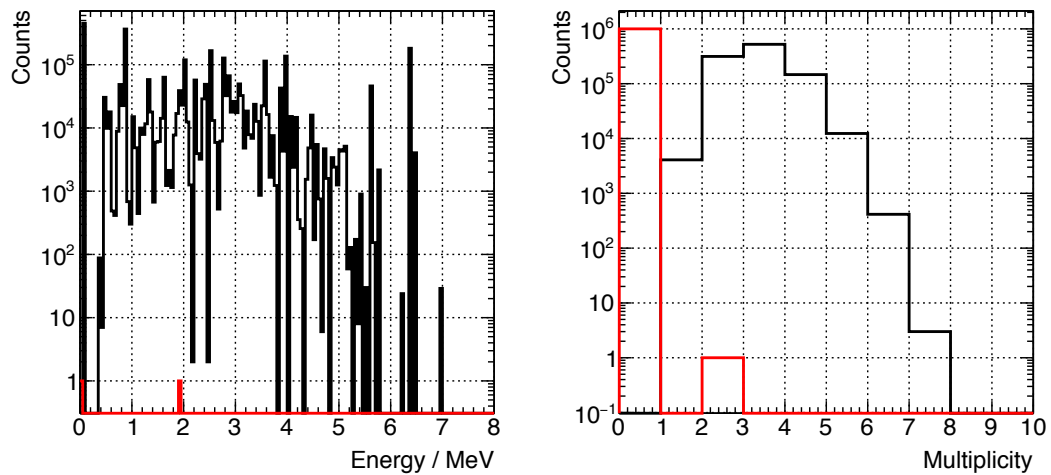
FIGURE A.2: NuDEX cascade simulation of the gamma-ray and internally converted electron energy and multiplicity distributions for thermal neutron capture on ^{23}Na.
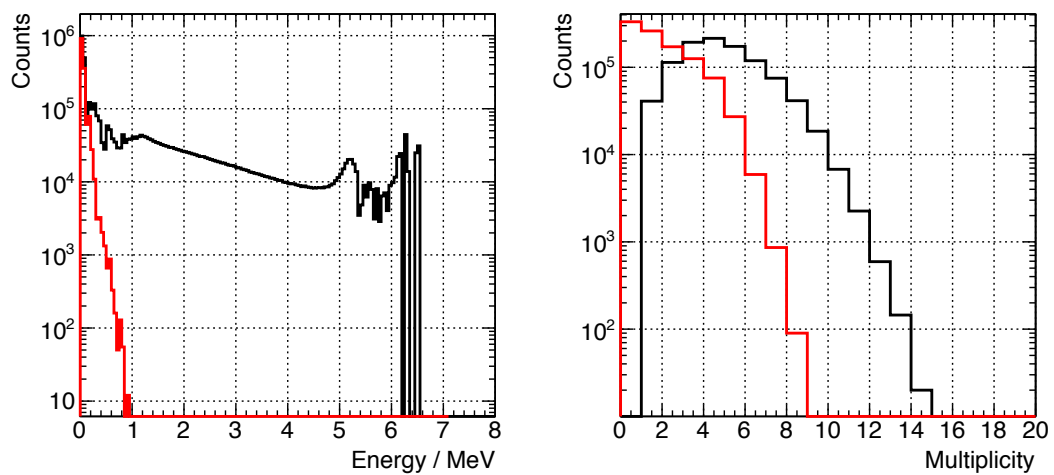
FIGURE A.3: DEGEN cascade simulation of the gamma-ray and internally converted electron energy and multiplicity distributions for thermal neutron capture on ^{197}Au.

TABLE A.1: Summary of de-excitation cascade simulations following thermal neutron capture for the three isotopes relevant to the ^{35}Cl capture measurement.
†There were only two internal conversion events out of 10^6 simulated cascades.

Cascades from thermal neutron capture on	Mean energy / MeV		Mean multiplicity	
	γ	e^-	γ	e^-
^{35}Cl	3.17	1.02	2.71	0.001
^{23}Na	2.27	— †	2.85	— †
^{197}Au	1.45	0.06	4.41	1.46

Appendix B

^{35}Cl+n resonance parameters

The full resonance parameters obtained for the resonance analysis of the ^{35}Cl(n, γ) data are given below for reference.

Table B.1: Full resonance parameters for ^{35}Cl+n from the R-Matrix analysis with SAMMY for the n_TOF data. The resonances for which only one partial width was varied are marked *. Resonances with tentative spin assignments are marked †.

		n_TOF						ENDF B-VIII.0			
E_R (eV)	J	Γ_γ (meV)	Γ_n (meV)	Γ_p (meV)	κ (meV)	Unc. κ (meV)	E_R (eV)	Γ_γ (meV)	Γ_n (meV)	Γ_p (meV)	κ (meV)
397.36	2	685.95	57.08	322.00	22.98	0.43	397.82	665.00	50.50	322.00	20.23
4243.56	1	518.92	626.41	230.00	88.63	10.27	4250.76	472.00	628.00	230.00	83.58
14758.68	2	367.52	27424.70	28.00	226.44	14.83	14802.00	345.68	32599.50	28.00	213.60
†16312.30	3	448.92	7547.36	164.02	363.30	15.47	16356.10	386.50	5981.80	164.02	309.69
17088.01	3	1007.87	12651.00	32.00	814.90	25.81	17133.90	802.28	14095.90	32.00	662.77
*†22327.11	0	1724.80	1159.87	0.00	86.69	60.79	22326.70	1724.80	966.37	0.00	77.42
26526.64	2	247.76	62300.00	0.00	154.23	24.16	26615.80	304.15	115498.00	0.00	189.59
†27262.17	2	526.16	6732.00	147.22	298.95	33.22	27276.40	457.92	6027.80	147.22	260.09
*†43995.36	1	1131.33	30541.90	0.00	409.10	89.45	44000.00	1042.90	30546.60	0.00	378.18
†51400.88	3	96.06	8032.57	96.00	82.09	30.94	51400.00	44.72	2417.15	96.00	36.97
†52757.27	2	416.86	29707.50	0.00	256.93	61.02	52774.10	562.41	815.95	0.00	208.08
54705.00	1	425.96	8608.09	0.00	152.20	76.44	54700.00	367.26	46442.40	0.00	136.64
†57585.17	2	569.98	36174.60	998.05	341.44	72.45	57611.60	538.07	107389.00	998.05	331.55

Bibliography

[1] T Wright, S Bennett, S Heinitz, U Köster, R Mills, T Soldner, P Steier, A Wallner, and T Wieninger. Measurement of the ^{13}C(n, γ) thermal cross section via neutron irradiation and AMS. *The European Physical Journal A*, 55(11):1–7, 2019.

[2] K Kolos, V Sobes, R Vogt, C Romano, MS Smith, LA Bernstein, DA Brown, MT Burkey, Y Danon, MA Elsawi, et al. Current nuclear data needs for applications. Technical report, Lawrence Livermore National Lab (LLNL), Livermore, CA (United States), 2021.

[3] M Qaim Syed. Nuclear data for medical applications: An overview of present status and future needs. In *EPJ Web of Conferences*, volume 146, page 08001. EDP Sciences, 2017.

[4] IAEA-NDS. Experimental Nuclear Data File. https://nds.iaea.org/exfor/exfor.htm. [Online; accessed 30-Sep-2021].

[5] International Atomic Energy Agency (IAEA). https://www.iaea.org. [Online; accessed 30-Sep-2021].

[6] NIRAB. UK Nuclear Innovation and Research Programme Recommendations. 2016.

[7] N Colonna, F Belloni, E Berthoumieux, M Calviani, C Domingo-Pardo, C Guerrero, D Karadimos, C Lederer, C Massimi, C Paradela, et al. Advanced nuclear energy systems and the need of accurate nuclear data: the n_TOF project at CERN. *Energy & Environmental Science*, 3(12):1910–1917, 2010.

[8] VN Manokhin and NT Kulagin. Nuclear data in the problem of fission reactor decommissioning. Technical report, 1993.

[9] I Porras, J Praena, F Arias de Saavedra, M Pedrosa-Rivera, P Torres-Sánchez, MP Sabariego, J Expósito-Hernández, JM Llamas-Elvira, A Ramírez-Navarro, A Rodríguez-Fernández, et al. BNCT research activities at the Granada group

and the project NeMeSis: Neutrons for medicine and sciences, towards an accelerator-based facility for new BNCT therapies, medical isotope production and other scientific neutron applications. *Applied Radiation and Isotopes*, page 109247, 2020.

[10] AM Lane and RG Thomas. R-Matrix theory of nuclear reactions. *Reviews of Modern Physics*, 30(2):257, 1958.

[11] FH Fröhner. Evaluation and analysis of nuclear resonance data. 2000.

[12] F Gunsing. Neutron resonance spectroscopy. 2005.

[13] J Lerendegui Marco. PhD thesis: Neutron radiative capture on 242Pu: addressing the target accuracies for innovative nuclear systems. 2019.

[14] P Schillebeeckx, B Becker, Y Danon, K Guber, H Harada, J Heyse, AR Junghans, S Kopecky, C Massimi, MC Moxon, et al. Determination of resonance parameters and their covariances from neutron induced reaction cross section data. *Nuclear Data Sheets*, 113(12):3054–3100, 2012.

[15] S Raman, ET Jurney, JW Starner, and JE Lynn. Thermal-neutron capture by silicon isotopes. *Physical Review C*, 46(3):972, 1992.

[16] A Borella, T Belgya, S Kopecky, F Gunsing, M Moxon, M Rejmund, P Schillebeeckx, and L Szentmiklosi. Determination of the 209Bi (n, γ) 210Bi and 209Bi (n, γ) 210mBi reaction cross sections in a cold neutron beam. *Nuclear Physics A*, 850(1):1–21, 2011.

[17] C Guerrero, U Abbondanno, G Aerts, H Alvarez, F Alvarez-Velarde, S Andriamonje, J Andrzejewski, P Assimakopoulos, L Audouin, G Badurek, et al. The n_TOF Total Absorption Calorimeter for neutron capture measurements at CERN. *Nuclear Instruments and Methods in Physics Research Section A: Accelerators, Spectrometers, Detectors and Associated Equipment*, 608(3):424–433, 2009.

[18] JL Ullmann, U Agvaanluvsan, A Alpizar, EM Bond, TA Bredeweg, E-I Esch, CM Folden, U Greife, R Hatarik, RC Haight, et al. The detector for advanced neutron capture experiments, a 4π BaF$_2$ detector for neutron capture measurements at LANSCE. In *AIP conference proceedings*, volume 769, pages 918–923. American Institute of Physics, 2005.

[19] RL Macklin, JH Gibbons, and T Inada. Neutron capture cross sections near 30 keV using a Moxon-Rae detector. *Nuclear Physics*, 43:353–362, 1963.

[20] U Abbondanno, G Aerts, H Alvarez, S Andriamonje, A Angelopoulos, P Assimakopoulos, CO Bacri, G Badurek, P Baumann, F Bečvář, et al. New experimental validation of the pulse height weighting technique for capture cross-section measurements. *Nuclear Instruments and Methods in Physics Research Section A: Accelerators, Spectrometers, Detectors and Associated Equipment*, 521(2-3):454–467, 2004.

[21] JL Tain, F Gunsing, D Cano-Ott, N Colonna, C Domingo, E Gonzalez, M Heil, F Käppeler, S Makrone, P Mastinu, et al. Accuracy of the pulse height weighting technique for capture cross section measurements. *Journal of Nuclear Science and Technology*, 39(sup2):689–692, 2002.

[22] A Borella, G Aerts, F Gunsing, M Moxon, P Schillebeeckx, and R Wynants. The use of C6D6 detectors for neutron induced capture cross-section measurements in the resonance region. *Nuclear Instruments and Methods in Physics Research Section A: Accelerators, Spectrometers, Detectors and Associated Equipment*, 577(3):626–640, 2007.

[23] KH Guber. High-Resolution Neutron Cross-Section Measurements at the Oak Ridge Electron Linear Accelerator. 2010.

[24] JE Escher, JT Burke, RO Hughes, ND Scielzo, RJ Casperson, S Ota, HI Park, A Saastamoinen, and TJ Ross. Constraining neutron capture cross sections for unstable nuclei with surrogate reaction data and theory. *Physical Review Letters*, 121(5):052501, 2018.

[25] A Ratkiewicz, JA Cizewski, JE Escher, G Potel, JT Burke, RJ Casperson, M McCleskey, RAE Austin, S Burcher, RO Hughes, et al. Towards Neutron Capture on Exotic Nuclei: Demonstrating $(d, p\gamma)$ as a Surrogate Reaction for (n, γ). *Physical Review Letters*, 122(5):052502, 2019.

[26] IAEA. Nuclear Data Standards. https://www-nds.iaea.org/standards/. [Online; accessed 19-Sep-2021].

[27] RL Macklin, J Halperin, and RR Winters. Absolute neutron capture yield calibration. *Nuclear Instruments and Methods*, 164(1):213–214, 1979.

[28] NM Larson. Updated Users' Guide for SAMMY Multilevel R-matrix Fits to Neutron Data Using Bayes' Equation. Technical report, Oak Ridge National Lab. (ORNL), TN (US), 1998.

[29] MC Moxon. REFIT: A least quare fitting program for resonance analysis of neutron transmission data. Technical report, 1979.

[30] RF Barth, MH Vicente, OK Harling, WS Kiger, KJ Riley, PJ Binns, FM Wagner, M Suzuki, T Aihara, I Kato, et al. Current status of boron neutron capture therapy of high grade gliomas and recurrent head and neck cancer. *Radiation Oncology*, 7(1):1–21, 2012.

[31] Nuclear Physics European Collaboration Committee (NUPECC), Nuclear Physics for Medicine, ESF Report. http://www.nupecc.org/pub/npmed2014.pdf. [Online; accessed 29-Sep-2021].

[32] International Atomic Energy Agency (IAEA), press release. https://www.iaea.org/newscenter/news/boron-neutron-capture-therapy-back-in-limelight-after-successful-trials. [Online; accessed 29-Sep-2021].

[33] I Porras and T Wright. Measurement of the ^{35}Cl(n,γ) cross section at n_TOF EAR1. Technical report, CERN, Geneva, Jan 2018.

[34] SE Jensen and Erik Nonbøl. Description of the magnox type of gas cooled reactor (MAGNOX). 1999.

[35] E Nonbøl. Description of the advanced gas cooled type of reactor (AGR). Technical report, Nordisk Kernesikkerhedsforskning, 1996.

[36] UK Nuclear Decommissioning Authority. Radioactive Wastes in the UK: - UK Radioactive Waste Inventory. Technical report, ISBN: 978-1-905985-33-3. Technical report, 2017.

[37] RW Mills, Z Riaz, and AW Banford. Nuclear data issues in the calculation of C-14 and Cl-36 in irradiated graphite. In *Proceedings of the European Nuclear Conference (ENC'12)*, 2012.

[38] L Taylor. Masters thesis: The Sensitivity of Activation Product Inventory Calculations to Perturbations in Cross Section Data. 2016.

[39] M Busso, R Gallino, and GJ Wasserburg. Nucleosynthesis in asymptotic giant branch stars: Relevance for galactic enrichment and solar system formation. *Annual Review of Astronomy and Astrophysics*, 37(1):239–309, 1999.

[40] F Käppeler, R Gallino, S Bisterzo, and W Aoki. The s-process: Nuclear physics, stellar models, and observations. *Reviews of Modern Physics*, 83(1):157, 2011.

[41] M Asplund, N Grevesse, AJ Sauval, and P Scott. The chemical composition of the sun. *Annual Review of Astronomy and Astrophysics*, 47:481–522, 2009.

[42] RL Macklin. Resonance neutron capture by 35,37Cl. *Physical Review C*, 29(6):1996, 1984.

[43] KH Guber, RO Sayer, TE Valentine, LC Leal, RR Spencer, John A Harvey, PE Koehler, and T Rauscher. New maxwellian averaged neutron capture cross sections for 35,37Cl. *Physical Review C*, 65(5):058801, 2002.

[44] RO Sayer, KH Guber, LC Leal, NM Larson, and T Rauscher. R-matrix analysis of Cl neutron cross sections up to 1.2 MeV. *Physical Review C*, 73(4):044603, 2006.

[45] S Pavetich, A Wallner, M Martschini, S Akhmadaliev, Iris Dillmann, K Fifield, S Halfon, T Heftrich, F Käppeler, C Lederer-Woods, et al. Accelerator mass spectrometry measurement of the reaction 35Cl(n, γ)36Cl at keV energies. *Physical Review C*, 99(1):015801, 2019.

[46] C Massimi, P Koehler, S Bisterzo, N Colonna, R Gallino, F Gunsing, F Käppeler, G Lorusso, A Mengoni, M Pignatari, et al. Resonance neutron-capture cross sections of stable magnesium isotopes and their astrophysical implications. *Physical Review C*, 85(4):044615, 2012.

[47] C Rubbia. Resonance enhanced neutron captures for element activation and waste transmutation (CERN). Technical report, 1997.

[48] C Rubbia, A Tzima, Y Kadi, SA Andriamonje, I Goulas, R Cappi, S Buono, JPC Revol, P Cennini, D Bouvet-Bensimon, et al. A high Resolution Spallation driven Facility at the CERN-PS to measure Neutron Cross Sections in the Interval from 1 eV to 250 MeV. Technical report, 1998.

[49] U Abbondanno. CERN n_TOF facility: Performance report. Technical report, 2003.

[50] C Guerrero, A Tsinganis, E Berthoumieux, M Barbagallo, F Belloni, F Gunsing, C Weiß, E Chiaveri, M Calviani, V Vlachoudis, et al. Performance of the neutron time-of-flight facility n_TOF at CERN. *The European Physical Journal A*, 49(2):1–15, 2013.

[51] E Chiaveri et al. Proposal for n_TOF Experimental Area 2. Technical report, 2012.

[52] M Sabaté-Gilarte, M Barbagallo, N Colonna, F Gunsing, P Žugec, V Vlachoudis, YH Chen, A Stamatopoulos, J Lerendegui-Marco, MA Cortés-Giraldo, et al. High-accuracy determination of the neutron flux in the new experimental area n_TOF-EAR2 at CERN. *The European Physical Journal A*, 53(10):1–13, 2017.

[53] M Barbagallo et al. High-accuracy determination of the neutron flux at n_TOF. *The European Physical Journal A*, 49(12):156, 2013.

[54] F Belloni, S Andriamonje, E Berthoumieux, M Brugger, M Calviani, E Chiaveri, N Colonna, Y Giomataris, C Guerrero, F Gunsing, et al. Neutron beam imaging with an XY-micromegas detector at n_TOF at CERN. *Physica Scripta*, 2012(T150):014004, 2012.

[55] C Paradela, L Tassan-Got, L Audouin, B Berthier, I Durán, L Ferrant, S Isaev, C Le Naour, C Stephan, D Tarrio, et al. Neutron-induced fission cross section of U234 and Np237 measured at the CERN Neutron Time-of-Flight (n_TOF) facility. *Physical Review C*, 82(3):034601, 2010.

[56] DB Gayther. International intercomparison of fast neutron fluence-rate measurements using fission chamber transfer instruments. *Metrologia*, 27(4):221, 1990.

[57] S Marrone, PF Mastinu, U Abbondanno, R Baccomi, E Boscolo Marchi, N Bustreo, N Colonna, F Gramegna, M Loriggiola, S Marigo, et al. A low background neutron flux monitor for the n_TOF facility at CERN. *Nuclear Instruments and Methods in Physics Research Section A: Accelerators, Spectrometers, Detectors and Associated Equipment*, 517(1-3):389–398, 2004.

[58] G Lorusso, N Colonna, S Marrone, G Tagliente, M Heil, D Cano-Ott, M Mosconi, C Moreau, A Mengoni, U Abbondanno, et al. Time–energy relation of the n_TOF neutron beam: energy standards revisited. *Nuclear Instruments and Methods in Physics Research Section A: Accelerators, Spectrometers, Detectors and Associated Equipment*, 532(3):622–630, 2004.

[59] P Mastinu, G Prete, C Guerrero, C Massimi, D Cano-Ott, PM Milazzo, J Praena, AR García, F Mingrone, F Gramegna, et al. New C_6D_6 detectors: reduced neutron sensitivity and improved safety. Technical report, 2013.

[60] R Plag, M Heil, F Käppeler, P Pavlopoulos, R Reifarth, K Wisshak, n_TOF Collaboration, et al. An optimized C6D6 detector for studies of resonance-dominated (n, γ) cross-sections. *Nuclear Instruments and Methods in Physics Research Section A: Accelerators, Spectrometers, Detectors and Associated Equipment*, 496(2-3):425–436, 2003.

[61] P Žugec, N Colonna, D Bosnar, S Altstadt, J Andrzejewski, L Audouin, M Barbagallo, V Bécares, F Bečvář, F Belloni, et al. GEANT4 simulation of the neutron background of the C6D6 set-up for capture studies at n_TOF. *Nuclear*

Instruments and Methods in Physics Research Section A: Accelerators, Spectrometers, Detectors and Associated Equipment, 760:57–67, 2014.

[62] CERN. Advanced storage manager. https://castor.web.cern.ch/castor/. [Online; accessed 19-Sep-2021].

[63] P Žugec, C Weiß, C Guerrero, F Gunsing, V Vlachoudis, M Sabate-Gilarte, A Stamatopoulos, T Wright, J Lerendegui-Marco, F Mingrone, et al. Pulse processing routines for neutron time-of-flight data. *Nuclear Instruments and Methods in Physics Research Section A: Accelerators, Spectrometers, Detectors and Associated Equipment*, 812:134–144, 2016.

[64] J Lerendegui-Marco, C Guerrero, MA Cortés-Giraldo, and JM Quesada. Geant4 Simulations for the Analysis of (n, γ) Measurements at n_TOF. *Basic Concepts in Nuclear Physics: Theory, Experiments and Applications*, pages 209–210, 2016.

[65] S Agostinelli, J Allison, K Amako, J Apostolakis, H Araujo, P Arce, M Asai, D Axen, S Banerjee, G Barrand, et al. Geant4—a simulation toolkit. *Nuclear instruments and methods in physics research section A: Accelerators, Spectrometers, Detectors and Associated Equipment*, 506(3):250–303, 2003.

[66] MJ Safari, F Abbasi Davani, and H Afarideh. Differentiation method for localization of Compton edge in organic scintillation detectors. *arXiv preprint arXiv:1610.09185*, 2016.

[67] William R Leo. *Techniques for nuclear and particle physics experiments: a how-to approach*. Springer Science & Business Media, 2012.

[68] Judith F Briesmeister et al. MCNPTM-A general Monte-Carlo N-particle transport code. *Version 4C, LA-13709-M, Los Alamos National Laboratory*, 2, 2000.

[69] R Brun and F Rademakers. ROOT—An object oriented data analysis framework. *Nuclear Instruments and Methods in Physics Research Section A: Accelerators, Spectrometers, Detectors and Associated Equipment*, 389(1-2):81–86, 1997.

[70] F James. Minuit: Function minimization and error analysis reference manual. Technical report, CERN, 1998.

[71] C Domingo Pardo. PhD thesis: New radiative neutron capture measurement of 207Pb and 209Bi. 2004.

[72] E Mendoza, D Cano-Ott, D Jordan, JL Tain, and A Algora. NuDEX: a new nuclear γ-ray cascades generator. In *EPJ Web of Conferences*, volume 239, page 17006. EDP Sciences, 2020.

[73] D Jordan, A Algora, and JL Tain. An event generator for simulations of complex β-decay experiments. *Nuclear Instruments and Methods in Physics Research Section A: Accelerators, Spectrometers, Detectors and Associated Equipment*, 828:52–57, 2016.

[74] F Bečvář. Simulation of γ cascades in complex nuclei with emphasis on assessment of uncertainties of cascade-related quantities. *Nuclear Instruments and Methods in Physics Research Section A: Accelerators, Spectrometers, Detectors and Associated Equipment*, 417(2-3):434–449, 1998.

[75] E Mendoza. Private communication.

[76] S Druyts, C Wagemans, and P Geltenbort. Determination of the 35Cl(n, p)35S reaction cross section and its astrophysical implications. *Nuclear Physics A*, 573(2):291–305, 1994.

[77] UN Singh, HI Liou, G Hacken, M Slagowitz, F Rahn, J Rainwater, W Makofske, and JB Garg. Neutron resonance spectroscopy: Chlorine. *Physical Review C*, 10(6):2138, 1974.

[78] GHE Sims and DG Juhnke. The thermal neutron capture cross section and resonance capture integral of 35Cl for (n, γ) and (n, p) reactions. *Journal of Inorganic and Nuclear Chemistry*, 31(12):3721–3725, 1969.

[79] I Dillmann, R Plag, F Käppeler, and T Rauscher. KADoNiS v0.3 - the third update of the Karlsruhe astrophysical database of nucleosynthesis in stars. In *EFNUDAT Fast Neutrons-scientific workshop on neutron measurements, theory & applications*, 2009.

[80] SE Woosley, WA Fowler, JA Holmes, and BA Zimmerman. Semiempirical thermonuclear reaction-rate data for intermediate-mass nuclei. *Atomic Data and Nuclear Data Tables*, 22(5):371–441, 1978.

[81] T Rauscher and FK Thielemann. Astrophysical reaction rates from statistical model calculations. *arXiv preprint astro-ph/0004059*, 2000.

[82] S Goriely. Hauser-Feshbach rates for neutron capture reactions (version 8/29/2005).(2005).

[83] I Dillmann, C Domingo-Pardo, M Heil, F Käppeler, A Wallner, O Forstner, R Golser, W Kutschera, A Priller, P Steier, et al. Determination of the stellar (n, γ) cross section of 40Ca with accelerator mass spectrometry. *Physical Review C*, 79(6):065805, 2009.

[84] A Wallner, K Buczak, T Belgya, M Bichler, L Coquard, I Dillmann, R Golser, F Käppeler, A Karakas, W Kutschera, et al. Precise measurement of the thermal and stellar 54Fe(n,γ)55fe cross sections via accelerator mass spectrometry. *Physical Review C*, 96(2):025808, 2017.

[85] A Wallner, T Belgya, M Bichler, K Buczak, I Dillmann, F Käppeler, C Lederer, A Mengoni, F Quinto, P Steier, et al. Novel Method to Study Neutron Capture of 235U and 238U Simultaneously at keV Energies. *Physical Review Letters*, 112(19):192501, 2014.

[86] M Forestini and C Charbonnel. Nucleosynthesis of light elements inside thermally pulsing AGB stars-I. the case of intermediate-mass stars. *Astronomy and Astrophysics Supplement Series*, 123(2):241–272, 1997.

[87] R Mills. Private communication.

[88] I Porras. Private communication.

[89] JT Goorley, WS Kiger Iii, and RG Zamenhof. Reference dosimetry calculations for neutron capture therapy with comparison of analytical and voxel models. *Medical Physics*, 29(2):145–156, 2002.

[90] JS Hendricks. MCNPX version 2.5.c. Technical report, Los Alamos National Laboratory, 2003.

[91] W von Lensa, D Vulpius, and HJ Steinmetz. Treatment and disposal of irradiated graphite and other carbonaceous waste. *Atw. Internationale Zeitschrift fuer Kernenergie*, 56(4-5):263–269, 2011.

[92] A Wallner, M Bichler, K Buczak, I Dillmann, F Käppeler, A Karakas, C Lederer, M Lugaro, K Mair, A Mengoni, et al. Accelerator mass spectrometry measurements of the 13C(n,γ) 14C and 14N(n,p)14C cross sections. *Physical Review C*, 93(4):045803, 2016.

[93] F Ajzenberg-Selove. Energy Levels of Light Nuclei A=14. *Nucl. Phys*, 523:1, 1991.

[94] A Tzelepi, MP Metcalfe, RW Mills, JH Dinsdale-Potter, and G Copeland. Understanding the formation and behaviour of C-14 in irradiated Magnox graphite. *Carbon*, 165:100–111, 2020.

[95] MP Metcalfe, AW Banford, Harry Eccles, and S Norris. EU Carbowaste project: Development of a toolbox for graphite waste management. *Journal of nuclear materials*, 436(1-3):158–166, 2013.

[96] GR Hennig. Thermal neutron capture cross section of carbon-13. *Physical Review*, 95(1):92, 1954.

[97] GA Bartholomew. Neutron capture gamma rays. *Annual review of nuclear science*, 11(1):259–302, 1961.

[98] HT Motz and ET Jurney. Washington AEC Office Reports 1044. Technical report, 1963.

[99] SF Mughabghab, MA Lone, and BC Robertson. Quantitative test of the Lane-Lynn theory of direct radiative capture of thermal neutrons by 12C and 13C. *Physical Review C*, 26(6):2698, 1982.

[100] RB Firestone and ZS Revay. Thermal neutron radiative cross sections for ^{6,7}Li, ^{9}Be, ^{10,11}B, ^{12,13}C, and ^{14,15}N. *Physical Review C*, 93(5):054306, 2016.

[101] ILL High-Flux research reactor. https://www.ill.eu/. [Online; accessed 30-Sep-2021].

[102] W Kutschera, P Collon, H Friedmann, R Golser, P Hille, A Priller, W Rom, P Steier, S Tagesen, A Wallner, et al. VERA: A new AMS facility in Vienna. *Nuclear Instruments and Methods in Physics Research Section B: Beam Interactions with Materials and Atoms*, 123(1-4):47–50, 1997.

[103] H Häse, A Knöpfler, K Fiederer, U Schmidt, D Dubbers, and W Kaiser. A long ballistic supermirror guide for cold neutrons at ILL. *Nuclear Instruments and Methods in Physics Research Section A: Accelerators, Spectrometers, Detectors and Associated Equipment*, 485(3):453–457, 2002.

[104] Hartmut Abele, D Dubbers, H Häse, M Klein, A Knöpfler, M Kreuz, T Lauer, B Märkisch, D Mund, V Nesvizhevsky, et al. Characterization of a ballistic supermirror neutron guide. *Nuclear Instruments and Methods in Physics Research Section A: Accelerators, Spectrometers, Detectors and Associated Equipment*, 562(1):407–417, 2006.

[105] University of Vienna. Accelerator mass spectrometry at VERA. https://isotopenphysik.univie.ac.at/en/vera/. [Online; accessed 30-Sep-2021].

[106] K Lefmann and K Nielsen. McStas, a general software package for neutron ray-tracing simulations. *Neutron news*, 10(3):20–23, 1999.

[107] P Willendrup, E Farhi, and K Lefmann. McStas 1.7-a new version of the flexible Monte Carlo neutron scattering package. *Physica B: Condensed Matter*, 350(1-3):E735–E737, 2004.

[108] P Willendrup, Emmanuel Farhi, E Knudsen, U Filges, and Kim Lefmann. McStas: Past, present and future. *Journal of Neutron Research*, 17(1):35–43, 2014.

[109] J Meija, TB Coplen, M Berglund, WA Brand, P De Bièvre, M Gröning, NE Holden, J Irrgeher, RD Loss, T Walczyk, et al. Isotopic compositions of the elements 2013 (IUPAC Technical Report). *Pure and Applied Chemistry*, 88(3):293–306, 2016.

[110] S Mughabghab. Resonance Properties and Thermal Cross Sections Z=1-60. In *Atlas of Neutron Resonances, Vol. 1*. Elsevier Amsterdam, 2018.

[111] B Pritychenko and SF Mughabghab. Neutron thermal cross sections, Westcott factors, resonance integrals, Maxwellian averaged cross sections and astrophysical reaction rates calculated from the ENDF/B-VII.1, JEFF-3.1.2, JENDL-4.0, ROSFOND-2010, CENDL-3.1 and EAF-2010 evaluated data libraries. *Nuclear Data Sheets*, 113(12):3120–3144, 2012.

[112] K Rozanski, W Stichler, R Gonfiantini, EM Scott, RP Beukens, B Kromer, and J Van Der Plicht. The IAEA 14C intercomparison exercise 1990. *Radiocarbon*, 34(3):506–519, 1992.

[113] T Wieninger. Diploma thesis: Production of a Radiocarbon Reference Material for Accelerator Mass Spectrometry by neutron activation. 2013.

[114] M Nadeau and PM Grootes. Calculation of the compounded uncertainty of 14C AMS measurements. *Nuclear Instruments and Methods in Physics Research Section B: Beam Interactions with Materials and Atoms*, 294:420–425, 2013.

[115] GC Hanna, DB Primeau, and PR Tunnicliffe. Thermal neutron cross sections and resonance integrals of the reactions 17O(n,α)C14, 36Ar(n,α)33S, and 14N(n,p)14C. *Canadian Journal of Physics*, 39(12):1784–1806, 1961.

[116] T Wright, SA Bennett, et al. EXFOR entry: 13C(n, γ) cross section. https://www-nds.iaea.org/exfor/servlet/X4sGetSubent?reqx=50678&subID=23538002. [Online; accessed 23-Sep-2021].

[117] MR Bhat. Evaluated nuclear structure data file (ENSDF). In *Nuclear data for science and technology*, pages 817–821. Springer, 1992. [http://www.nndc.bnl.gov/ensdf/. Online; accessed 29-Sep-2021].